Master Thesis, Department of Geosciences

De-blending of marine seismic hydrophone and multicomponent data

Fredrik Magnussen

Supervisors: C. Sanchis, T. Elboth and L.-J. Gelius.

UNIVERSITY OF OSLO
FACULTY OF MATHEMATICS AND NATURAL SCIENCES

De-blending of marine seismic hydrophone and multicomponent data

Fredrik Magnussen

Master Thesis in Geosciences

Discipline: Geophysics

Department of Geosciences

Faculty of Mathematics and Natural Sciences

University of Oslo

June, 2015

Acknowledgements

This thesis concludes a two year master program at the Department of Geoscience at the University of Oslo. It has been done in the collaboration between the University of Oslo and the geoscience company CGG. First, I would like to thank my external supervisor Dr. Charlotte Sanchis for her guidance and help. I thank Dr. Thomas Elboth for daily discussions, his encouragements and important feedback.

Secondly, I would like to thank my internal supervisor, Prof. Leiv-J. Gelius for his initial contributions, and Prof. Isabelle Lecomte for constructive feedback.

Furthermore, this work was partly performed on the Abel Cluster, owned by the University of Oslo and the Norwegian metacenter for High Performance Computing (NOTUR), and operated by the Department for Research Computing at USIT, the University of Oslo IT-department. http://www.hpc.uio.no/

Finally, I would like to thank my family and friends who have supported me during my studies. Without their help, I would not be where I am today.

Oslo, June 2015 Fredrik Magnussen

Abstract

Blended marine acquisition, i.e., marine acquisition where multiple sources have been utilized, is the next breakthrough in marine seismic acquisition. It has the ability to improve quality and/or decrease acquisition time, resulting in a better image of the subsurface and/or reducing acquisition cost. However, the main drawback of blended acquisition is the cross-talk between successive shots, i.e., the overlap due to firing shots simultaneously. The removal of this cross-talk, called blending noise, can be done in two ways: passively by direct imaging, or actively by de-blending. De-blending can be seen as a noise attenuation problem, or as an inversion problem.

Furthermore, recent development of streamers have led to combining both hydrophones, which measure pressure (P), and geophones, which measure particle velocity. This has led to a new type of streamer called multicomponent (MC) streamer.

The objective of this thesis is to take advantage of the additional information provided by MC data to improve the de-blending of P data. At the same time, we also need to deal with the challenging nature of MC data that is very noisy. For these reasons, we propose a method for joint de-blending of P and MC data, that aims at improving de-blending of P data, as well as de-blending and de-noising MC data. The existing de-blending method using P data only will be used as a benchmark to evaluate the merits of the novel joint de-blending technique. Finally, this thesis is to our knowledge, the first attempt to use MC data in de-blending.

In this thesis, the joint de-blending method has only been tested on middle frequencies (31-55 Hz) of a wide azimuth survey completed with MC streamers, and on a dataset containing 61 shots. The MC data have been numerically blended, and to not cumulate the MC noise, one of the MC datasets has been de-noised prior the blending with a second dataset. Tests done on this dataset, show that the proposed method using multicomponent data is slightly better than the one using P data only in terms of faster convergence and data quality. The multicomponent data have also been de-blended and de-noised satisfactorily.

Furthermore, using P data only, we have conducted a comparison of passive deblending by stacking and migrating the data, with active de-blending.

Contents

1 INTRODUCTION **1**

1.1 Marine seismic acquisition . . . 1

1.2 Streamer technology . . . 1

1.2.1 Conventional streamers . . . 1

1.2.2 Multi-sensor streamers . . . 3

1.3 Blended acquisition . . . 5

1.4 Literature . . . 6

1.4.1 Blending methods . . . 6

1.4.2 De-blending techniques . . . 6

1.5 Problem statement . . . 7

1.6 Thesis outline . . . 8

2 NOISE IN MARINE SEISMIC DATA **9**

2.1 Introduction and classification of noise . . . 9

2.2 Common noise associated to marine seismic . . . 9

2.2.1 Coherent noise . . . 10

2.2.2 Random noise . . . 13

2.3 Multi-sensors related noise . . . 13

3 NOISE ATTENUATION TECHNIQUES **17**

3.1 Introduction . . . 17

3.2 Common noise attenuation techniques . . . 17

3.2.1 Frequency filtering . . . 17

3.2.2 f-k filter . . . 18

3.2.3 Linear Radon ($\tau - p$) transform . . . 19

3.2.4 f-x Prediction filter . . . 20

3.2.5 Rank reduction techniques (SVD) . . . 22

3.3 Noise attenuation techniques used in de-blending . . . 24

3.3.1 f-x Cadzow filter . . . 24

3.3.2 Time frequency de-noising (TFDN) . . . 32

3.3.3 Joint de-noising of multicomponent data . . . 32

4 DE-BLENDING OF SEISMIC DATA **35**

4.1 Introduction . . . 35

4.2 De-blending of P data . . . 38
4.2.1 General algorithm . . . 38
4.2.2 Filters . . . 42
4.2.3 Brief comparison between f-x Cadzow and the hybrid filter . . . 42
4.2.4 Algorithmic aspects . . . 45
4.3 Joint de-blending of P and MC data . . . 50
4.3.1 Method . . . 52
4.3.2 Other Attempts . . . 53
4.3.3 Algorithmic aspects . . . 54

5 FIELD DATA EXAMPLES 55
5.1 Introduction . . . 55
5.2 Faroese 2D field data: De-blending of P data . . . 56
5.2.1 General information . . . 56
5.2.2 Blended acquisition design . . . 56
5.2.3 De-blending strategy . . . 57
5.2.4 Results . . . 58
5.3 Wide azimuth 2D field data: Joint de-blending of P and MC data . . . 66
5.3.1 General information and blending strategy . . . 66
5.3.2 De-blending strategy . . . 70
5.3.3 Results . . . 70

6 DISCUSSION 77
6.1 Active vs. passive de-blending . . . 77
6.2 De-blending using f-x Cadzow . . . 78
6.3 Joint deblending of P and MC data . . . 78

7 CONCLUSION AND FUTURE WORK 81

A CHARACTERIZATION OF NOISE MODES IN MULTICOMPONENT STREAMERS 85
A.1 Transverse vibrations . . . 85
A.2 Longitudinal vibrations . . . 86
A.3 Angular vibrations . . . 86

B FAROESE TEST - ADDITIONAL RESULTS 87
B.1 Scenario 1 . . . 87
B.2 Scenario 2 . . . 87

Bibliography 93

Abbreviations

CMP	**C**ommon **M**id**P**oint
CO	**C**ommon **O**ffset
CR	**C**ommon **R**eceiver
CS	**C**ommon **S**hot
DFT	**D**igital **F**ourier **T**ransform
f-k	**F**requency-wavenumber(**K**)
f-x	**F**requency-offset(**X**)
ICA	**I**ndependent **C**omponent **A**nalysis
MC	**M**ulti **C**omponent
NRMS	**N**ormalized **R**oot **M**ean **S**quare
NMO	**N**ormal **M**ove-**O**ut
OBS	**O**cean **B**ottom **S**ensor
RMS	**R**oot **M**ean **S**quare
SI	**S**eismic **I**nterference
SNR	**S**ignal-to-**N**oise **R**atio
SSA	**S**ingular **S**pectrum **A**nalysis
SVD	**S**ingular **V**alue **D**ecomposition
TFDN	**T**ime **F**requency **D**e-**N**oising

1 Introduction

This thesis deals with de-blending of marine seismic data acquired with a towed multi-sensor streamer, where both hydrophone (P) and multicomponent (MC) particle velocity data are recorded. This first chapter gives an introduction to marine seismic acquisition, streamer technology and blended acquisition. It is followed by a literature review of existing blending and de-blending schemes. Finally, the problem statement and the outline of the thesis are provided.

1.1 Marine seismic acquisition

These days geophysical surveys are used for exploration of hydrocarbons and other resources that is located inside the earth. For offshore exploration, marine seismic acquisition is the most common method. Marine seismic acquisition is done with large seismic vessels towing one or multiple air gun arrays behind the vessel. They create a seismic signal by forcing highly pressurized air into the water. Receivers are towed behind the ship in one or several long streamers that are typically 6-9 kilometers long (Gelius and Johansen, 2010). Figure 1.1 shows the schematics of a marine seismic survey with one seismic vessel, two air gun arrays and multiple streamers towed behind the vessel.

1.2 Streamer technology

1.2.1 Conventional streamers

The first oil-filled streamer for geophysical purposes was patented in 1947 by R. Pasley, G. Pavey and P. Wipff (Pavey, 1966; Lawyer et al., 2001) and was an oil-filled streamer with piezoelectric hydrophones as sensors. The ideas behind a towed streamer and the use of piezoelectric material as a sensor can be traced back to the research done by the U. S. Navy for anti-submarine devices (Hayes, 1920; Namorato, 2000).

Piezoelectric materials create an electrical charge measured as voltage when submitted to strain. It can be crystals such as quartz or ceramics such as barium titanate. Piezoelectric hydrophones

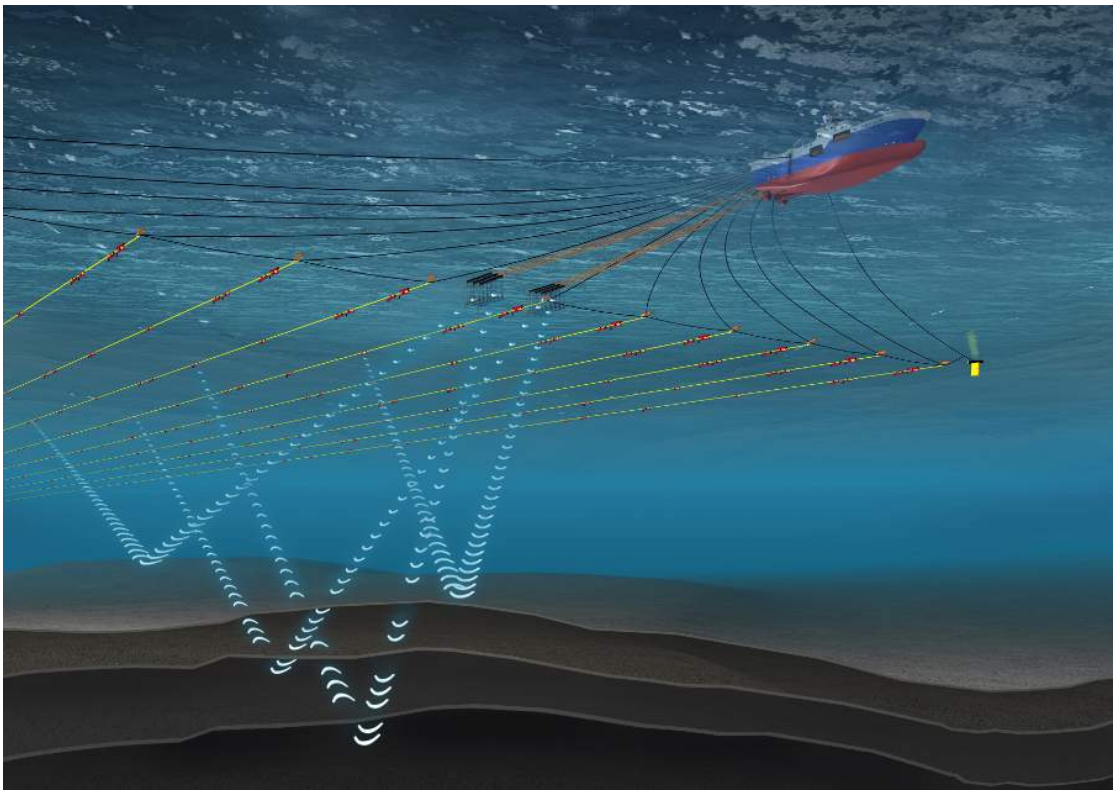

Figure 1.1: Marine seismic survey, with seismic vessel, air guns and streamers. Image courtesy of CGG.

Filling	Sensor layout	Streamer profile
• Fluid • Solid	• Conventional by grouping • Point-receiver recording	• Streamer is placed horizontal in the water column • Over/under streamers • Slanted streamer

Table 1.1: Different configurations for hydrophone only streamers.

react to a change in pressure by a squeezing motion (Figure 1.2a) proportional to the measured voltage (Meunier, 2011).

Today, conventional streamers consist of a set of 150 m sections with 12 stations containing a group of 8 to 16 hydrophones, resulting in a receiver sampling of 12.5 m. Buoyancy is achieved by filling the streamer with kerosene resulting in a fluid streamer (Meunier, 2011). The number of towed streamers has increased steadily from 3 in 1991 to 24 (PGS, 2015) in 2015. Table 1.1 lists the different configurations for a streamer, in terms of streamer filling, sensor layout and streamer profile.

Solid streamers became available in the 1990s (Dragoset, 2005). They are less sensitive to swell noise and insensitive to vibrations from depth-controllers (birds) and towing equipment (Dowle,

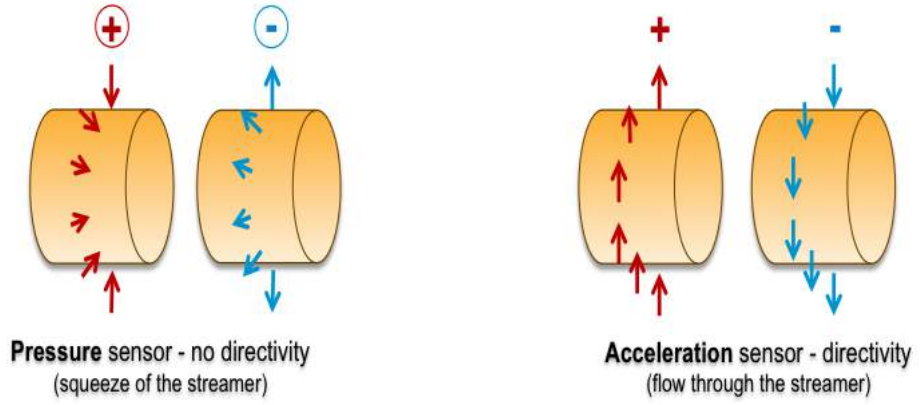

(a) (b)

Figure 1.2: Different kind of sensors in a streamer. a) Pressure sensor. b) Acceleration sensor. Courtesy CGG.

2006). This allows for more flexibility on towing depth.

The hydrophone data can be sampled differently. Blacquière and Ongkiehong (2000) suggest sampling each single hydrophone sensor, instead of grouping them. According to their study two major advantages are pointed out: possibility to apply a spatial anti-alias filter before decimation, i.e., reducing the sampling rate, and the possibility to correct for small-scale 'perturbations' (e.g., amplitude variations, 'dead' sensors, polarity reversal, intra-group statics).

Different streamer layouts can be implemented to recover a larger frequency content than by conventionally towing the streamer horizontally at a fixed depth in the water column. Two different designs are discussed: Over/under acquisition and slanted streamer. Parrack (1976) patented the use of placing two streamer cables at different vertical depths in the water column, i.e., over/under acquisition. Moldoveanu et al. (2007) discuss the benefits of such a system by the application of separating the wave-field into up- and down-going waves. Ray and Moore (1982) patented the use of placing of the streamer at different water-depths. Soubaras and Dowle (2010) discuss the benefits that can be achieved by using a variable-depth streamer in terms of attenuating the receiver ghost (cf. section 2.2.1).

1.2.2 Multi-sensor streamers

Recent streamer development has led to streamers with collocated hydrophones and geophones, i.e., a multi-sensors streamer. Contrary to hydrophones, geophones measure particle velocity or acceleration (or pressure derivatives). Figure 1.2b illustrates this schematically. On todays market, two types of multi-sensor streamer exist:

- Dual-sensor streamer (Pavey and Pearson, 1966; Berni, 1985; Tenghamn et al., 2007).
- Multicomponent (MC) streamer (Robertsson et al., 2008).

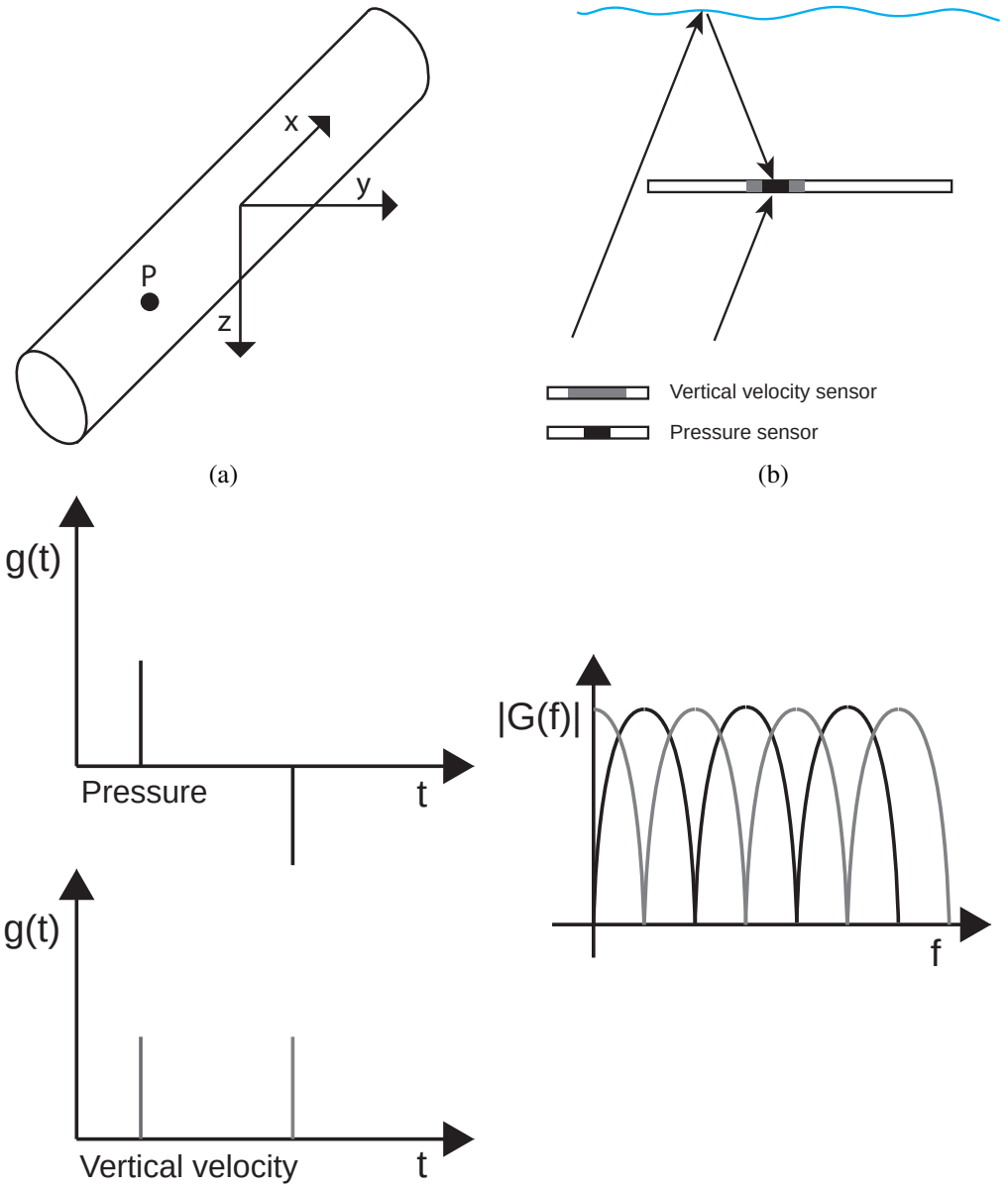

Figure 1.3: (a) MC sensor containing a hydrophone and directional motion sensors (Teigen et al., 2012). (b) P and MC sensors recording the up-going and down-going (sea-surface ghost) waves. (c) Time response for the recorded signal (left) and corresponding amplitude spectra for the pressure and vertical velocity sensor (right). Modified after Parkes and Hegna (2012).

The dual-sensor records pressure with hydrophones, hereby denoted as P data, and vertical particle velocity, Z data. The multicomponent streamer records particle velocities in inline, crossline and vertical directions, hereby denoted by X, Y and Z data respectively. Figure 1.3a illustrates a multicomponent streamer that records P data as well as data in X-, Y- and Z-directions.

Figure 1.3b shows a multi-sensor streamer recording a primary arrival (up-going wave) and its sea-surface reflection, i.e. receiver ghost (down-going wave) (cf. section 2.2.1). Contrary to hydrophones, geophones are directionally sensitive, up- and down-going waves are in a 1D

sense recorded with opposite polarities. Accordingly, up-going signals recorded by collocated hydrophones and geophones are in phase while down-going signals, like ghosts reflections, are 180 ° out of phase. Figure 1.3c shows the time response of a primary arrival and its sea-surface reflection (left) and the corresponding amplitude spectrum (right) for pressure and vertical velocity. Therefore, when the vertical particle velocity, Z data, is measured together with the pressure field, P data, we can decompose the seismic signal into an up-going and down-going wave field. This technique, also known as PZ summation, aims of attenuating the receiver ghost (Carlson et al., 2007; Caprioli et al., 2012), thereby recovering a broader frequency band. Some other applications for multicomponent data are listed below, but is not covered in this thesis:

- Using Z data to relax assumptions in marine data-driven demultiple algorithms (Frijlink et al., 2011).
- Using multicomponent X, Y and Z data to reconstruct P data in the crossline direction (Robertsson et al., 2008).

However, the problem with the multicomponent streamer is that it is very sensitive to mechanical vibrations (cf. section 2.3) as geophones measure movement and therefore, multicomponent data are very noisy, especially in the first 50 Hz.

1.3 Blended acquisition

Seismic surveys are often a trade-off between quality and economics. Conventional seismic has relatively long time intervals between shots to avoid interference with the next shot recorded by the receivers. This results in time-consuming and therefore expensive surveys with poor sampling in source domain. To address these problems, simultaneous shooting with two or more sources, also called blended acquisition, has been developed. It was probably first introduced by Barbier and Staron (1972) and Barbier and Viallix (1974) and later rediscovered by Beasley et al. (1998). As recently pointed out by Berkhout (2008), blended acquisition has the possibility to decrease acquisition time, by reducing the waiting time between firing sources and/or improve data quality, introducing multiple sources.

Blended acquisition has been used for a long time in land surveys. As this thesis only covers the marine application of blending, I refer the reader to see Bagaini (2006) for an overview over land seismic acquisition techniques.

Blended acquisition opens many possibilities for different acquisition designs. For example, one vessel towing streamers and source(s) are accompanied with one shooting vessel to cover a larger area in less time. A more creative implementation could be one towing vessel with circling source boats shooting from different angles to illuminate the surface from different directions.

1.4 Literature

1.4.1 Blending methods

For the marine case, blended acquisition was probably first introduced by Barbier and Staron (1972) and Barbier and Viallix (1974), under the name "SOSIE", where usage of several sources during the normal recording time is suggested. Later, the concept was reintroduced by Beasley et al. (1998). In Beasley et al. (1998) study, two sources were placed at the opposite sides of a 2D streamer and fired simultaneously. The sources were then separated using dip filtering. Timoshin and Chizhik (1990) patented the concept of seismic acquisition using a random or quasi-random time-delay between the firing sources. Vaage (2002) did the same in later years. Hampson et al. (2008) presented a near-simultaneous shooting technique with small time-delays between sources. Berkhout et al. (2009) extended the blending concept to the receiver side. By combining incoherent shooting with incoherent recording the concept of double blending was introduced. Mansour et al. (2012) proposed a quantitative method for analyzing blended acquisition setups using compressive sensing measures. Parkes and Hegna (2012) developed a new blended acquisition technique using multicomponent streamers and sources that fire at different depths and times to accomplish a ghost-free solution at the source side. Berkhout (2013) introduced the network concept of distributed blended acquisition. Wason et al. (2014) extended blended acquisition to time-lapse surveys where the results were comparable to conventional methods.

1.4.2 De-blending techniques

The main problem with the processing of blended data is the crosstalk between neighboring shots, i.e., interference noise, due to overlap. Removal of this type of noise can either be done by direct imaging and waveform inversion (Berkhout et al., 2012; Choi and Alkhalifah, 2012; Guitton and Díaz, 2012; Plessix et al., 2012; Xue et al., 2014) or by de-blending, i.e., separation of the blended data into their respective source followed by conventional processing. This thesis focuses on the de-blending approach. The reader is therefore referred to the papers mentioned above if interested in the more direct imaging approach.

De-blending techniques can be seen either as a random noise problem or as an inverse problem. Ikelle (2007) addressed the problem using Independent Component Analysis (ICA) to separate multiple sources. Techniques using random noise attenuation exploit the fact that the coherency of blended data, shot with different time-delays for each shot, varies in different data domains. Thus, one can de-blend the data by filtering out random interference noise in a domain where one source is seen as coherent, while the other sources are seen as random. Kim et al. (2009) build a noise model in the common offset domain of ocean bottom seismic (OBS) and subtract it

to obtain results. Huo et al. (2012) apply a vector median filter after sorting the data to common-midpoint (CMP) domain. Maraschini et al. (2012) used an iterative f-x Cadzow in the common offset (CO) domain.

Inversion treats the problem as an estimation problem of the unknown unblended data. This is an ill-posed problem, i.e., the problem has many solutions and therefore regularization is needed (Doulgeris et al., 2012). Akerberg et al. (2008) and Moore et al. (2008) used sparse Radon inversion, while Ibrahim and Sacchi (2013) used a robust Radon inversion. Lin and Herrmann (2009) and Wason et al. (2011) used a curvelet-based source separation. Abma et al. (2010) separated the data by a project gradient optimization algorithm. Mahdad et al. (2012) and Doulgeris et al. (2012) used an iterative f-k filtering approach. Finally, Cheng and Sacchi (2013) used an iterative f-x Cadzow for the de-blending approach. This is an active area of research and other solutions also exist.

1.5 Problem statement

As stated earlier, blended acquisition has the possibility to decrease acquisition time and/or improve data quality. The main problem with processing of blended data is crosstalk between neighbouring shots, i.e., interference noise, due to data overlap. Removal of this type of noise can be done passively by direct imaging and waveform inversion (Berkhout et al., 2012) or actively by *de-blending*, i.e., separation of the blended data into individual source contributions followed by conventional processing. De-blending is the process of retrieving the data as it was acquired in a conventional, unblended way. This step has to be applied if conventional processing workflows are applied to the data. De-blending of blended seismic data is the major focus of this thesis.

The objective of this thesis is to take advantage of the additional information provided by MC data to improve the de-blending of P data. At the same time, we also need to deal with the challenging nature of MC data that is very noisy. For these reasons, we propose a method for joint de-blending of P and MC data, that aims at improving de-blending of P data, as well as de-blending and de-noising MC data. The existing de-blending method using P data only will be used as a benchmark to evaluate the merits of the novel joint de-blending technique. Finally, this thesis is to our knowledge, the first attempt to use MC data in de-blending.

The main ideas behind the novel method presented were proposed by Dr. Charlotte Sanchis. The author has implemented the ideas, done all the testing and improvements related to run time.

1.6 Thesis outline

This thesis consists of seven parts. The first part gives a general background of the thesis, its objectives and outline. The next parts are:

Chapter 2 *Noise in marine seismic data.*
This chapter covers noise related to marine seismic data. Common noise as well as noise related to multicomponent data are presented.

Chapter 3 *Noise attenuation techniques.*
In this chapter, noise attenuation techniques are presented. These techniques are essential in the understanding of the methods presented in chapter 4.

Chapter 4 *De-blending of seismic data.*
In this chapter, the iterative estimation and subtraction for de-blending P data is presented. Also the novel method for joint de-blending of P and MC data is presented, as well as other attempts in the development of the method.

Chapter 5 *Field data examples.*
The de-blending methods described in chapter 4 are tested on real datasets. The datasets have been numerically blended and a numerical evaluation of the results has also been done.

Chapter 6 *Discussion.*
Main observations from the field data examples are discussed in this chapter.

Chapter 7 *Conclusion and future work*
In the final chapter, conclusion and suggestions for future work are given.

The programming related to the development of the method has solely been done in MATLAB. Some initial de-noising, stacking and migration have been carried out with CGG processing software.

2 Noise in marine seismic data

2.1 Introduction and classification of noise

In this chapter a discussion on common noise associated to marine seismic will be presented as well as noise related to multi-sensors streamers. In general, noise is divided into the categories coherent and random noise. Coherent noise can be followed and predicted over a number of traces, while random noise is unpredictable. In a general way, seismic data x can be decomposed into the sum of signal, s and noise, n, as follows:

$$x = s + n. \tag{2.1}$$

Recorded data is usually too noisy and needs to be cleaned by different techniques before further processing. Noise attenuation techniques are presented in chapter 3. An optimal case will be to attenuate all the noise, n, and be left with the noise-free signal, s.

2.2 Common noise associated to marine seismic

In this section a brief discussion on noise related to traditional marine seismic will be given. These are presented in table 2.1 where they are divided into the categories coherent and random noise.

Coherent noise	**Random noise**
Multiples	Ambient noise
Ghosts	Swell noise
Diffractions	
Refracted and direct waves	
Seismic interference	

Table 2.1: List of different coherent and random noise types.

2.2.1 Coherent noise

Multiple reflections

Multiple reflections are non-linear coherent noise due to entrapment of energy either between the sea-bottom and the sea-surface, the water layer, or between layers in the subsurface called a peg-leg multiple. Multiples have the same frequency as the survey and decay in amplitude over time. Figure 2.1 displays a water-bottom multiple, source-ghost and two different peg-legs.

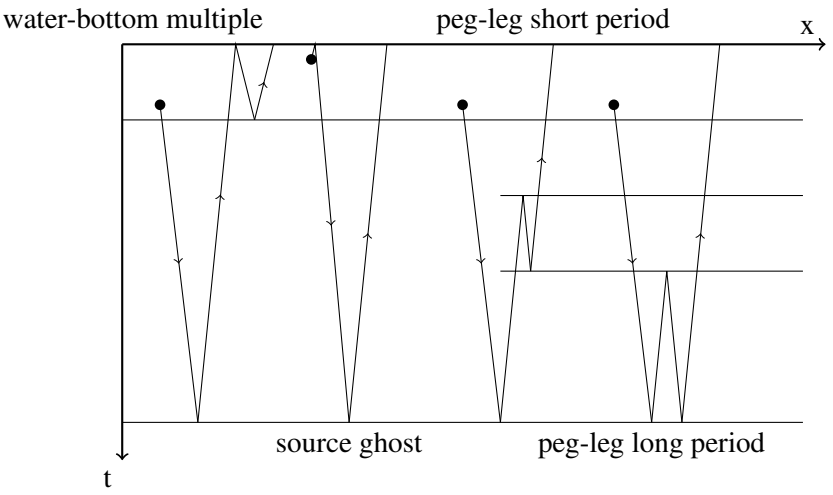

Figure 2.1: Example of different kind of multiples: water-bottom multiple, source-ghost and two different peg-leg multiples modified after Gelius and Johansen (2010).

Ghost reflections

Ghost reflections are non-linear coherent noise and can be treated as a special case of multiples. The ghost reflections can either come from the receiver side, a receiver-ghost, or the source side, a source-ghost. Ghost reflections are due to that the air-water contact acts as a mirror when the sea is relatively calm. Hence, when the air gun array is fired we record an initial pulse $s_0(t)$ followed by a delayed pulse due to the sea surface reflection, resulting in a distorted wavelet $s(t)$:

$$s(t) = s_0(t) - r s_0(t - t_0) \quad , r \in [0, 1], \tag{2.2}$$

where r is the reflection coefficient and t_0 is the delay. This expression is valid for both the receiver and source side, where only r and t_0 change.

Figure 2.2 illustrates the primary wave (1), source ghost (2), receiver ghost (3) and the source and receiver ghost (4). All these events except the primary wave are considered as noise.

The ghost interferes both constructively and destructively with the primary reflection, causing notches in the amplitude-frequency spectrum illustrated by the blue curve in Figure 2.3. By removing the receiver ghosts one obtains a broader frequency content (red curve). The source

ghost can be removed by placing sources at different depths in the water-column (Parkes and Hegna, 2012).

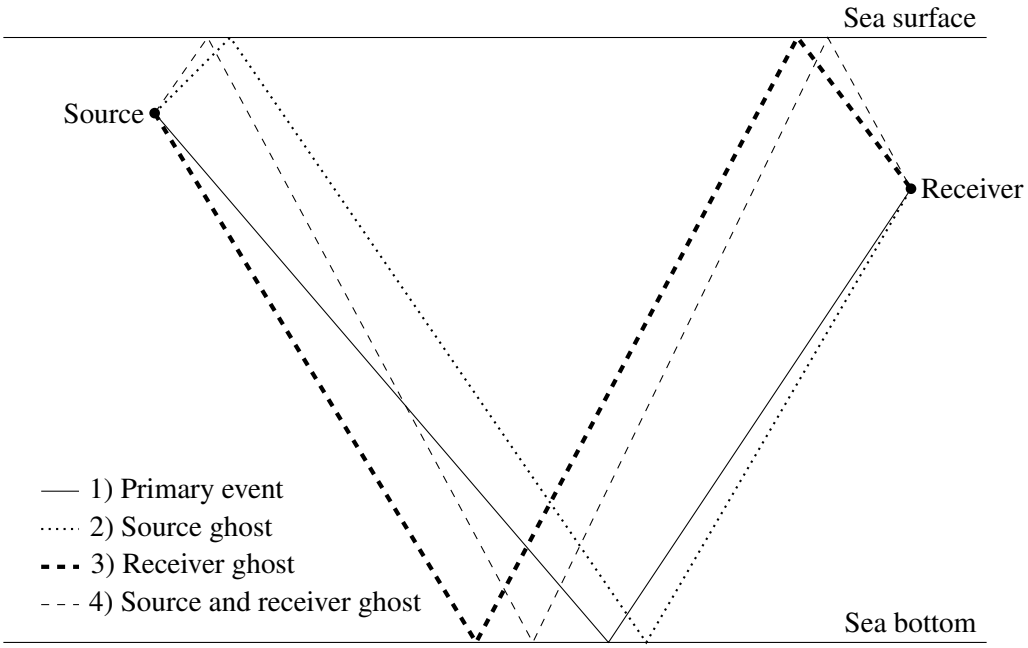

Figure 2.2: 1) Primary event, 2) Source ghost, 3) Receiver ghost and 4) Source and receiver ghost. All reflections except the primary event are considered as noise. By employing multi-sensors streamers one can remove the ghost on the receiver-side.

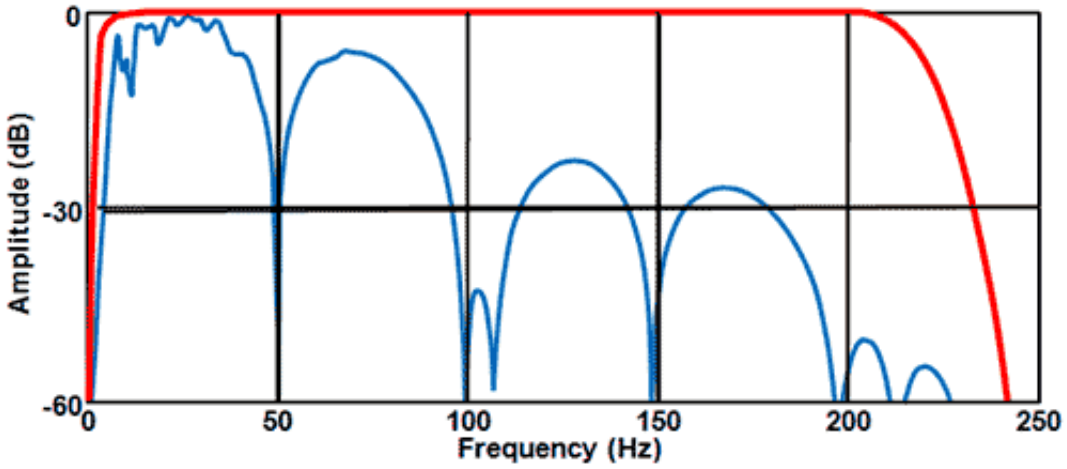

Figure 2.3: The ghost reflections interfere constructively and destructively with the primary event and the result can be seen as notches in the amplitude-frequency spectrum (blue color). The recovered spectrum without ghost-reflections is shown in red.

Diffraction

Diffraction is due to wave energy that gets scattered when meeting a discontinuity like a fault, boulders on the seafloor or sudden changes of facies. In a seismic profile, the diffraction noise has an hyperbolic shape (Figure 2.4).

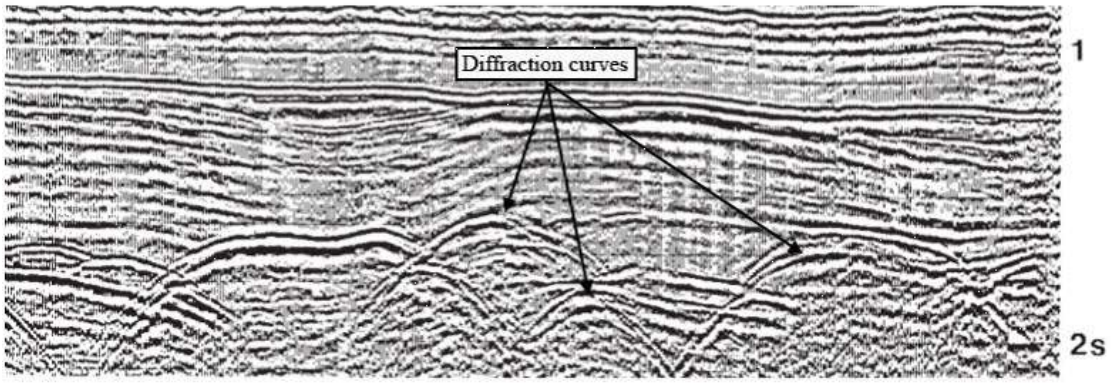

Figure 2.4: Hyperbolic shape in seismic data caused by diffraction. Image courtesy CGG.

Refracted and direct waves

Direct waves are characterized by high amplitudes, they go directly from source to receiver without having travelled through the subsurface and are therefore of no interest. Refracted waves are entrapment of waves between two layers that leak energy to the surface. Refracted waves occur when the incidence angle of the wave goes past the critical angle.

Seismic interference noise

Seismic interference noise can have high amplitudes and a broad band of frequencies. Seismic interface noise is caused by nearby seismic surveys or anomalies that diffract the seismic energy in the survey area. Figure 2.5 shows a shot gather that is corrupted by seismic interference (SI) noise. The SI noise observed is typically acoustic energy that is trapped in the water column and can be problematic up to 100 km away.

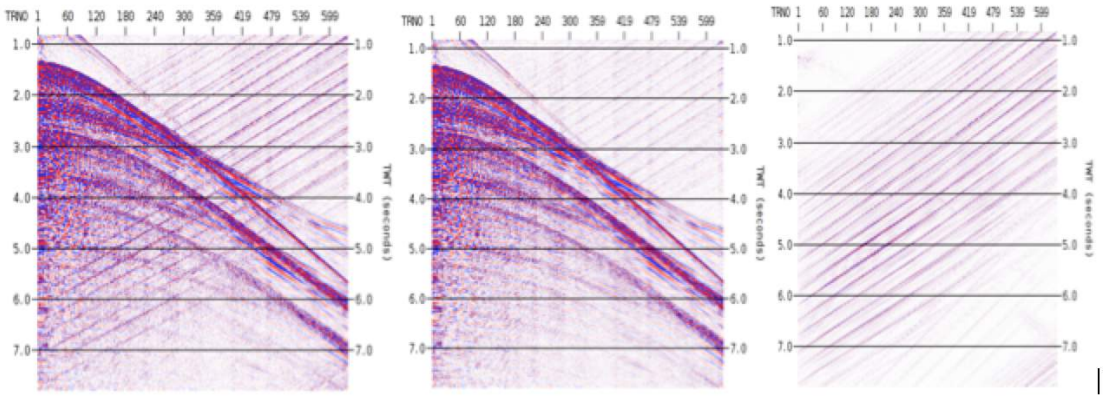

Figure 2.5: Seismic interference before (left) and after (middle) attenuation of SI. The difference is plotted to the right. Image courtesy CGG.

2.2.2 Random noise

Swell noise

Swell noise is high amplitude, low frequency (2-15 Hz) noise caused by rough weather conditions during acquisition. Swell noise can not be removed by a band pass filter as it would remove seismic signal that belongs to the same frequency range (Elboth and Hermansen, 2009). It is typically caused by streamer vibrations and turbulence that interacts with the streamer.

Ambient noise

Ambient noise is usually low amplitude, high frequency noise. It is caused by machinery, nearby boats, marine life, tides and weather (i.e., wind and rain).

Random noise is independent on the survey. Therefore it causes trouble for 4D seismic, i.e., repeating a 3D survey again at a later time over a specific area. 4D seismic measures the occurred changes in the subsurface and is typically done over a producing reservoir.

2.3 Multi-sensors related noise

Multi-sensors streamers measure both pressure and particle motion as discussed in section 1.2.2. Hydrophones are by design insensitive against vibration. In comparison, the particle motion sensors are directly sensitive to self-vibration of the cable. This gives rise to multi-sensors related noise as the cable is prone to several modes of vibration due to excitation of water around it (Teigen et al., 2012).

These different noise modes are linked with the mechanical properties of the seismic streamer and can be shaped to enable effective noise attenuation. However, to do so, a good understanding of the noise modes must be acquired through analytical and numerical modeling.

This section will try to summarize the work of Teigen et al. (2012). They present synthetic models for the different noise modes recorded by particle motions (i.e., transversal, longitudinal and torsional vibrations) and compare it with real data. Appendix A goes through the theory behind the synthetical models.

The noise analysis of Teigen et al. (2012) was performed with one type of multi-sensors streamers with stiff construction with triaxial accelerometers placed in the main body. However, we generalize this analysis as we believe that CGG's multi-sensors streamer layout is rather similar.

Transverse vibrations

Transverse vibrations propagate orthogonal to the streamer inline axis. Their velocities range from 30-120 m/s in a stiff cable which is typically slower than the seismic signal. For a stiff streamer these vibrations are aliased as discussed below and dispersive, i.e., the phase velocity is a function of frequencies (Equation A.3 in Appendix A).

Figure 2.6a illustrates the f-k spectrum of transversal vibration noise, the synthetic data (left) and observed data (right) are comparable with each other. Curved pattern indicates dispersive noise, while the wrapping of the energy indicates spatial aliasing (Ikelle and Amundsen, 2005).

Longitudinal vibrations

Longitudinal vibrations go in the same direction as the propagation direction and for a typical streamer with Kevlar stress members the propagation velocity is around 1500 m/s.

Figure 2.6b illustrates the f-k spectrum of longitudinal vibration noise for synthetic data (left) and measured data (right). In this figure, the f-k spectrum of both the measured and observed data are comparable. In comparison with transversal vibrations, longitudinal vibrations are not dispersive (Equation A.7 in Appendix A) and not aliased, due to straight lines and no wrapping in the f-k spectrum.

Angular vibrations

When the streamer is towed it rotates about the longitudinal axis (Figure 2.6c) and therefore picks up angular vibrations. For a stiff streamer the propagation velocity is around 500 to 1000 m/s while a gel- or fluid-filled streamer will experience a propagation velocity of almost zero.

Figure 2.6d illustrates measured rotational vibrations (blue curve) and an estimate of it (red curve). Teigen et al. (2012) suggests that the mismatch in the curves is due to that the sensors' orientation in the red curve are incorrectly corrected.

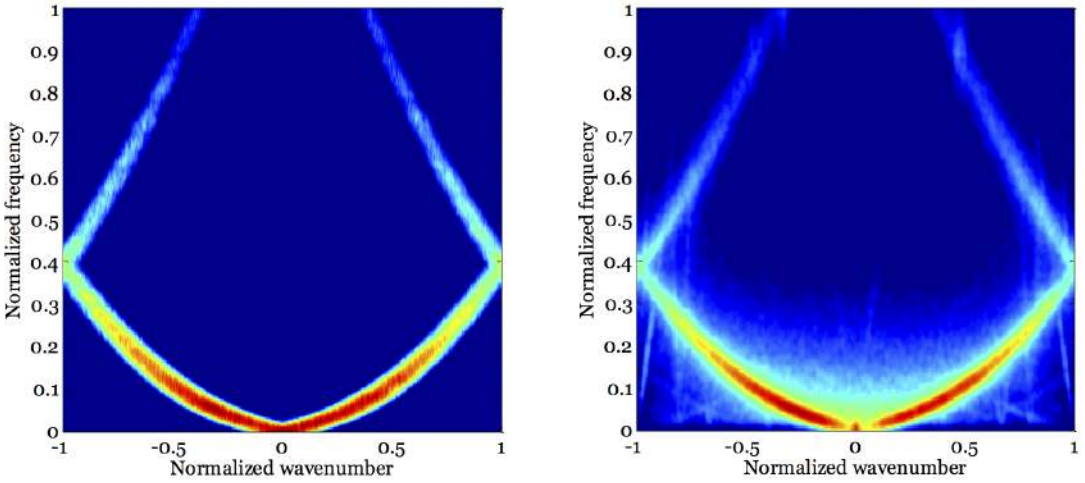

(a) F-K spectrum of transversal vibrations.

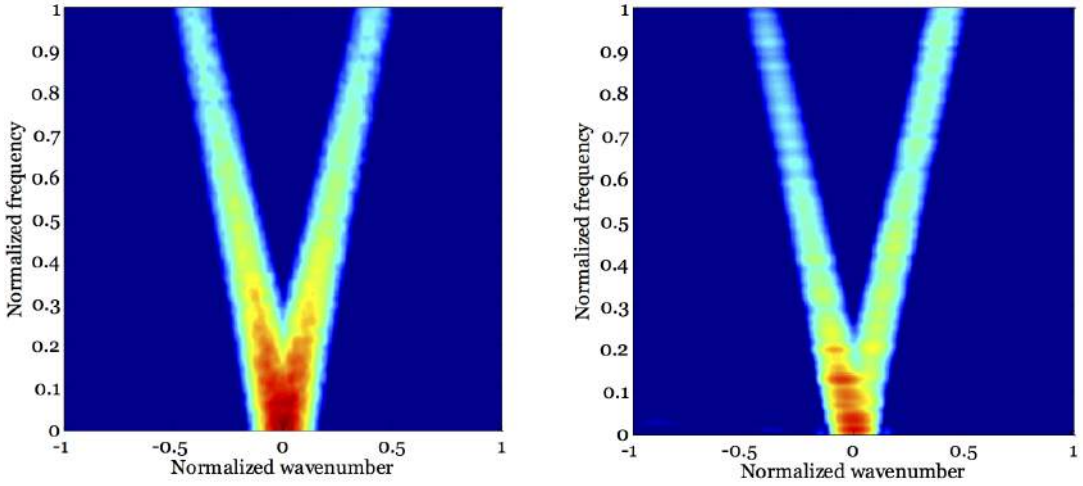

(b) F-K spectrum of longitudinal vibrations.

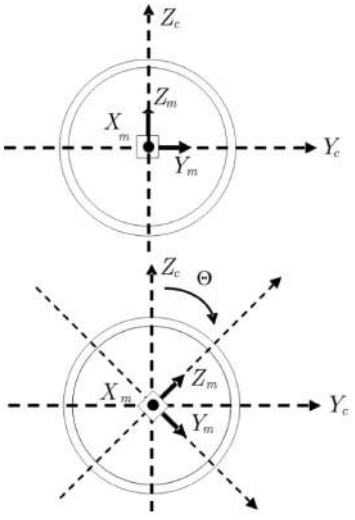

(c) Angular vibrations: Orientation.

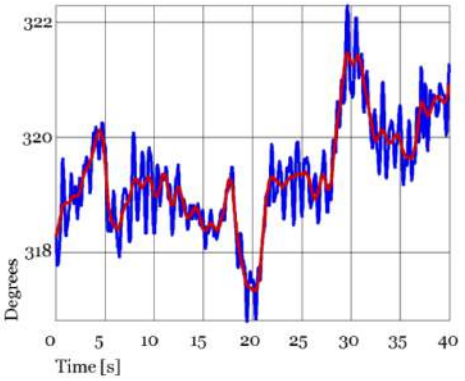

(d) Angular vibrations Degree-Time plot

Figure 2.6: (a) f-k spectrum of transversal vibrations for synthetically derived data (left) and observed data (right). Curved pattern indicates that the noise is dispersive. (b) f-k spectrum of longitudinal vibrations for synthetically derived data (left) and measured data (right). (c) Schematic drawing of the angle measured Θ in the particle motion sensor (y-z plane). (d) Orientation plot of a transverse particle motion sensor as a function of time (blue) and an estimate of it (red). Taken from Teigen et al. (2012).

3 Noise attenuation techniques

3.1 Introduction

The seismic data recorded by streamers during a marine acquisition is corrupted by different types of noise covered in chapter 2. Attenuation of this noise requires a set of noise attenuation techniques. This chapter consists of two sections. The first section, section 3.2, covers common noise attenuation techniques: frequency filtering, f-k filter, linear Radon ($\tau - p$) transform, prediction filter and filtering by rank reduction (SVD). The second section, section 3.3, covers the noise attenuation techniques used in the de-blending covered in chapter 4. These filters are: f-x Cadzow, time-frequency de-noising (TFDN) and joint de-noising of multicomponent (MC) data guided by the P-data.

The filters f-x prediction, f-x Cadzow, SVD and TFDN were programmed in MATLAB. The MATLAB code for the f-x prediction filter was modified after Sacchi (2002). The MATLAB code for the f-x Cadzow filter was modified after Reynolds (2007). Dr. Thomas Elboth guided the programming of the TFDN filter. Dr. Charlotte Sanchis provided the MATLAB code for the joint de-noising of multicomponent data. The synthetic models for the datasets consist of one straight and one dipping reflector were made using the ricker function provided by Kozola (2001) and examples given in Sacchi (2002). The f-x prediction, SVD and f-x Cadzow are tested on this simple synthetic model. Furthermore, the f-x Cadzow and TFDN were tested on a synthetic dataset named Pluto (Stoughton et al., 2001) which was numerically blended.

3.2 Common noise attenuation techniques

3.2.1 Frequency filtering

Frequency filtering is the most common technique to remove noise whose frequencies do not fall into the signal frequency band. Examples can be very low frequency swell noise or high frequency thermal noise.

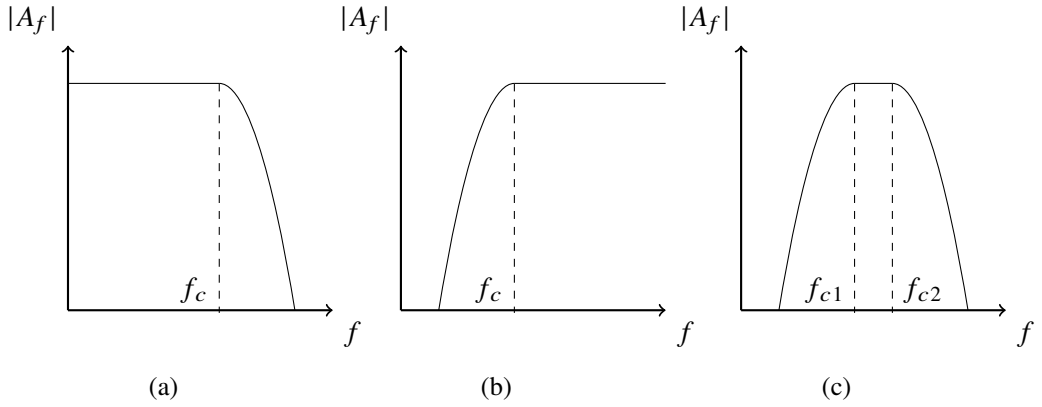

Figure 3.1: Frequency filtering: (a) Low-pass filter. (b) High-pass filter. (c) Band-pass filter.

Low-pass, high-pass and band-pass filtering

Figure 3.1(a-c) displays a low-, high- and band-pass filter respectively in the amplitude spectrum. Low- and high-pass filters remove all frequencies above and below respectively a cut-off frequency, f_c. These filters are a special case of a band-pass filter. A band-pass filter keeps all frequencies between two picked frequencies, f_{c1} and f_{c2}.

Both low-, high- and band-pass filters can be designed to be zero-phase, i.e., they do not change the phase spectrum, only the amplitude spectrum. The filters are applied by multiplication in the frequency domain, which is convolution in time domain. In addition, to avoid artifacts like Gibbs phenomena, i.e., oscillations, a slope after the cut-off frequency f_c is defined. These slopes are given by a window function, e.g, Hann, Blackman and Bartlett (Gelius and Johansen, 2010).

3.2.2 f-k filter

Attenuation of coherent noise can be done by applying a f-k dip filter (Treitel, 1970) as detailed in Figure 3.2. It consists of transforming the data from the t-x to f-k domain, then an attenuation zone is defined and set to zero. Finally the data is transformed back to the t-x domain.

In Figure 3.2, the objective is to attenuate the reflector D. In the t-x domain the reflectors C and A are overlapping with D and therefore hard to attenuate. By transforming the data to the f-k domain the reflectors A to D are separated due to different dips. The area containing D is defined and removed. When the data is transformed back to the t-x domain the reflector D has been attenuated.

The attenuation region is defined by the linear relationship between lateral wavenumber, k_x, and frequency, f,

$$k_x = \left(\frac{2\pi \sin\theta}{c}\right) f \tag{3.1}$$

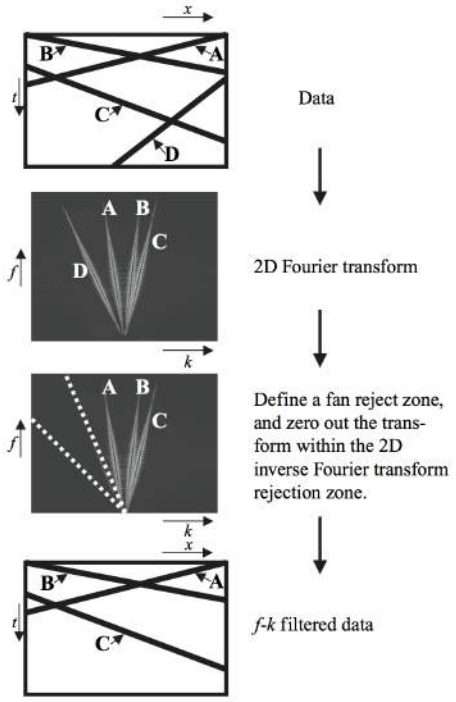

Figure 3.2: f-k dip filter flow chart. Taken from Ikelle and Amundsen (2005).

where c and θ are the velocity and incidence angle respectively. In the industry the incidence angle is usually set to 90 degrees so the filter is only defined by the velocity, the lowest velocity in the signal corresponds to the whole f-k spectrum. In academia, the velocity is typically set to the lowest value of the signal, then the incidence angle defines the region to attenuate and 0 degrees corresponds to the whole f-k spectrum.

Applications of a f-k dip filter include removal of multiples, ground roll and undesired effects of spatial aliasing.

3.2.3 Linear Radon ($\tau - p$) transform

Johan Radon (1917) is credited the Radon transform, i.e., a function that integrates a specific medium property along a particular path. The linear Radon transform, also known as the $\tau - p$ transformation, i.e., a plane wave decomposition, $u(p,\tau)$, of the data, $d(x,t)$, is given by

$$u(p,\tau) = \sum_{x} d(x, \tau + px), \tag{3.2}$$

where τ is the intercept time at zero offset, x is the offset, t is time and p is the ray parameter given by

$$p = \frac{\sin\theta}{v}, \tag{3.3}$$

where θ is the incident angle from the vertical axis and v is the wave propagation velocity. This transformation is also called the slowness slant stack, as the values along the ray parameter p

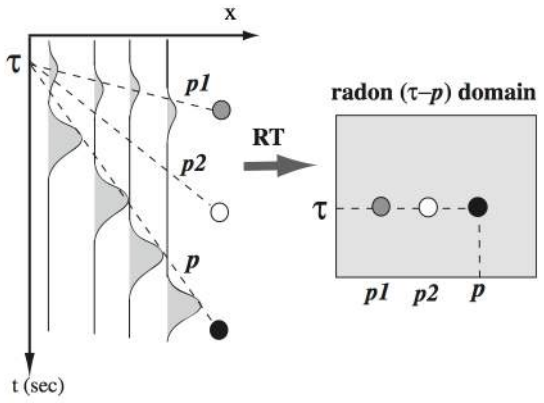

Figure 3.3: $\tau - p$ transformation. Taken from Gu and Sacchi (2009).

are stacked. Figure 3.3 illustrates the linear Radon transformation where three different plane waves have been decomposed into three dots and the color represents their amplitude in the $\tau - p$ domain. Direct and refracted waves correspond to dots in the $\tau - p$ domain, while hyperbolic events are elliptical curves (Cao et al., 2003).

In the $\tau - p$ domain we can, e.g., filter away multiples and seismic interference noise.

3.2.4 f-x Prediction filter

f-x prediction filtering proposed by Canales (1984) is an effective tool to attenuate random noise and is widely accepted and used in the industry. The f-x prediction filter is easy to implement and efficient in terms of computation.

To understand the f-x prediction filter we will first go through signal modeling in the f-x domain and then detail the filter methodology.

Signal model in f-x domain

The signal model in f-x domain is based on the assumption of that seismic data can be considered as a superposition of delayed signals with linear move out (e.g., $\delta(t - px)$). This assumption is true for a seismic section that is divided into small overlapping windows, where signals can locally be considered as linear.

We consider a seismic section with one linear event in t-x domain, $s(t, x)$ given by,

$$s(t, x) = \delta(t - px), \tag{3.4}$$

where δ is the delta function, p denotes the slope of the linear event, x is the spatial coordinate and t is the time. Taking the Fourier transform of $s(x,t)$ with respect to time gives us

$$S(\omega, x) = \int_{-\infty}^{\infty} \delta(t - px) e^{-i\omega t}\, dt = e^{-i\omega px}, \tag{3.5}$$

where the fundamental property of a delta function,

$$\int_{-\infty}^{\infty} \delta(t - a) f(t)\, dx = f(a), \tag{3.6}$$

is used. A discrete version where $x = (k-1)\Delta x \;\; , k = 1,2,\ldots,N$ is for any temporal frequency and n^{th} trace:

$$S_n(\omega) = e^{-i\alpha n} \;\; , n = 1,2,\ldots,N \tag{3.7}$$

where $\alpha = \omega p \Delta x$. By combining S_n and S_{n-1} one can obtain the following recursion

$$S_n = P S_{n-1} \tag{3.8}$$

where $P = e^{-i\alpha}$. Equation 3.8 is a first order difference equation and can be used to recursively predict the signal along the spatial variable x. This principle can also be extended to a seismic section that consists of h complex harmonics (i.e., h linear events in t-x domain) where the difference equation of order h is given by

$$S_n = P_1 S_{n-1} + P_2 S_{n-2} + \ldots P_h S_{n-h}. \tag{3.9}$$

Algorithm

The algorithm for the f-x prediction filtering has been explained thoroughly by Galbraith (1991) and uses a complex Wiener filter to predict the signal for each frequency. The algorithm can be summarized as follows:

f-x prediction filter steps:

1. Transform the data from t-x to f-x domain by Fourier transform with respect to time.
2. For each frequency: Estimate the prediction filter by a complex wiener filter problem.
3. Apply the filter to the data.
4. Transform the data back from f-x to t-x domain.

Figure 3.4 shows f-x prediction onto a synthetic dataset with one straight and one dipping reflector with additive white noise. It recovers the dipping event quite well.

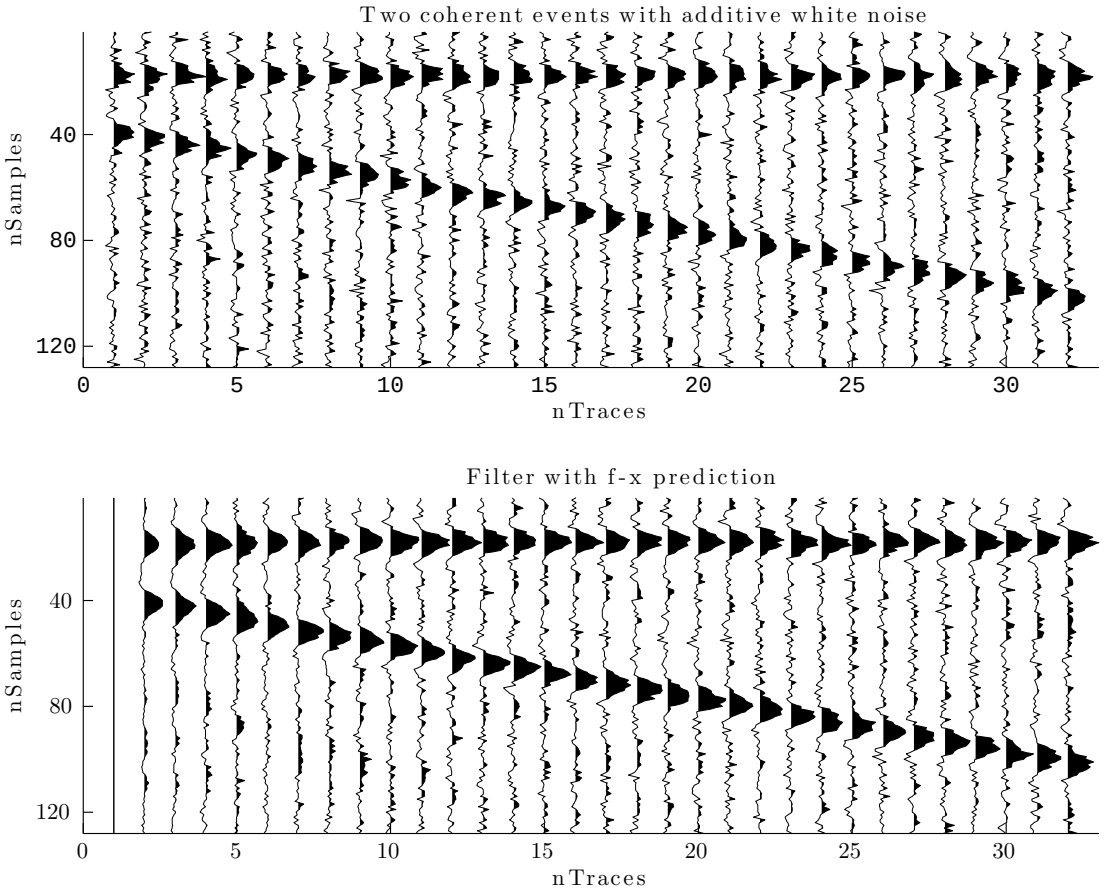

Figure 3.4: Synthetic example with additive zero-mean random noise of variance 0.2 (top) and with f-x prediction applied on the dataset (bottom).

Limitations

A limitation is that the signal model in this method assumes that the signal can be described by an autoregressive (AR) model (i.e., $S_n = PS_{n-1}$). The noise is then an innovative rather than an additive part of the signal. Soubaras (1994) was the first to see this inconsistency and proposed a technique named f-x projection filtering to overcome this problem. Sacchi and Kuehl (2001) addressed the same problem by modelling the signal with an autoregressive-moving average (ARMA) model and obtained similar results as Soubaras (1994). These methods will not be covered in this thesis.

3.2.5 Rank reduction techniques (SVD)

In this section a powerful linear algebra tool called singular value decomposition (SVD) is presented. SVD is used to estimate the rank of huge matrices and for rank-reduction of matrices. SVD is widely used in applied linear algebra like image processing and signal processing.

One of the main tool used in this thesis is the f-x Cadzow filter (Cadzow, 1988; Trickett, 2008) that uses SVD for rank-reduction. So, for the sake of clarity of the next chapter, SVD will here

be presented as an independent filtering technique (Bekara and van der Baan, 2007; Manolakis et al., 2005).

Mathematical description

Any matrix can be decomposed into a diagonal matrix such that

$$\mathbf{A} = \mathbf{U}\Sigma\mathbf{V}^H \tag{3.10}$$

where $\mathbf{A}$ is a matrix of dimension $m \times n$ with rank r, $\mathbf{U}$ and $\mathbf{V}$ are orthogonal matrices with dimensions $m \times m$ and $n \times n$ respectively. Σ is a $m \times n$ matrix on the form

$$\Sigma = \begin{bmatrix} D & 0 \\ 0 & 0 \end{bmatrix} \tag{3.11}$$

where D is an $r \times r$ diagonal matrix consisting of the r singular values of $\mathbf{A}$, with diagonal elements: $\sigma_1 \geq \sigma_2 \geq \ldots \geq \sigma_r > 0$. H denotes the hermitian transpose or more self-explanatory conjugate transpose.

Another way of representing the matrix $\mathbf{A}$ is as a set of eigenimages $\mathbf{I}_i$ such that

$$\boldsymbol{A} = \mathbf{I}_1 + \ldots + \mathbf{I}_r \tag{3.12}$$

where

$$\boldsymbol{I}_i = \sigma_i \mathbf{u}_i \mathbf{v}_i^H = \sigma_i \begin{bmatrix} u_{i,1} \\ \vdots \\ u_{i,m} \end{bmatrix} \begin{bmatrix} \overline{v_{i,1}} & \ldots & \overline{v_{i,n}}. \end{bmatrix} \tag{3.13}$$

σ_i denotes the i-th singular value, $\mathbf{u}_i$, the i-th column of $\mathbf{U}$ and $\boldsymbol{v}_i$, the i-th column of $\mathbf{V}$. $\overline{v_{i,j}}$ denotes the conjugate of $v_{i,j}$.

Physical interpretation

The singular values σ_i are measures of the lateral correlation, i.e., how correlated events are from trace to trace. Hence, a laterally coherent event will have a high singular value. Since the singular values are sorted in decreasing order such that $\sigma_1 \geq \sigma_2 \geq \ldots \geq \sigma_r \geq 0$, then the first eigenimages consist of laterally coherent signals while the latter ones are associated to random noise as the degree of correlation is low.

This is best illustrated by an example. Figure 3.5 shows a picture of a noisy T, that has been decomposed into its eigenimages by SVD. We can see that the first two eigenimages contain the laterally coherent T, while the other eigenimages contain noise. By displaying the image as eigenimages, as in Figure 3.5, one can understand why rank reduction is used in noise attenuation as it separates the noise from the signal.

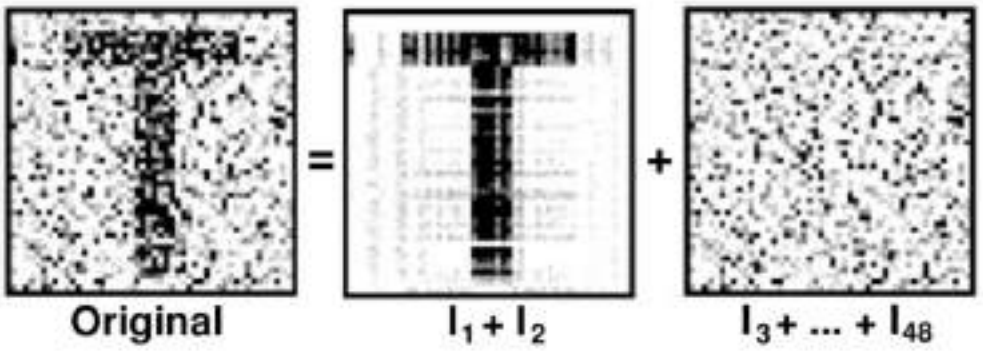

Figure 3.5: A 48x48 pixel picture showing a noisy T and its eigenimages. One can see that laterally coherent signals will be captured in the first two eigenimages and the noise is in the following eigenimages. Taken from Trickett (2003).

Algorithm

Typically the desired signal is represented by the first eigenimages, while unwanted noise is confined in the latter ones. Therefore, keeping the first k^{th} eigenimages, with $0 < k < r$, creates a rank reduced matrix $\mathbf{F}_k(\mathbf{A})$:

$$\mathbf{F}_k(\mathbf{A}) = \mathbf{I}_1 + \ldots + \mathbf{I}_k . \tag{3.14}$$

Figure 3.6a shows us an example containing one flat and laterally coherent event with additive random noise (top). By keeping only the first eigenimage, i.e., $k = 1$, we observe that the flat event is successfully estimated (bottom). In Figure 3.6b a dipping coherent event has been added to the data (top). By keeping the two first eigenimages, i.e, $k = 2$, the laterally coherent event is preserved, but the dipping event is attenuated. Bekara and van der Baan (2007) have solved this issue by using SVD for a local window where dip steering has been applied for dipping events. Trickett (2003) solves it by first transforming the data into the f-x domain and then performing the SVD on the transformed data.

3.3 Noise attenuation techniques used in de-blending

3.3.1 f-x Cadzow filter

f-x Cadzow filter is an improved version of the Cadzow filter (Cadzow, 1988), presented by Trickett (2008). The f-x Cadzow filter is also known under the name Singular Spectrum Analysis (SSA) which was derived in parallel to the f-x Cadzow, but from scientists working with

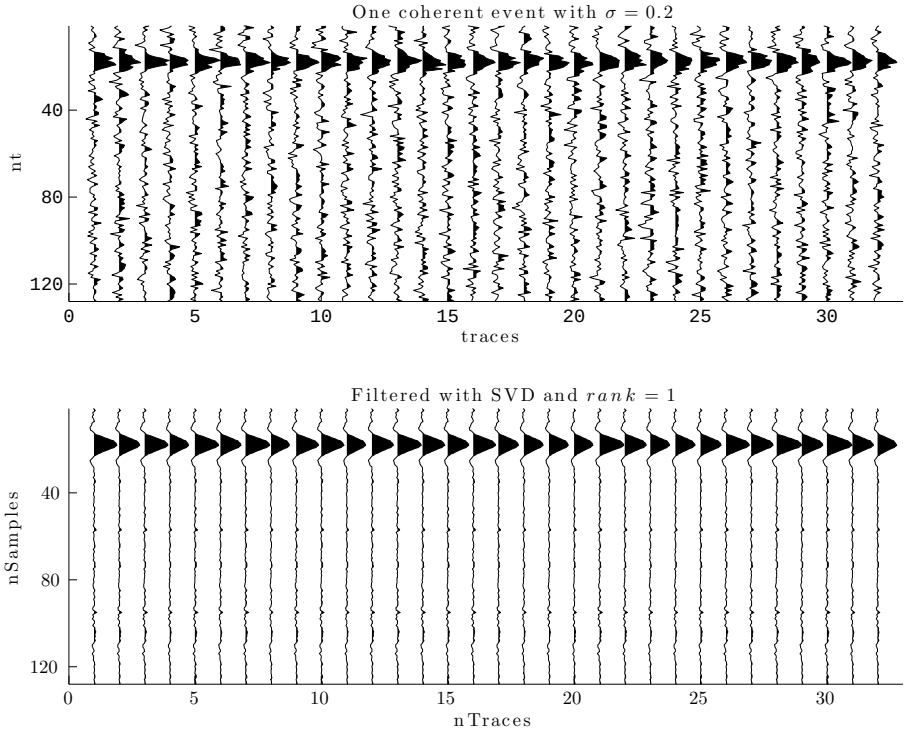

(a) SVD example 1. Input (top) and output (bottom).

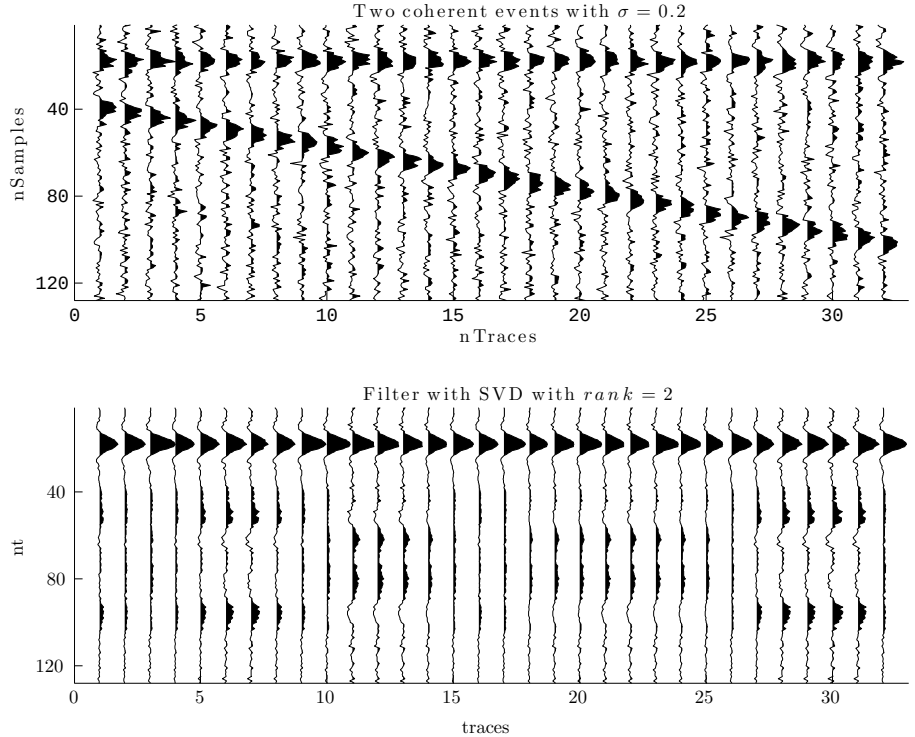

(b) SVD example 2. Input (top) and output (bottom).

Figure 3.6: (a) Synthetic example of the SVD acting in the t-x domain on a flat event with additive white noise with variance, $\sigma^2 = 0.2$. The data was rank-reduced to rank 1. (b) Synthetic example of the SVD acting on a falt and a dipping event in t-x domain.

dynamical systems as a method for rank reduction of 1D time-series (Broomhead and King, 1986; Vautard and Ghil, 1989) instead of as a image processing technique. This section will present the algorithm for the f-x Cadzow filter and its physical interpretations.

Algorithm

In Figure 3.7 the algorithm is presented as done by Trickett (2008). First the data is transformed from t-x to f-x domain using a digital Fourier transform (DFT). Then for every frequency slice, i.e., one frequency for all the traces, the complex values $c_1, c_2, \ldots, c_n$ are placed into a matrix where all the entries are constant along the anti-diagonals, i.e., a Hankel matrix,

$$\mathbf{H} = \begin{bmatrix} c_1 & c_2 & \ldots & c_{n-m+1} \\ c_2 & c_3 & \ldots & c_{n-m+2} \\ \vdots & \vdots & \ddots & \vdots \\ c_m & c_{m+1} & \ldots & c_n \end{bmatrix}. \tag{3.15}$$

By editing m, the matrix dimension can be controlled. Usually m is set to $m = n/2$ making the Hankel matrix as square as possible. For example, if the frequency slice contains 7 traces, then the Hankel matrix $\mathbf{H}$ would be

$$\mathbf{H} = \begin{bmatrix} c_1 & c_2 & c_3 & c_4 \\ c_2 & c_3 & c_4 & c_5 \\ c_3 & c_4 & c_5 & c_6 \\ c_4 & c_5 & c_6 & c_7 \end{bmatrix}.$$

Thereafter the rank of the Hankel matrix is reduced by applying SVD (cf. section 3.2.5) denoted by the operator $\mathbf{F}_k$ such as:

$$\widetilde{\mathbf{H}} = \mathbf{F}_k(\mathbf{H}). \tag{3.16}$$

The rank reduced matrix is not longer constant along the anti-diagonals so by averaging the anti-diagonals the Hankel structure is recovered. The filtered complex values, $\hat{c_1}, \hat{c_2}, \ldots, \hat{c_n}$ are then extracted, and we repeat the process for the next frequency. Once all the frequencies have been filtered, one can take the inverse DFT to obtain the data in t-x domain.

Theoretical insight

f-x Cadzow, as well as the f-x prediction filter is based on the fact that linear events in t-x domain are predictable in the f-x domain as detailed in section 3.2.4. The reasons for forming a Hankel matrix is that pure signals are usually low in rank. Specifically if the data contains h dips, $c_1, c_2, \ldots, c_n$ are the sum of h complex sinusoids, and if $c_1, c_2, \ldots, c_n$ is the sum of h complex sinusoids, the Hankel matrix, $\mathbf{H}$, has rank h. Consider a simple seismic dataset only containing

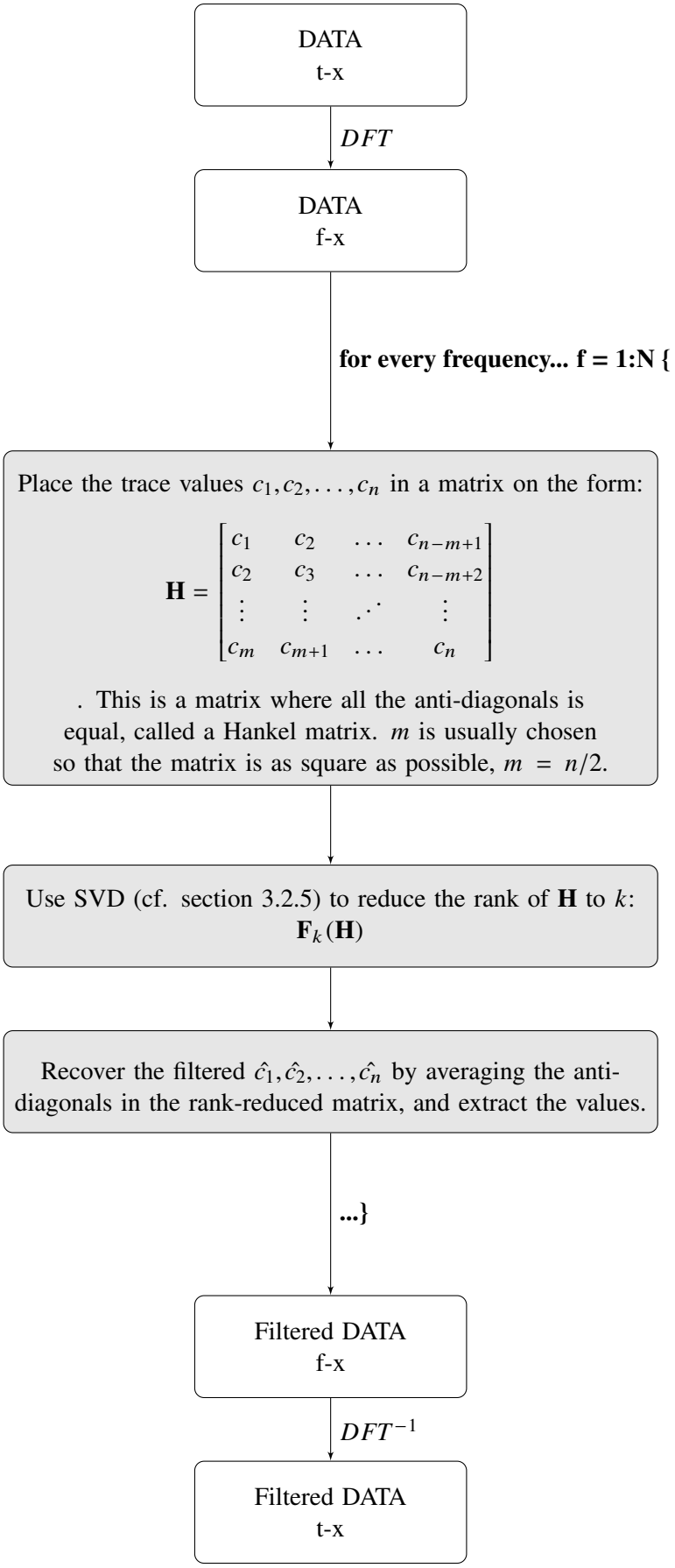

Figure 3.7: Flow chart explaining the steps in a f-x Cadzow filter.

one single event and seven traces. The Hankel matrix would then be,

$$\mathbf{H} = \begin{bmatrix} c_1 & c_2 & c_3 & c_4 \\ c_2 & c_3 & c_4 & c_5 \\ c_3 & c_4 & c_5 & c_6 \\ c_4 & c_5 & c_6 & c_7 \end{bmatrix} = \begin{bmatrix} c_1 & Pc_1 & P^2c_1 & P^3c_1 \\ Pc_1 & P^2c_1 & P^3c_1 & P^4c_1 \\ P^2c_1 & P^3c_1 & P^4c_1 & P^5c_1 \\ P^3c_1 & P^4c_1 & P^5c_1 & P^6c_1 \end{bmatrix}. \tag{3.17}$$

where the relation $S_n = PS_{n-1}$ in Eq. (3.8) has been used. The rank of this Hankel matrix is 1. In case of additive noise, the rank will be larger than one, but it can be reduced by rank reduction. The data is therefore only retaining coherent signals. The larger the rank k is chosen, the more dips can be recovered, but the lower the noise-suppression will be. Therefore the choice of rank should be data-dependent.

Examples

Figure 3.8a shows one flat and one dipping event with additive zero-mean random noise of variance, σ^2, of 0.2 (top). The f-x Cadzow filter is applied to the synthetic dataset by reducing the rank of the Hankel matrices to 2, equivalent to keeping the two first eigenimages (bottom). Figure 3.8b shows the same example as in Figure 3.8a but with additive random noise with a variance, σ^2, of 0.6 (top). In this case the f-x Cadzow (bottom) attenuates the noise in similar proportion as in Figure 3.8a.

Figure 3.9 shows the seven first eigenimages of a common offset section containing blending noise. The signal is contained in the three first eigenimages while the blending noise is contained in the latter ones. By looking at the energy distribution in Figure 3.10 one can see that most of the energy is contained in the first three eigenimages. Thus, by for example only keeping the first two eigenimages, equivalent to reduce the rank of the Hankel matrices to 2, most of the blending noise is attenuated (Figure 3.11). It is noticeable that the f-x Cadzow is trying to find coherency between the blending noise seen as parallel lines in the computed sliding windows. Areas where no signal is present are contaminated by noise due to the averaging nature when reconstructing the rank reduced Hankel matrices. Edge effects between the overlapping windows are also present and could be dampened by an averaging scheme of the overlapping windows.

Limitations

f-x Cadzow is a powerful technique and can be expanded to multiple dimensions as shown by Trickett (2008). The only drawback is the computational cost of forming Hankel matrices and rank-reducing them by SVD for every frequency. A solution to this problem is to use R-SVD, i.e., Randomized-SVD to speed up the SVD. The downsides are that this method is not elegant as it destroys symmetry and is an approximation.

Furthermore, edge effects are present for the end traces due to end values are not affected by the averaging in the Hankel matrix. Noise-free areas have been contaminated by small amount

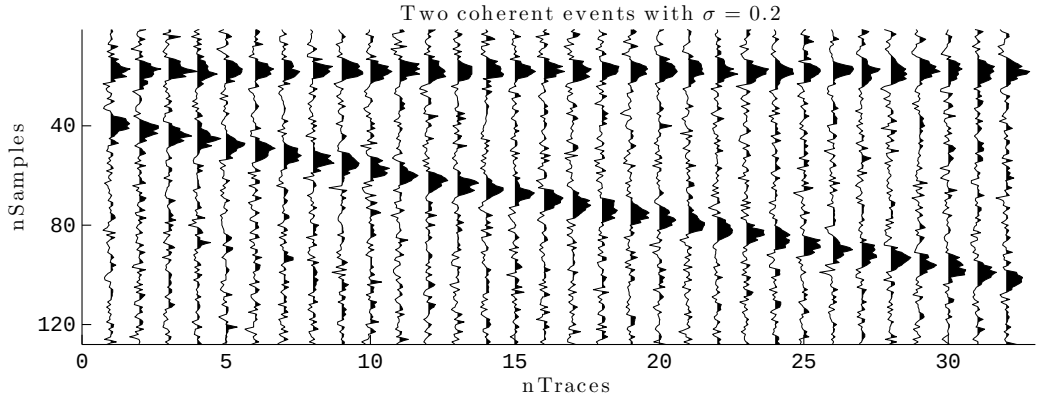

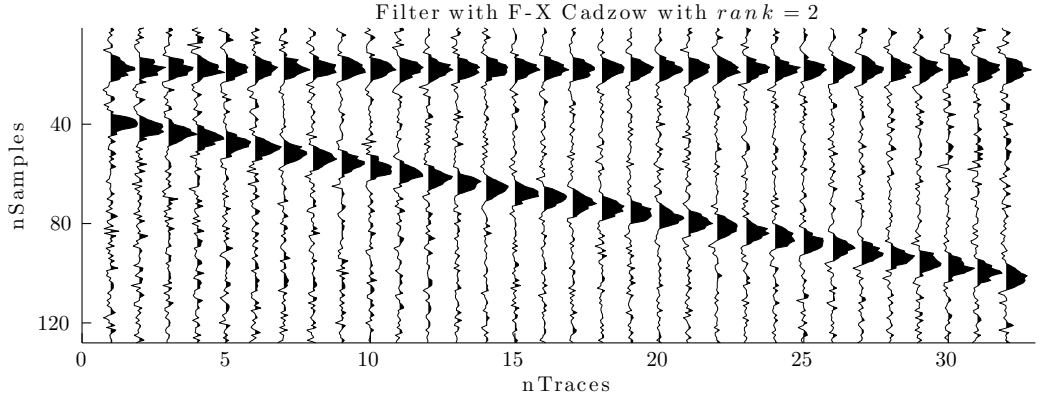

(a) Cadzow: Synthetic example 1

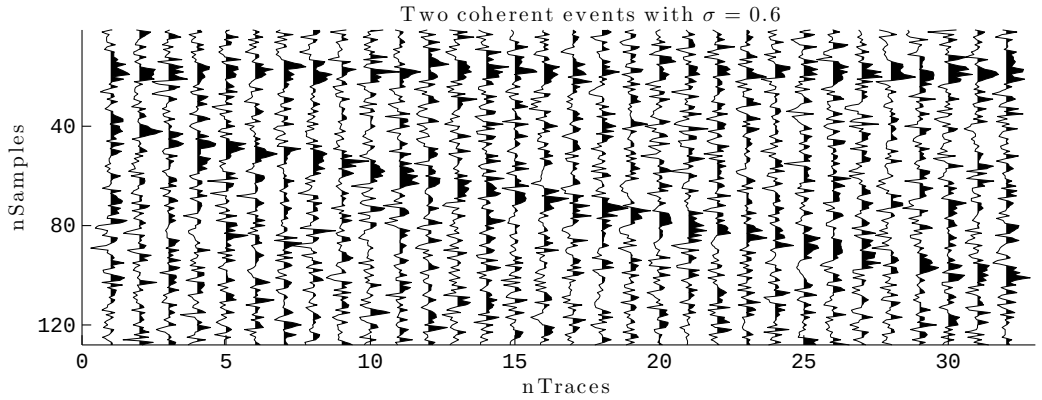

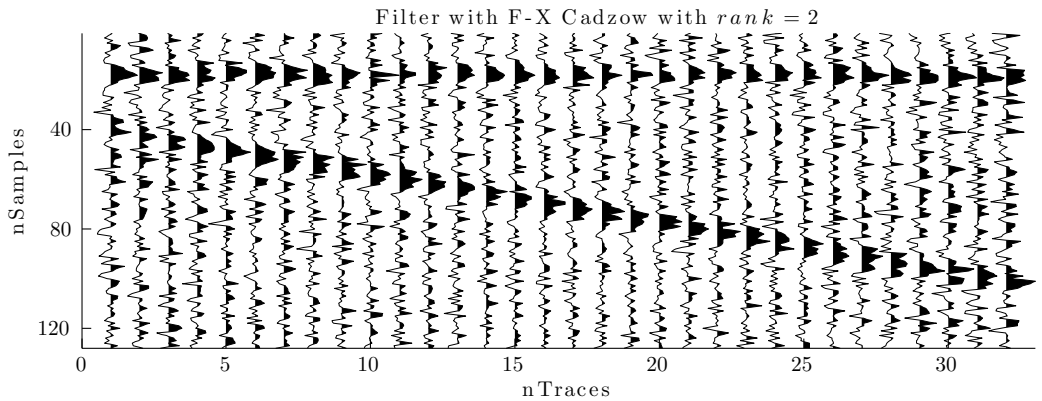

(b) Cadzow: Syntethic example 2

Figure 3.8: (a) f-x Cadzow applied on a synthetic example with one straight and one dipping event and noise of $\sigma^2 = 0.2$ added. (b) f-x Cadzow applied on a synthetic example with one straight and one dipping event and noise of $\sigma^2 = 0.6$ added.

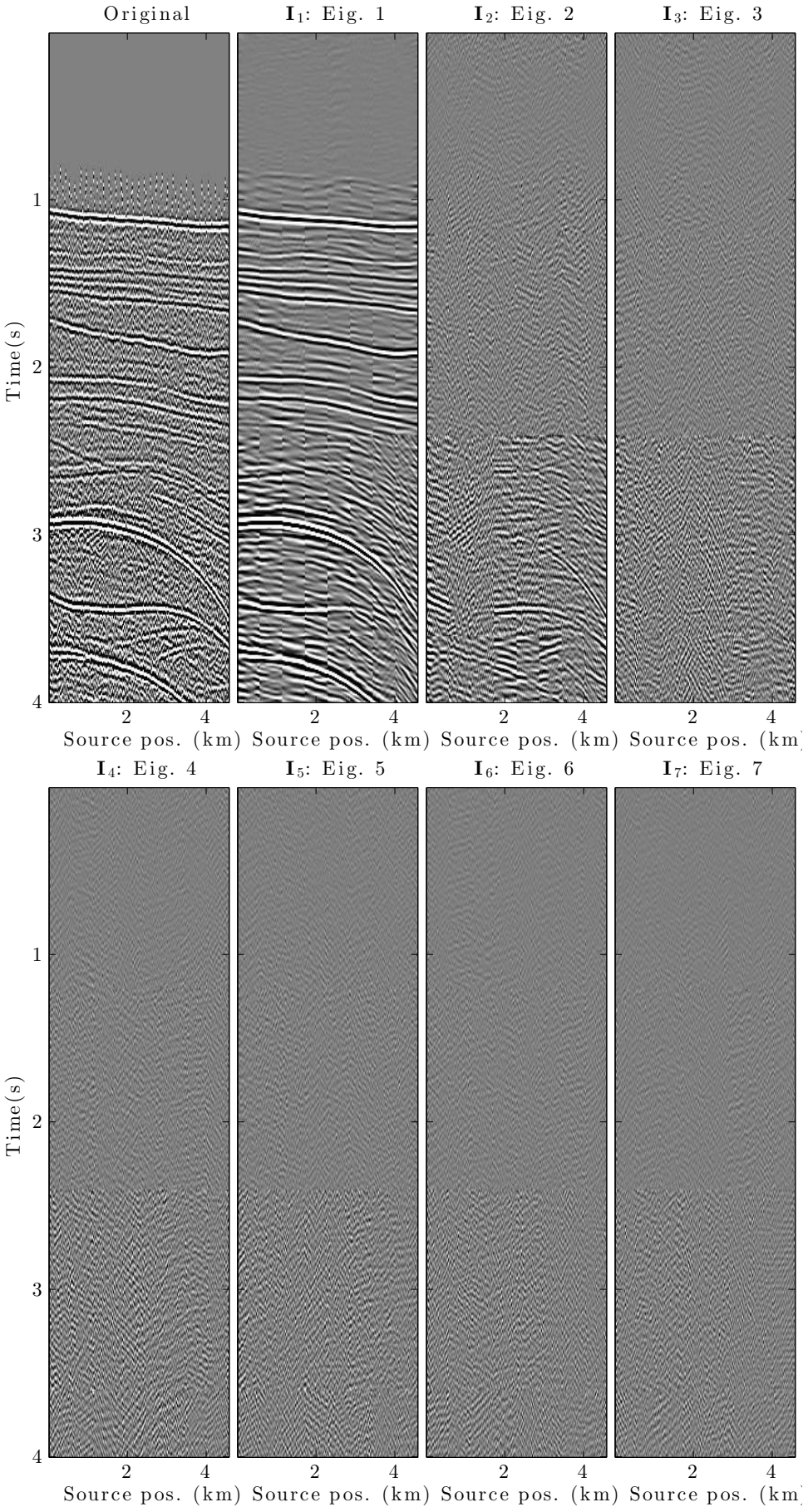

Figure 3.9: Different eigenimages for a common offset section containing blending noise.

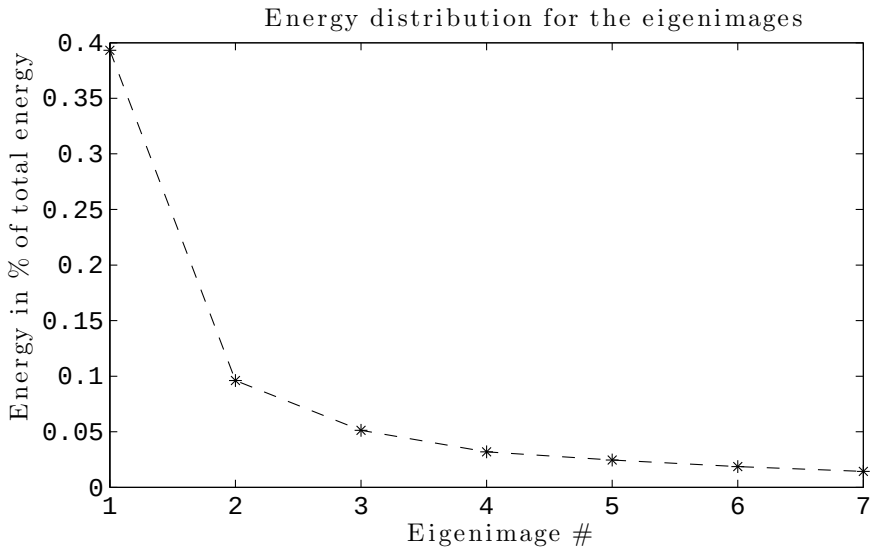

Figure 3.10: Energy distribution for the different eigenimages in Figure 3.9.

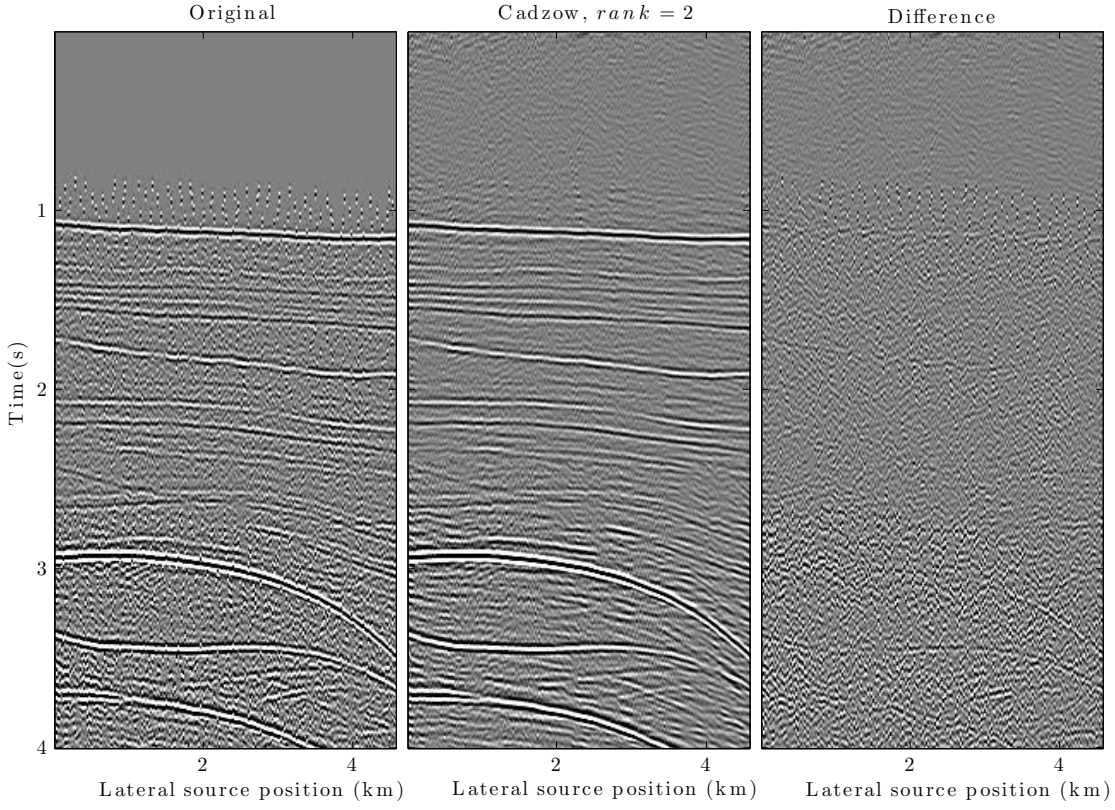

Figure 3.11: Rank reduction to rank = 2 on a common offset section containing blending noise.

of noise after filtering, due to the averaging scheme in the reconstruction of the rank reduced Hankel matrix.

3.3.2 Time frequency de-noising (TFDN)

Time frequency de-noising (TFDN), also known as a "time and space varying median filter", was introduced by Vassiliou and Garossino (1998) and later improved by Elboth et al. (2008). It is a powerful technique in de-noising a broad range of noise. This section details the implementation of the TFDN technique and provides examples in a common offset section containing blending noise.

TFDN works by using a sliding window, both in time and space. The window containing all traces and nY samples is multiplied by a window function, to suppress Gibbs phenomena, and then transformed from time- to frequency domain. Every frequency slice is then checked for amplitude anomalies by a 1D window containing nX traces. The 1D window is moving one trace at the time and contains a odd number of samples for symmetry. The amplitude of the middle sample is then compared against the median value contained in the 1D window. If the amplitude value of the middle sample is *tFactor* larger than the median, then the amplitude of the middle sample is scaled down to the amplitude of the median value. The data is then transformed back to the time domain and only the center of the window is kept. Then the whole window is moved down one sample and the process is repeated until the whole dataset has been run through.

For the implementation in MATLAB, the data has not been zero padded. Therefore the data is not filtered in the top and bottom $nY/2$ samples, and in the first and last $nX - ceil(\frac{nX}{2})$ samples, where $ceil$ is the operator that always rounds numbers towards infinity. For example, if $nX = 3$; $3 - ceil(3/2) = 1$, the first and last traces are left untouched. Furthermore the window is moved 3 samples at the time and the three middle samples of the window are kept. The goal is to speed up the filter.

Tests run on a common offset section containing blending noise suggest that the *tFactor* should be 2.

Figure 3.12 shows us an example of TFDN run on a synthetic common offset section with $nX = 3$, $nY = 64$ and $tFactor = 2$. Only small amounts of the blending noise have been filtered away (right columnn).

3.3.3 Joint de-noising of multicomponent data

In this section, I present a method developed recently for the noise attenuation of multicomponent (MC) data: joint directional de-noising (Sanchis and Elboth, 2014). This method takes advantage of having both the pressure and MC sensors collocated, to guide the de-noising of MC data with good quality P-data. The MATLAB code for this method has been provided by

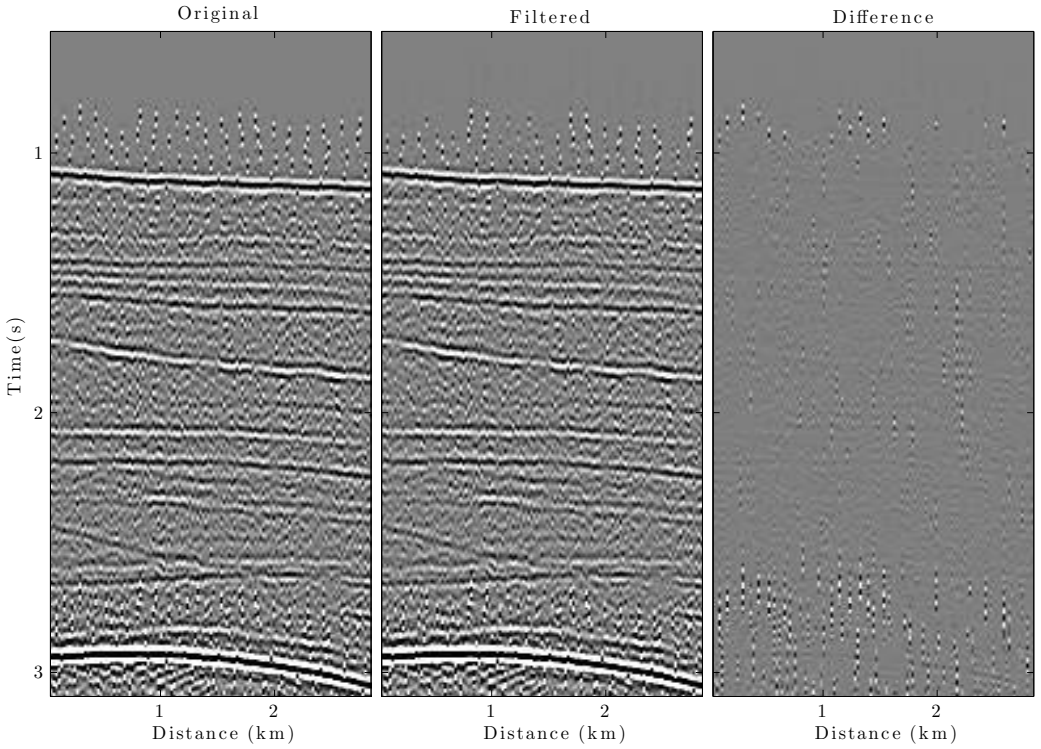

Figure 3.12: TFDN with $nX = 3$, $nY = 64$ and $tFactor = 2$.

Dr. Charlotte Sanchis. The details of this method is out of the scope of this thesis. Thus, only the workflow of the method is discussed.

Figure 3.13 presents the workflow of the processing sequence of the joint de-noising of MC-data using P-data as a guide. The raw P-data is de-noised and split into frequency bands. Then the raw MC-data is converted to pressure equivalent data, so amplitudes are comparable. Joint-directional de-noising is then performed. It consists of transforming the data to f-x domain. Each frequency slice of both the P- and MC-data is arranged into their respective Hankel matrix (cf. section 3.3.1). Decomposing the Hankel matrix of the P-data into eigenimages gives the directions of the signal. By mapping the MC-data Hankel matrix along the signal directions, given by the eigenimages of the P-data, we can estimate the MC-data complex values by least-squares fitting. Since the MC-data estimation could contain errors due to high amplitude noise that has the same direction as the signal, the estimation of the MC-data frequency slice needs to be done iteratively with a weighting scheme. When all the frequency slices have been processed, transfer the data back from the f-x to t-x domain by an inverse digital Fourier transform. Finally, apply a final standard de-noising method on the MC-data.

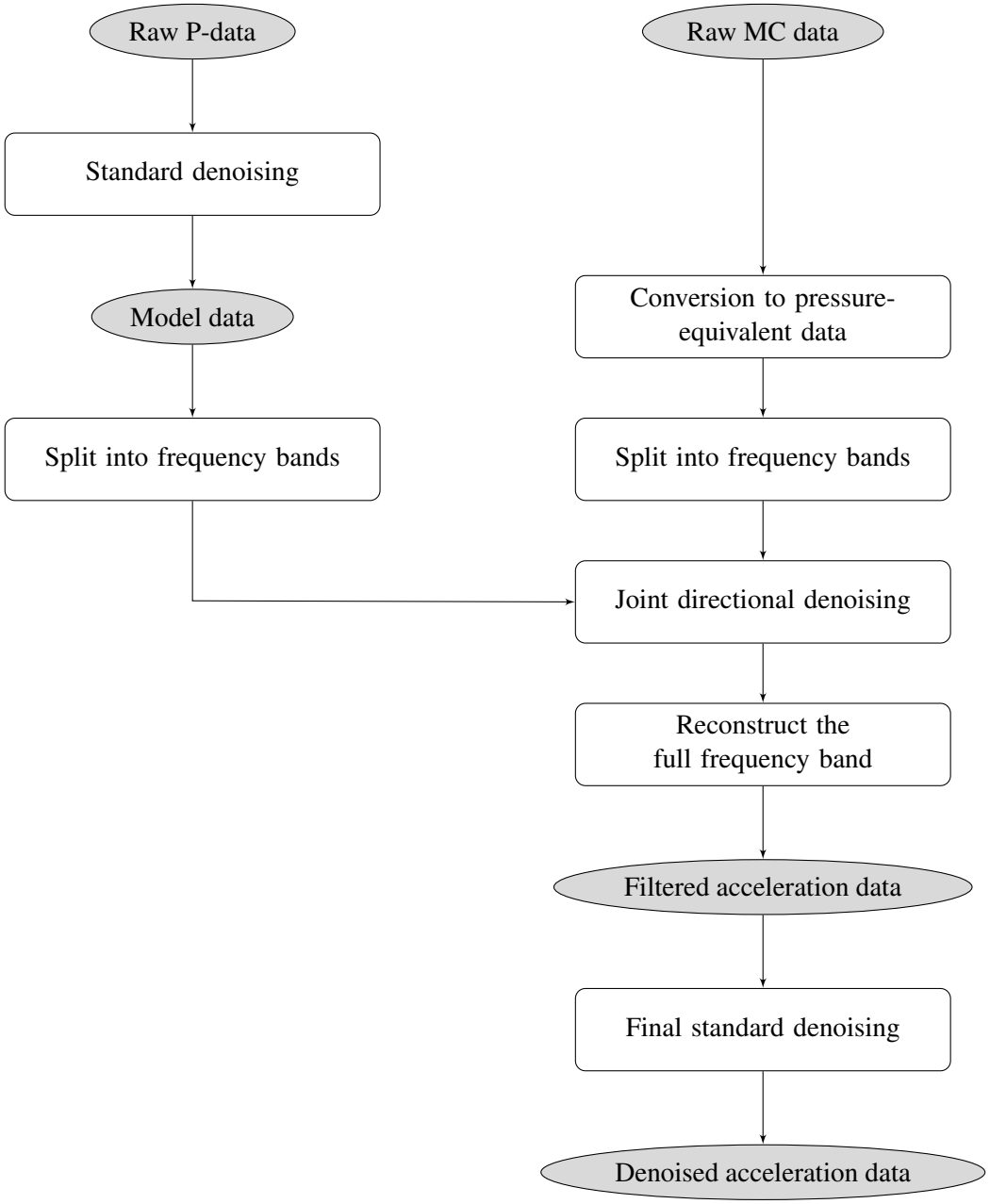

Figure 3.13: Workflow describing the joint de-noise of MC-data processing sequence. Taken from Sanchis and Elboth (2014).

4 De-blending of seismic data

4.1 Introduction

The main problem with blended data is the cross-talk between the sources, i.e, the blending noise. When each source is fired with random or quasi-random time-delay in respect to each other, the blending noise appears coherent in the common shot domain. However, the blending noise appears incoherent in the common receiver, common mid-point and common offset domain. Section 4.1 presents blended data in these domains.

Section 4.2 presents an iterative de-blending method of the P data similar to Mahdad et al. (2012), Maraschini et al. (2012) and Cheng and Sacchi (2013). This section is divided into four parts. First the general algorithm is presented. Then, two noise attenuation filters involved in the de-blending process are discussed: the f-x Cadzow in one hand, and a hybrid f-x Cadzow and time-frequency de-noising (TFDN) in the other hand. The f-x Cadzow and hybrid filters are then briefly compared on the synthetic dataset *Pluto* (Stoughton et al., 2001). Finally, some algorithmic aspects related to the method are given. The hybrid filter led to an EAGE student paper presented in Magnussen (2015).

In section 4.3 we take take advantage of the additional information provided by multicomponent (MC) data to improve the de-blending of P data. In that purpose, we propose a method for joint de-blending of P and MC data, that aims at improving de-blending of P data, as well as de-blending and de-noising MC data. Finally, a small section is dedicated the other attempts tested during the development of joint de-blending of P and MC data.

Blended seismic data in different domains

Before diving into the theory behind de-blending of seismic data, this section covers how blended data looks in different domains. This gives a better understanding of why some of these domains are chosen for de-blending blended data. To illustrate this section, we use the numerically blended dataset *Pluto* (Stoughton et al., 2001). In the numerically blended data, one source is shot as in conventional seismic while the other source is shot with a quasi-random time-delay for each shot.

Common shot (CS) domain displays all the traces recorded from one particular shot. Figure 4.1a shows a blended dataset that consists of two overlapping shots from two different sources. Both sources are coherent in CS domain, and are therefore difficult to separate.

Common receiver (CR) domain displays all the traces from one fixed receiver coordinates. Thus, each trace comes from a different shot coordinates. Since the random time delay varies from shot to shot, one source appears coherent, while the other source appears incoherent. The contribution from the incoherent source can be regarded as blending-noise for the other. In Figure 4.1b one source appears coherent while the blending-noise coming from the other source is incoherent.

Common mid-point (CMP) domain displays all the traces with the same mid-point. Figure 4.1c shows blended data in the CMP domain. Like in the CR domain, each trace from the CMP gather comes from a different shot coordinates, thereby turning the second source into incoherent noise.

Common offset (CO) domain displays all the traces with the same offset from source to receiver. A CO section can be seen as a brute stack of the data with fold of 1. As for the CR and CMP domain, each trace in the CO domain comes from a different shot coordinates. Thus, making one source coherent and the other source incoherent as shown in Figure 4.1d.

In the examples mentioned above, two sources are used. One source has a constant time-delay from shot to shot, while the other source has a quasi-random time-delay, which makes one source appear coherent and the other source incoherent in the CR, CMP and CO domains. By sorting the data to one of this domain, we turn the de-blending problem into a noise attenuation problem. I.e., applying an noise-attenuation technique to a blended CO, CR or CMP section removes energy from the other source. Furthermore, the time-delays for the other source are known, so, it is possible to decide which source to make coherent. These are the basics behind the algorithm presented in the following section.

In this thesis we choose to use the CO domain for the de-blending. As pointed out above, the CR or CMP could have been used as well. For example, Huo et al. (2012) use the CMP domain and Ibrahim and Sacchi (2013) use the CR domain in de-blending data.

Relation between common shot and common offset domain

Figure 4.2 illustrates the connection between the CS domain and the CO domain. Figure 4.2a shows all the shot gathers for one streamer put behind each other. If we now take a cross section that cuts all the shot gathers for one specific offset (red square in Figure 4.2a), we make the common offset section emphasized by a red square in Figure 4.2b. Repeating this for all offsets will sort the data to common offset domain (Figure 4.2b). The common offset domain will give us an image of the subsurface with a fold = 1. Conversely, to go back to the shot domain, we take a cross section that cuts all the different offsets for one specific shot number (green cross section in Figure 4.2b). This creates the shot marked by the green rectangle in Figure 4.2a.

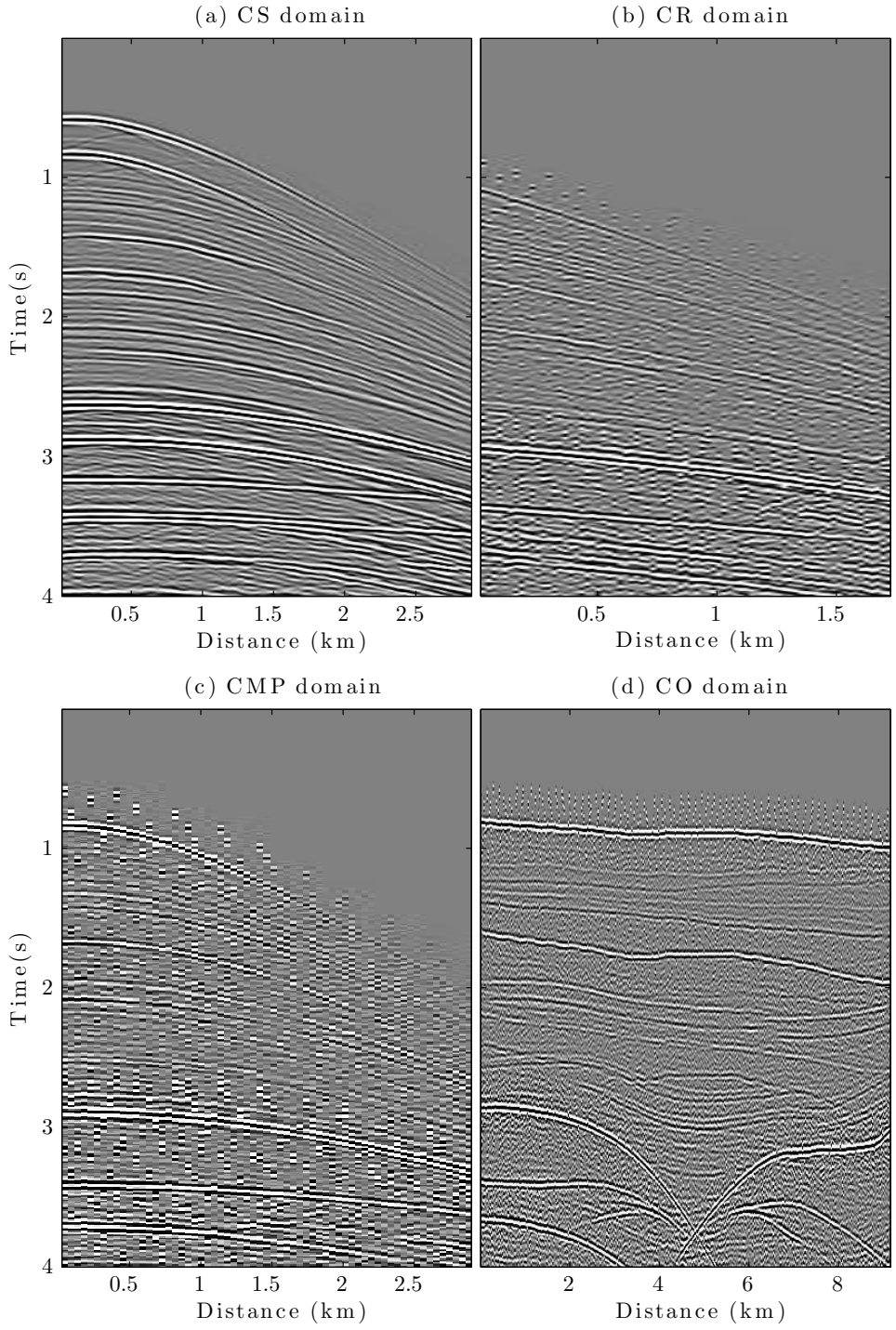

Figure 4.1: Blended data in different domains.

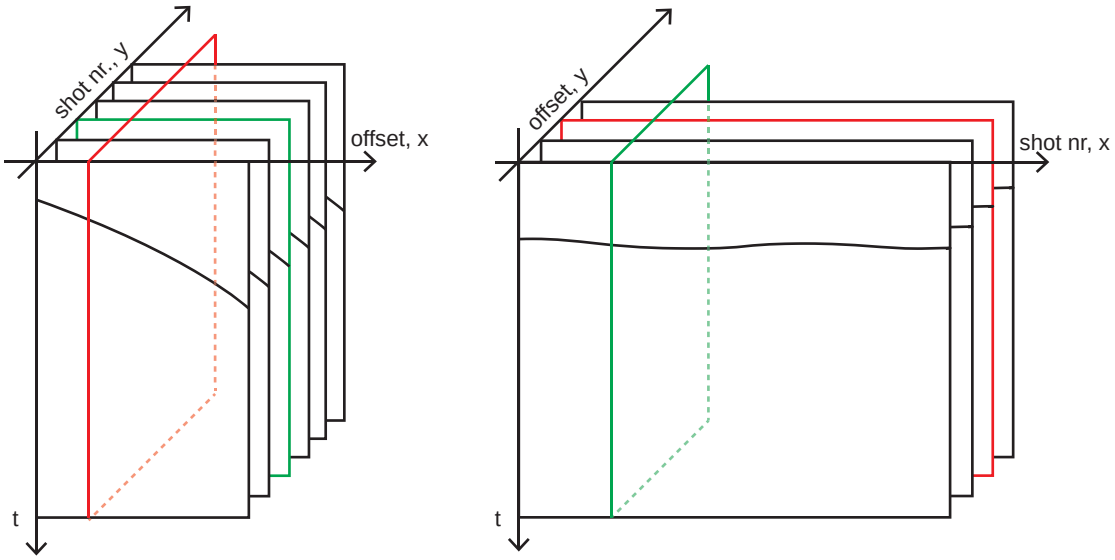

(a) Shot domain

(b) Common offset domain

Figure 4.2: Relation between shot domain and common offset domain.

Basically, going from shot domain to common offset domain is the same as rotating our matrix, containing all our shots, 90-degrees clockwise around the z-axis.

4.2 De-blending of P data

4.2.1 General algorithm

The principle behind the method presented in this section is similar to Mahdad et al. (2012), Maraschini et al. (2012) and Cheng and Sacchi (2013). It is based on the principle that one shot is time-shifted with a random time-delay relative to the other. These time-delays are known so that by proper time shifting one can switch between which of the two simultaneous source contributions being coherent after sorting into the common-offset domain. Assume a blended acquisition with two shooting vessels and let the recorded seismic data, $\mathbf{D}$, be written formally as

$$\mathbf{D} = \mathbf{D}_1 + T_2(\mathbf{D}_2), \tag{4.1}$$

where $\mathbf{D}_i$ is the data from the i^{th} source without delay and T_2 is the time-shift operator which shifts each trace of $\mathbf{D}_2$ relative to $\mathbf{D}_1$ with its respective time-shift. $\mathbf{D}$ is considered to be marine data acquired by a single streamer and with the second simultaneous source attached to a nearby shooting vessel. These combined data can be sorted into the time-offset-shot (t-x-y) space for further processing. It follows from Eq.(4.1) that the data associated with source 1 is not time-shifted (e.g. $T_1(\mathbf{D}_1) = \mathbf{D}_1$). If the time-shift operator T_2^{-1} is applied to $\mathbf{D}$ we obtain,

$$T_2^{-1}(\mathbf{D}) = \mathbf{D}_2 + T_2^{-1}(\mathbf{D}_1), \tag{4.2}$$

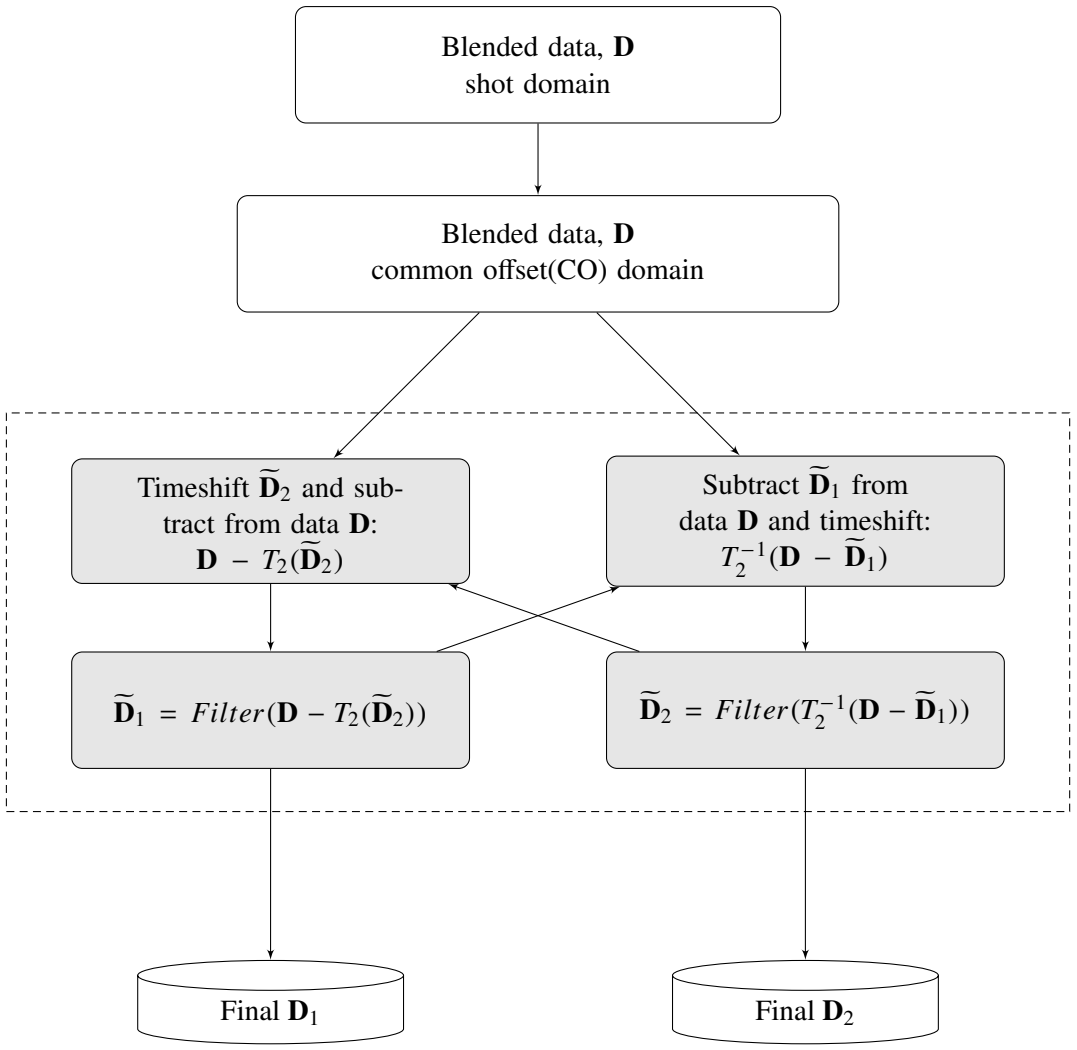

Figure 4.3: Flowchart of the iterative estimation and subtraction de-blending of P data.

where $\mathbf{D}_2$ now appears coherent in the common offset domain while the other term $T_2^{-1}(\mathbf{D}_1)$ appears in a random fashion due to the time-shifting operator T_2^{-1}. The de-blending method employed here makes use of an iterative estimation and subtraction approach that gradually recovers each individual source contribution as described schematically in Figure 4.3. Initially the estimates for sources 1 and 2, $\widetilde{\mathbf{D}}_1$ and $\widetilde{\mathbf{D}}_2$ respectively, are set to zero. Then for every iteration and both sources, the estimation of the complementary simultaneous source is subtracted. Next, application of a filter (cf. section 4.2.2) attenuates the events made random by the time-shifting operator while preserving the coherent ones. Thus, if working perfectly, this de-blending scheme will leave us with decomposed responses associated with the two sources. In practice an iterative process is needed until an appropriate exit criterion has been reached. Finally, the residuals are added back into both final estimates, as the residuals may contain data of interest. For illustration purposes, the first 4 iterations are detailed in example 4.1.

Example 4.1. *The first 4 iterations of the de-blending for two sources.*
$\widetilde{\mathbf{D}_{1,0}} = 0$
$\widetilde{\mathbf{D}_{2,0}} = 0$
$i = 1$*:*
$\widetilde{\mathbf{D}}_{1,1} = Filter(\mathbf{D} - \widetilde{\mathbf{D}_{1,0}}) = Filter(\mathbf{D}_1 + T_2(\mathbf{D}_2 - \widetilde{\mathbf{D}}_{2,0}))$
$\widetilde{\mathbf{D}}_{2,1} = Filter(T_2^{-1}(\mathbf{D} - \widetilde{\mathbf{D}}_{1,1})) = Filter(\mathbf{D}_2 + T_2^{-1}(\mathbf{D}_1 - \widetilde{\mathbf{D}}_{1,1}))$
$i = 2$*:*
$\widetilde{\mathbf{D}}_{1,2} = Filter(\mathbf{D} - T_2(\widetilde{\mathbf{D}}_{2,1})) = Filter(\mathbf{D}_1 + T_2(\mathbf{D}_2 - \widetilde{\mathbf{D}}_{2,1}))$
$\widetilde{\mathbf{D}}_{2,2} = Filter(T_2^{-1}(\mathbf{D} - \widetilde{\mathbf{D}}_{1,2})) = Filter(\mathbf{D_2} + T_2^{-1}(\mathbf{D}_1 - \widetilde{\mathbf{D}}_{1,2}))$
$i = 3$*:*
$\widetilde{\mathbf{D}}_{1,3} = Filter(\mathbf{D} - T_2(\widetilde{\mathbf{D}}_{2,2})) = Filter(\mathbf{D}_1 + T_2(\mathbf{D}_2 - \widetilde{\mathbf{D}}_{2,2}))$
$\widetilde{\mathbf{D}}_{2,3} = Filter(T_2^{-1}(\mathbf{D} - \widetilde{\mathbf{D}}_{1,3})) = Filter(\mathbf{D}_2 + T_2^{-1}(\mathbf{D}_1 - \widetilde{\mathbf{D}}_{1,3}))$
$i = 4$*:*
$\widetilde{\mathbf{D}}_{1,4} = Filter(\mathbf{D} - T_2(\widetilde{\mathbf{D}}_{2,3})) = Filter(\mathbf{D}_1 + T_2(\mathbf{D}_2 - \widetilde{\mathbf{D}}_{2,3}))$
$\widetilde{\mathbf{D}}_{2,3} = Filter(T_2^{-1}(\mathbf{D} - \widetilde{\mathbf{D}}_{1,4})) = Filter(\mathbf{D}_2 + T_2^{-1}(\mathbf{D}_1 - \widetilde{\mathbf{D}}_{1,4}))$

Figure 4.4 shows the first iteration of the algorithm tested on a synthetic CO section containing signals from two blended sources shot with random time-delays. As explained above, we first subtract the contribution from the second source, in the first iteration this contribution is zero. A noise attenuation filter is employed and the first estimate from source 1 is obtained. Both the estimate of source 1 and the original data are time-shifted into time-configuration 2. The blending noise created by source 1 is subtracted from the original data and then filtered to obtain an estimate of source 2. By time-shifting estimate 2 into time-configuration 1, a noise model has then been created for source 2. The process is then repeated, with an estimate of the second source that is improved at each iteration. This will again lead to a better estimation for source 1 and therefore a better estimation for source 2, and so on, until convergence.

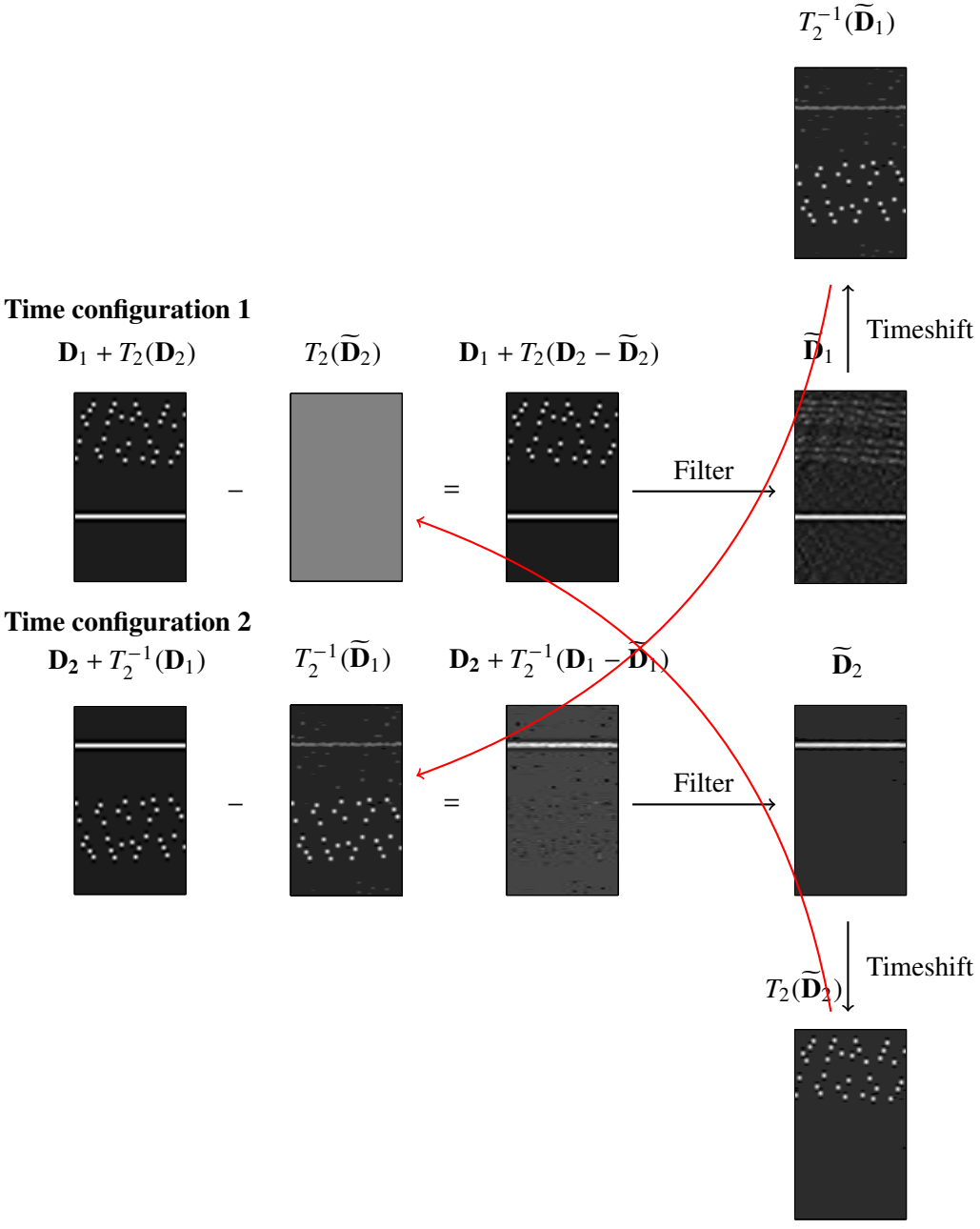

Figure 4.4: Flowchart of the iterative estimation and subtraction showing a synthetic CO section with one straight reflector.

4.2.2 Filters

We test two possible filters for the attenuation of the random events created by the time-shifting operator: a f-x Cadzow and a hybrid TFDN/f-x Cadzow filter. The f-x Cadzow (cf. section 3.3.1) filter has proven to be efficient in removing blending noise as shown by Maraschini et al. (2012) and Cheng and Sacchi (2013). The hybrid filter is inspired by Mahdad (2012) where a hybrid f-k and median filter is used and Huo et al. (2012) and Chen (2014) who use a median filter on CMP sections. The selected filters are run in overlapping windows on CO sections. The size of the window is usually set two 25 traces and 256 samples with a window overlap of 25 %.

f-x Cadzow

Different parameterization to run the f-x Cadzow in an iterative manner can be set. The main parameter for the f-x Cadzow filter is the number of eigenimages. This could either be held constant or be incremented for each iteration. Tests suggest that an incremental approach gives the best results.

Hybrid f-x Cadzow and TFDN filter

The motivation for combining the f-x Cadzow and TFDN filters is the belief that implementing a TFDN filter could lead to faster convergence and remove more blending noise in the process.

We propose two ways to combine a f-x Cadzow and TFDN filter. In the first approach, approach 1, the TFDN and f-x Cadzow alternate between each other for every i^{th} iteration. The second approach, approach 2, uses TFDN as a pre-processing tool on these input data. The TFDN filtered input data are then de-blended using the f-x Cadzow filter. Figure 4.5 shows flowcharts for the two approaches. In the second approach, it is crucial that the TFDN targets blending noise only and leaves the signal untouched.

4.2.3 Brief comparison between f-x Cadzow and the hybrid filter

As one of the goal of this thesis is to benchmark the novel joint deblending method with the best possible deblending results achieved with P data only, we present in this section a brief comparison of the f-x Cadzow and hybrid f-x Cadzow/TFDN. The filter that proves to give the best results on synthetic data, will be taken further to process a full semi-synthetic dataset from offshore the Faroe islands. Furthermore, it will be used as benchmark to evaluate the joint de-blending of P data and MC data.

The filters are tested on the window depicted in Figure 4.6. The window is taken from one common offset section of the synthetic dataset *Pluto*, which has been numerically blended with a quasi-random time-shift of -250 to 250 ms. The window consists of an outer-window that is

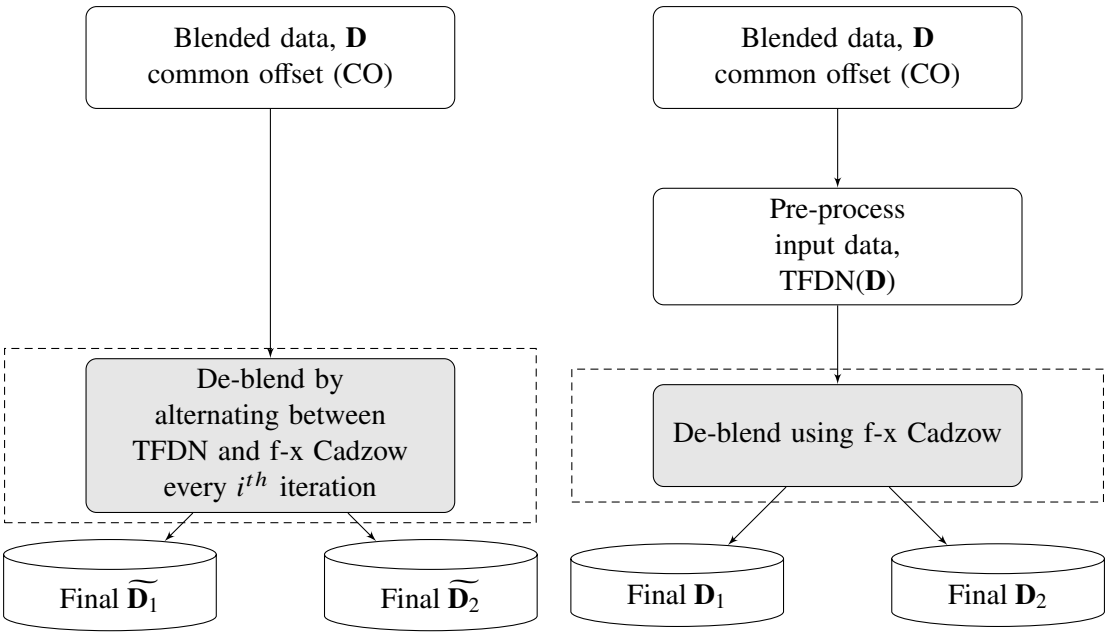

Figure 4.5: Two possible ways to combine TFDN and f-x Cadzow. (left) Approach 1: Alternating between TFDN and f-x Cadzow. (right) Approach 2: Using TFDN as a pre-processing tool

50 % larger than the inner window of 512 samples and 25 traces. For a quantitative measure of the correctness of the filters the root mean square (RMS), defined as

$$RMS(\mathbf{X}) = \sqrt{\frac{1}{N}\sum_{i=1}^{N} x_i^2}, \tag{4.3}$$

is calculated of the difference between the estimate and the original unblended data for the inner window for each iteration.

The f-x Cadzow filter and two approaches of the hybrid filter, are tested on the window shown in Figure 4.6. The black rectangle in the CO plane is the window to the right. Parameters used for the three approaches were decided upon testing and are provided in table 4.1. The f-x Cadzow filter in each approach was incremented by one at each iteration, going from 1 to 8. The iterative process ends when the residuals energy does not change more than 1 % or if the maximum number of iterations set to 50 is reached. T_f is the threshold factor for the TFDN filter, while nX_{Median} and nY_{Median} is the size of the horizontal and vertical sliding window respectively. Table 4.1 also provides the number of iterations taken before convergence are noted with i. RMS is the last RMS value between the residuals of estimated and original unblended data. Time denotes the total amount of run-time. Figure 4.7 shows the RMS value of the residuals between estimates and unblended data for each iteration. For approach 1, the iterative process stops at 50 iterations, meaning that the method either never converges or converge too slowly. For approach 2, the method converges fast, but the end result is not satisfactory. Using f-x

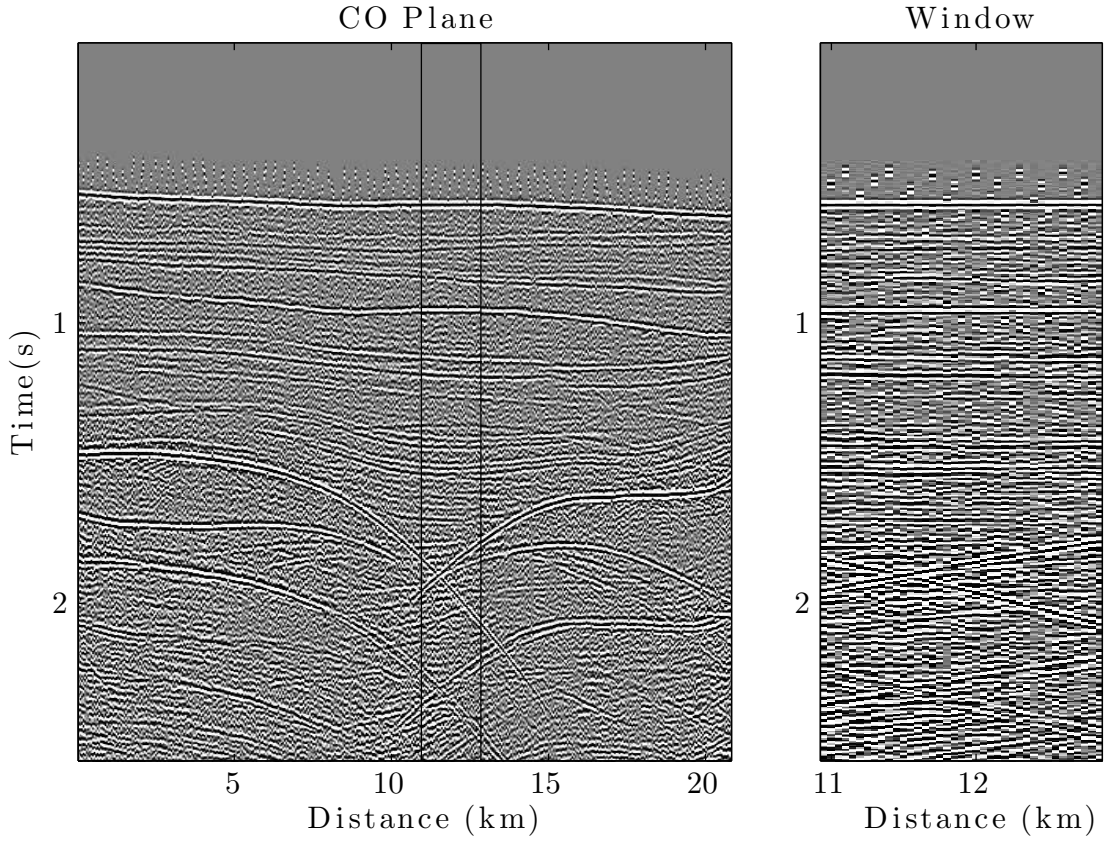

Figure 4.6: Window used in the brief comparison between the Hybrid and f-x Cadzow filter. The black rectangle in the CO plane to the left corresponds to the window to the right.

	Cadzow param.		TFDN param.			Results		
Filter	*type*	*rank*	T_f	nX_{Median}	nY_{Median}	i	RMS	Time (s)
f-x Cadzow	inc	1 to 8				24	40	76
Hybrid - Approach 1	inc	1 to 8	2	5	128	50	41	457
Hybrid - Approach 2	inc	1 to 8	4	3	128	8	62	50

Table 4.1: Parameters and results of the f-x Cadzow and Hybrid filter.

Cadzow only, converges after 24 iterations and the end RMS value is better than the ones for the Hybrid approaches.

From these results we can conclude that the f-x Cadzow is both faster and leads to a better estimate than the hybrid approaches for the selected window from the synthetic dataset Pluto. Therefore, the f-x Cadzow will be run on a semi-synthetic dataset from the Faroese Sea and used in the comparison with the joint de-blending method

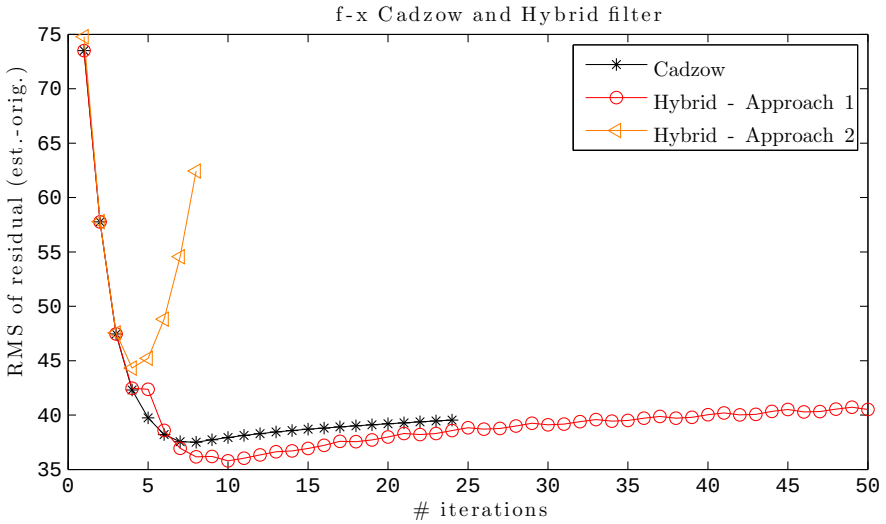

Figure 4.7: RMS of residuals between estimate and unblended data inside inner window for the two approaches for the Hybrid filter and f-x Cadzow.

4.2.4 Algorithmic aspects

This section covers the following related to the de-blending algorithm using f-x Cadzow as a filter:

- Sliding window
- Number of eigenimages
- Thresholding
- Exit strategies

Sliding window

The algorithm uses a overlapping sliding window to adapt for the data locally. The window consists of an inner and outer window. Figure 4.8 shows schematically how the inner and outer window are defined in the algorithm. The inner window is noted with a solid line and the outer with a dashed. The parameters nX and nY define the window length in horizontal and vertical directions respectively. The outer window extends in per % in all directions from the inner window. Data are estimated in the outer window, but only data in the inner window are kept to avoid undesirable edge effects. No averaging scheme is applied for the overlap between the windows. Following paragraphs discuss two aspects: window size and time-shifting of traces.

Window size

To illustrate different window sizes, an example is given. Figure 4.9 shows one common offset section with blending-noise from the *Pluto* dataset. f-x Cadzow has been run one time (i.e., not iteratively) for two different window sizes. In both cases the data has been rank reduced to rank 1. Figure 4.9a shows input (left), and output data (right). The window size is 25 traces in horizontal direction and 10 samples in vertical direction. The input data shows areas with

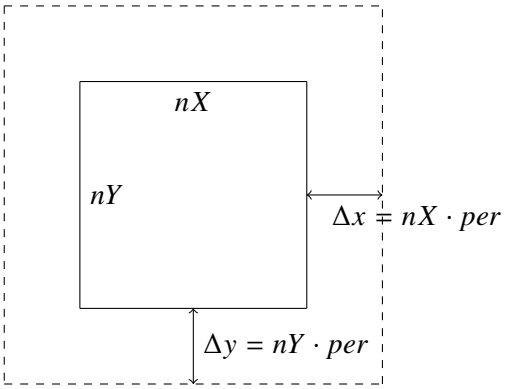

Figure 4.8: Sliding window is defined by three parameters: nX, nY and per.

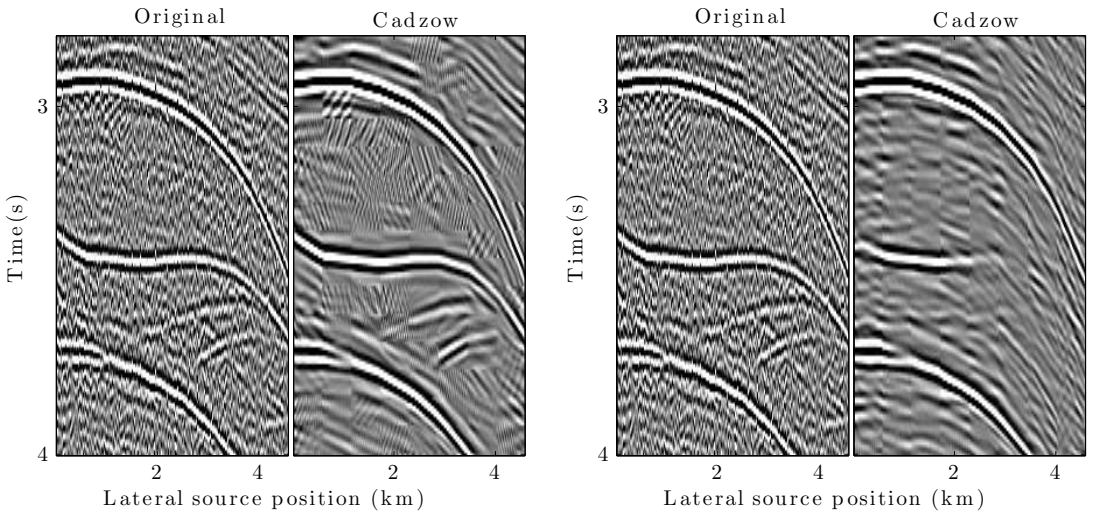

Figure 4.9: Different window sizes applied to blended data. (a) Input (left) and output (right). Window size of 10 samples in vertical direction and 25 traces in horizontal direction. (b) Input (left) and output (right). Window size of 256 samples in vertical direction and 25 traces in horizontal direction.

high dip and different geology. Output data (right) shows that areas with high dip have been preserved. However, in windows where the blending noise is dominant, the f-x Cadzow finds coherency, that looks like linear lines oriented in different directions. A solution to this problem could be to threshold the data. For Figure 4.9b we have the same input data (left), but we use a different window size in the computation (right). The window size is 25 traces in the horizontal direction and 256 samples in the vertical direction. When a window contains multiple dips, more than one eigenimages are needed to ensure full data reconstruction. But, the more eigenimages we take into consideration the more noise will be kept. Therefore, a compromise is needed. The window size should be large enough so the chance of capturing areas with only blending noise is small. But, it should also be small enough to keep the number of necessary eigenimages low. Tests done on the synthetic dataset *Pluto* suggest that a small window size is preferable.

Time-shifting

Time-shifting between time-configurations can be done in two different ways: time-shifting inside the outer window, or time-shifting on the whole time-column. Time-shifting inside the selected window limits the vertical window size. If the vertical outer window size, compared with the inner window, is less than the largest time-shift a poor result is obtained. Therefore, for small inner windows, a large outer window is needed. The overlap of the data is therefore large. A large overlap indicates that more calculations are needed, and therefore the run time is longer. A solution to this problem is to time-shift the whole time-column. This changes the way of estimating each source contribution iteratively. When the time-shift occurs within the window, both source contributions can be calculated inside the window iteratively before we move on to the next window. When time-shifting the whole time-column, the sources are in need of being calculating iteratively time-column by time-column, because information may come from the window below. An example is provided for clarification. Let us consider the estimation of two sources for one time-column. One time-column is picked with an inner and outer column. We only keep data from the inner column. For the first iteration and first source, no time-shifting is applied to the data. Source 1 is estimated by sliding through the time-column vertically, the sliding window consists of a inner and outer window, where only data from the inner window are kept. The estimate is withdrawn and the whole time-column time-shifted, we estimate source 2 for the whole column, time-shift and withdraw and then we estimate source 1. The process is repeated until convergence.

We use the *Pluto* dataset to compare both time-shifting methods. The results depends on two parameters: the largest time-shift, $t_{shift_{max}}$, and the vertical difference, Δy, defined in Figure 4.8. If $\Delta y \geq t_{shift_{max}}$, both time-shifting schemes perform equally. But, if $\Delta y \leq t_{shift_{max}}$, time-shifting the whole time-column gives the best result. Therefore, time-shifting of the full time-column was implemented in the algorithm. This adds flexibility in the algorithm, and we are not limited by the choice of parameters.

To summarize, the window size is defined by the parameters nX, nY and per as shown in Figure 4.8. nX and nY defines the inner window, while per defines the size of the outer window. Time-shifting is done for the whole time-column to add flexibility.

Number of eigenimages

The f-x Cadzow has one parameter, which is the number of eigenimages. This parameter can either be constant or incremental.

Constant

A constant number of eigenimages leads to fast convergence of the data, but a non-flexible algorithm, as the number of eigenimages to take into consideration should preferably be data-dependent.

Incremental
The number of eigenimages is increased during the iterative process. Thus, the method is data-adaptable as we gradually include more and more information in the reconstruction of both the sources. The parameters are defined as r_{min}, r_{max} and r_{inc}:

- r_{min}: Number of eigenimages at first iteration.
- r_{max}: Maximum number of eigenimages taken into consideration.
- r_{inc}: How many eigenimages to increment at each iteration.

For comparison, the constant and incremental approaches have been tested on the synthetic dataset *Pluto*. A constant approach can perform equally well as an incremental approach, but requires more testing of the parameters. An incremental approach is more flexible in nature, but the maximum number, r_{max}, of eigenimages taken into consideration should be carefully decided. If r_{max} is high, the algorithm has difficulty to converge. Due to the adaptive nature, the incremental approach is used in the de-blending.

Threshold

Thresholding is the process of setting to zero values that are under a certain threshold. The estimates can be thresholded after each iteration to ensure that wrongly estimated data are not taken further into next iteration.

The effect of thresholding was tested on a small window of the *Pluto* dataset. Results indicate that thresholding the data does not improve the de-blending.

Exit strategies

Two different exit strategies can be set. One considers the change of the residuals energy, while the other stops the iterative process when maximum number of eigenimages, r_{max}, is reached. If the exit criterion is not met, the method exits the iterative process after reaching a maximum number of iterations, i_{max}, defined by the user.

Energy criterion
When the energy of the residuals does not change from one iteration to the next, the iterative process is terminated. The residuals is defined as:

$$\mathbf{R} = \mathbf{D}_{est} - \mathbf{D}_{obs}, \tag{4.4}$$

where $\mathbf{D}_{est}$, is the sum of time-shifted estimated data for both sources, $\widetilde{\mathbf{D}_1} + T_2(\widetilde{\mathbf{D}_2})$, and $\mathbf{D}_{obs}$ denotes the input blended data. When the energy of the residuals defined in Eq. 4.4 does not change more than a given percentage, C, we exit the iterative process. This parameter is usually set to 1 %.

	Parameters
Window size	nX : Horizontal inner window size, in samples. nY : Vertical inner window size, in samples. per : Window overlap, in percent.
Eigenimage	r_{min} : Number of eigenimages at first iteration. r_{max} : Maximum number of eigenimages taken into consideration. r_{inc} : Number of eigenimages to increment at each iteration.
Exit strategy	C : Residual criterion for the energy change, in percent.

Table 4.2: Parameters used in the de-blending of P data.

Maximum number of eigenimages reached

When the maximum number of eigenimages, r_{max}, is reached, we exit the iterative process. This implementation is rather naive, but can be used when the convergence criteria described above is not met. This implementation shortens the run time, as less iterations are used.

For the testing of the de-blending of the multicomponent data, the energy criterion is used as a measure of the convergence.

Summary

The algorithmic aspects can be summarized as follows:

- The algorithm uses a sliding window.
- The time-shifting between time-configurations occurs for time-columns.
- An incremental approach for the eigenimages is taken.
- Thresholding is not applied.
- The energy criterion is usually used as exit strategy.

Further testing should be done for: optimal window size, thresholding and exit strategy. Table 4.2 summarizes the parameters.

4.3 Joint de-blending of P and MC data

This section presents a novel method for joint deblending of P and MC data. It uses the directivity information provided by the MC data to aid the de-blending of P data, but it also de-blends the MC data. As the signal-to-noise ratio (SNR) of MC data can be extremely low, it is difficult to use the MC data by itself. For this reason, a joint process of de-noising and de-blending is proposed where the objective is double: First, improve the de-blending of P data and secondly, de-blend and de-noise simultaneously the MC data.

The basics covered in section 4.2 also apply for joint de-noising and de-blending of the data. I.e., data is processed in common offset (CO) sections where time-shifting of each trace results in one source contribution being coherent and the other being incoherent. The method requires blended P data and at least one MC dataset, appropriately chosen.

During the course of the development of the method, multiple versions have been tested on a numerically blended wide azimuth (WAZ) dataset described in section 5.3. The final method is described below, while a summary of the other attempts is given in table 4.3 in section 4.3.2. It should be noted that all the tests done on MC data have been restricted to the frequency range $31 - 55$ Hz, due to the low frequencies being extremely noisy.

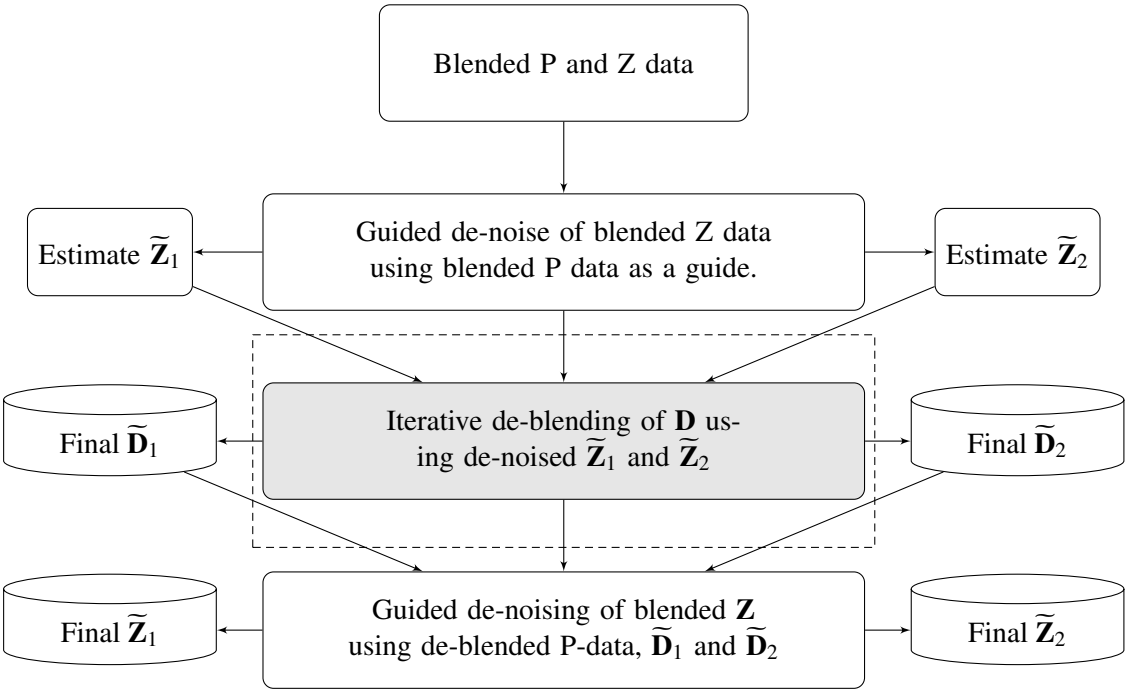

Figure 4.10: Workflow for the joint de-denoising and de-blending the P and MC data.

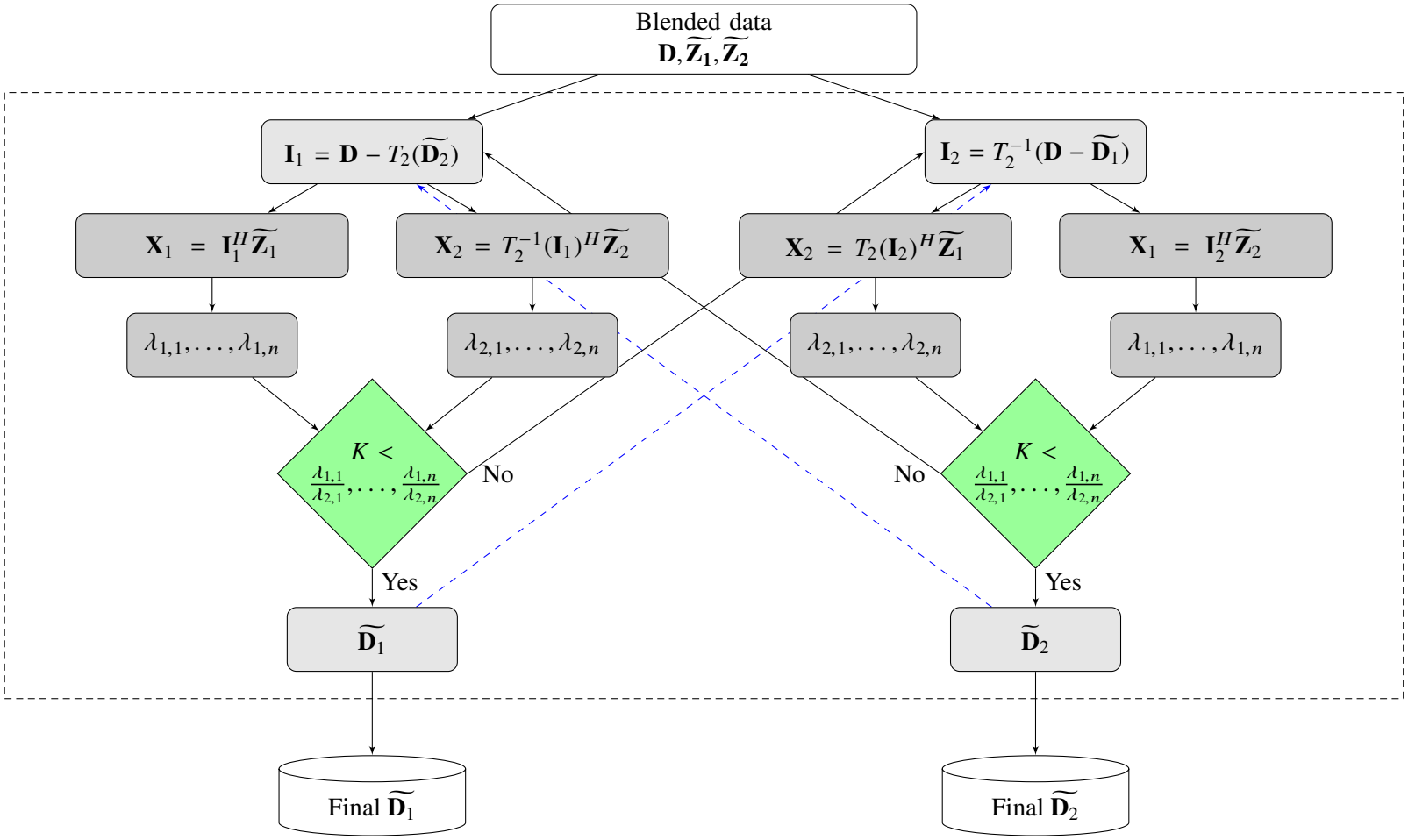

Figure 4.11: Flowchart detailing the iterative de-blending of P data using MC data.

4.3.1 Method

The method, schematically described in Figure 4.10, requires P data and one MC dataset, either Y or Z data, and operates in the CO domain. We describe de-blending where two sources have been blended and the blended Z data is utilized. But, this could be extended to multiple sources and using both Y and Z data. First, an initial estimate of Z data for both sources, $\widetilde{\mathbf{Z}_1}$ and $\widetilde{\mathbf{Z}_2}$, is obtained by applying joint denoising (cf. section 3.3.3), with $\mathbf{D}$ and $T_2^{-1}(\mathbf{D})$ as respective guides. The Z data estimates are then used in the guided de-blending of P data detailed below, yielding the deblended estimates of P data, $\widetilde{\mathbf{D}_1}$ and $\widetilde{\mathbf{D}_2}$. These final estimates are then used as a guide for the joint denoising of each source of MC data, thereby providing de-noised and implicitly de-blended $\widetilde{\mathbf{Z}_1}$ and $\widetilde{\mathbf{Z}_2}$ estimates.

Figure 4.11 shows a flowchart that details the guided de-blending of P data using the vertical Z component. The method includes a step where the correlation between the conservative estimate of P data and the MC data is evaluated. The method can be described as follows:

De-blending of P and Z data:

1. Apply guided de-noising on the blended $\mathbf{Z}$-data using the blended P data as a guide to obtain, $\widetilde{\mathbf{Z}_1}$ and $\widetilde{\mathbf{Z}_2}$.
2. Iterative de-blend the P data using $\widetilde{\mathbf{Z}_1}$ and $\widetilde{\mathbf{Z}_2}$:
   (a) For source 1:
      i. Obtain a conservative estimate: $\mathbf{I}_1 = \mathbf{D} - T_2(\mathbf{D}_2)$.
      ii. Compute $\mathbf{X}_1 = \mathbf{I}_1^H \widetilde{\mathbf{Z}_1}$.
      iii. Find the eigenvalues of $\mathbf{X}_1$ and sort them in descending order.
      iv. Compute $\mathbf{X}_2 = T_2^{-1}(\mathbf{I}_1)^H \widetilde{\mathbf{Z}_2}$.
      v. Find the eigenvalues of $\mathbf{X}_2$ and sort them in descending order.
      vi. Take the ratio of the r largest eigenvalues from $\mathbf{X}_1$ and $\mathbf{X}_2$.
      vii. Decide whether to use the conservative estimate further, based on the ratio threshold, K, or go to time-configuration 2.
      viii. Estimate $\widetilde{\mathbf{D}_1}$ by f-x Cadzow keeping r eigenimages.
   (b) For source 2:
      i. Obtain a conservative estimate: $\mathbf{I}_2 = T_2^{-1}(\mathbf{D} - \mathbf{D}_1)$.
      ii. Compute the cross-correlation $\mathbf{X}_1 = \mathbf{I}_2^H \widetilde{\mathbf{Z}_2}$.
      iii. Find the eigenvalues of $\mathbf{X}_1$ and sort them in descending order.
      iv. Compute $\mathbf{X}_2 = T_2(\mathbf{I}_2)^H \widetilde{\mathbf{Z}_1}$.
      v. Find the eigenvalues of $\mathbf{X}_2$ and sort them in descending order.
      vi. Take the ratio of the r largest eigenvalues from $\mathbf{X}_1$ and $\mathbf{X}_2$.
      vii. Decide whether to use the conservative estimate further, based on the ratio threshold, K, or go to time-configuration 1.
      viii. Estimate $\widetilde{\mathbf{D}_2}$ by f-x Cadzow keeping r eigenimages.
   (c) Update parameters and repeat until convergence.

3. Apply a guided de-noising on the blended **Z**-data using $\mathbf{D}_1$ and $\mathbf{D}_2$ as respective guides to obtain a final de-noised and de-blended version of the Z data, $\mathbf{Z}_1$ and $\mathbf{Z}_2$.

4.3.2 Other Attempts

During the development of the method described in the previous section, three other versions have been tested on a subset of numerically blended wide-azimuth (WAZ). Since the SNR is extremely low for low frequencies of the MC data, we have only tested if we can improve the de-blending of P data by using the middle frequencies of the MC data, i.e., $31 - 55$ Hz. An overview is presented in table 4.3. They were tested on an inner window of 512 samples and 25 traces with an outer window 50 % larger. The convergence criteria was set to 1 % change in the energy of the residuals. Number of iterations before convergence are denoted $iter$, RMS denotes the RMS value for the last iteration of the estimated and original unblended data. The time used by each method is displayed in hours. The number of eigenimages evaluated was incremented by 1 for each iteration and went from 1 to 8.

Version	Description	iter.	RMS	Time(h)
f-x Cadzow	Benchmark: De-blending as described in section 4.2 using f-x Cadzow as a filter in the iterative process.	26	11.05	0.02
Version 1	Compare the estimated acceleration singular values from the guided de-noising method. De-noising of the MC data occurs 4 times per iteration. Abandoned due to inconsistency in estimated singular values.	13	10.5	1.02
Version 2	Compare I/O in frequency domain. De-noising of the MC data occurs 4 times per iteration. Abandoned as it did not improve the results.	28	11.5	1.38
Version 3	Compare I/O in time domain. De-noising of the MC data occurs 4 times per iteration. Further improved due to being computational expensive.	11	9.43	0.73
Version 3.1 (Final)	Compare I/O in time domain. De-noising of MC data occurs only two times, before and after the iterative process.	9	8.38	0.06

Table 4.3: Other attempts tested for joint de-blending of P and MC data.

4.3.3 Algorithmic aspects

Noisy sections

One main issue with the method is extremely noisy MC data that makes it not reliable. To solve this problem the method skips the evaluation using MC data if the first test for the first iterations fails, i.e., if the ratio set for the first iteration does not pass the threshold, K. The de-blending of the P data is then the same as in section 4.2.

High performance computing

The high performance computing (HPC) cluster Abel (University of Oslo) was used, due to the method being computational expensive. An utilization of 120 processors was used, one per CO section. Leading to drastically reducing the run-time. Faster testing leads to better development as more things could be implemented and tested faster. For the final version the use of HPC would not be required, but it was an important factor in the development of the algorithm.

Parameters

The new parameters used in the method are the ratio threshold, K, and the number of eigenimages to use in the de-noising of the MC data, N_{den}.

Ratio threshold, K The ratio threshold should be carefully selected. If the threshold is too small, all the eigenvalues will pass the criterion and the method is equal to just using f-x Cadzow in the de-blending process. If the threshold is set too large, no estimate is taken further for both time-configurations and therefore, the data is not de-blended. Tests suggest that the threshold, K, should be set to 1, i.e. the ratio $R = \frac{\lambda_1}{\lambda 2} > 1$. The maximum number of eigenvalues to evaluate was set to 6.

Eigenimages in de-noising, N_{den} is the number of eigenimages to be used in the de-noising of the MC data. If the data are very noisy, a small value is chosen, e.g. 4. If the data are contaminated by little noise, a larger value should be chosen. Tests suggest that a value of 5 eigenimages should be used for middle frequencies.

5 Field data examples

5.1 Introduction

In this chapter, we test on field data the deblending techniques described in chapter 4. It consists of two parts, section 5.2 showing results for de-blending of P data only and section 5.3 showing results for joint de-blending of P and MC data

In section 5.2 two streamers from a 3D survey have been numerically blended to form a 2D blended dataset. The data have been blended in two different ways:

- Scenario 1: Primary and source vessel on the same side of the streamer, where the source vessel is 200 m to the right of the primary vessel.
- Scenario 2: Source vessel is behind the tailbuoys of the survey.

The data have then been de-blended by only using P data. The f-x Cadzow has been run iteratively as described in section 4.2 and we have obtained de-blended estimates of the sources. These estimates are then processed further by stacking and post-stack finite difference migration. Only the migrations are shown due to similar results with the stacked data. As we have numerically blended the data, unblended data are available, and the error have been quantified by normalized root mean square (NRMS) describe below.

In section 5.3 a wide azimuth survey have been numerically blended. A joint de-blending of P and MC data have then been performed, as described in section 4.3. Both Y and Z data have been used separately for guiding the de-blending of P data. The error has been quantified with NRMS as we have unblended data available.

The NRMS that quantifies the error between estimated data and unblended data is defined as (Kragh and Christie, 2002):

$$NRMS = \frac{RMS(\mathbf{a} - \mathbf{b})}{\frac{1}{2}(RMS(\mathbf{a}) + RMS(\mathbf{b}))} \tag{5.1}$$

where the RMS is defined as

$$RMS(\mathbf{x}) = \sqrt{\frac{\sum_i^N x_i^2}{N}} \tag{5.2}$$

and **x** is a vector containing N samples. The NRMS is in the range from 0 to 2. If the datasets are equal, the NRMS is 0. If the datasets are not equal at all, the NRMS is 2. If the two datasets contains random noise, the NRMS is 1.41 or $\sqrt{2}$ (Kragh and Christie, 2002). The NRMS has been calculated in two ways in this chapter: locally and globally. The local method calculates the NRMS for a sliding window, of 5 samples and 1 trace. This gives a visual presentation of the performance of the de-blending. Globally, the NRMS is calculated for a large window, and therefore a value is obtained. The window selected is the same for all the datasets computed and can therefore be used as an quantitative measure of how well the de-blending performed.

5.2 Faroese 2D field data: De-blending of P data

5.2.1 General information

The field data presented is acquired offshore the Faroe islands. The acquisition parameters are given in table 5.1. A subset of the original data was extracted, the data were resampled to 4 ms and number of channels were reduced from 638 to 240. The swell noise was estimated and removed before numerical blending of the data.

5.2.2 Blended acquisition design

The original data was acquired with 5 streamers with a spacing of 100 m (Figure 5.1a). The data from streamer 1 and 3 have been blended together in two different ways:

- Scenario 1: Primary and source vessel on the same side of the streamer, where the source vessel is 200 m to the right of the primary vessel.
- Scenario 2: Source vessel is behind the tailbuoys of the survey.

Scenario 1 is depicted in Figure 5.1b, where data from streamer 1 has been time-shifted and added onto the data from streamer 3. For scenario 2, the data from streamer 1 has been flipped and time-shifted before it has been added onto the data from streamer 3. The time-shifts were quasi-random and between -250 and 250 ms.

Source interval	50 m
Receiver interval	12.5 m
Sample rate	2 ms
Number of channels	638
Number of shots	416

Table 5.1: Acquisition geometry for the Faroese dataset.

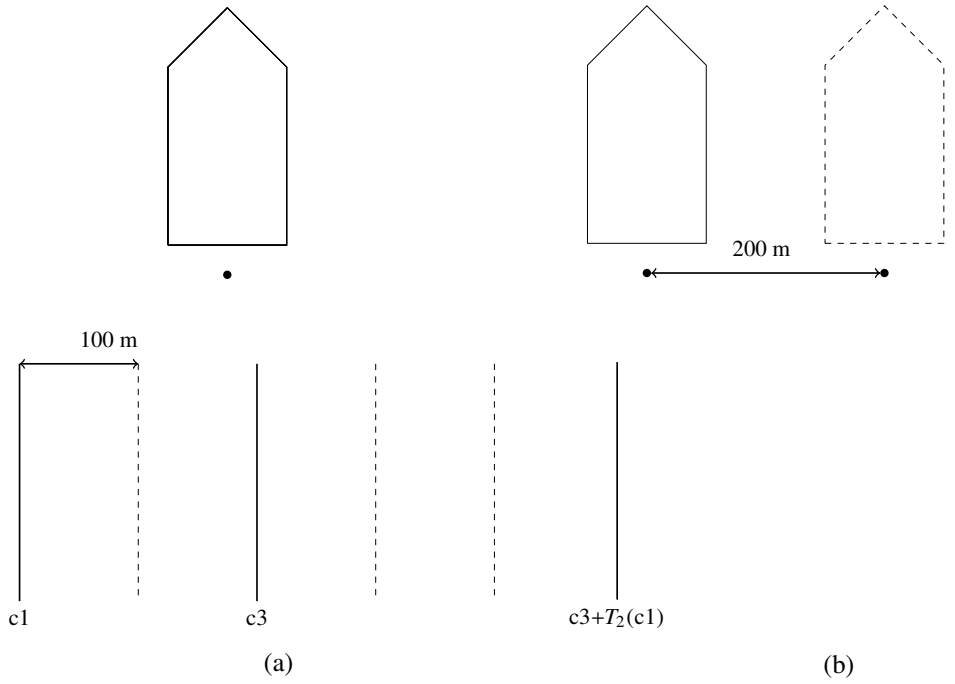

Figure 5.1: Numerically blended Faroese acquisition design with 1 streamers and two sources.

5.2.3 De-blending strategy

For scenario 1 the de-blending is done with a f-x Cadzow iterative filter with a window size of 25 shots and 300 samples in the CO domain with the windows overlapping by 25 percent. Rank stars at 1 and increased by 1 every iteration up to rank 7. The iteration ends when we reach the maximum rank of 7, resulting in 7 iterations per window. Running through the whole dataset takes about 7 hours on 12 CPUs.

For scenario 2 the de-blending is done with a f-x Cadzow iterative filter with a window size of 25 shots and 256 samples in the CO domain with the windows overlapping by 25 percent. Rank starts at 1 and increases by 1 every iteration up to rank 8. The iteration ends when the residual energy stops changing by more than 1 %, resulting in an average of 15 iterations per window. Running through the whole dataset takes about 8 hours on 12 CPUs. The parameters are summarized for scenario 1 and 2 in table 5.2.

	Window size			Eigenimages			
Dataset	nX	nY	per	r_{min}	r_{max}	r_{inc}	C
Scenario 1	25	300	0.25	1	7	1	No
Scenario 2	25	256	0.25	1	8	1	0.01

Table 5.2: Parameters used in de-blending of the different scenarios.

5.2.4 Results

Scenario 1

Figure 5.2 shows one blended shot de-blended into its respective sources, as well as the difference plots between the de-blended data and the original unblended data. Source 1 shows some attenuation of coherent energy, marked by dashed ellipses. For source 2, the de-blending has estimated some coherent energy in the top of the data that should not be present, marked by arrows. The data was further processed to compare the data as stacks and post-stack migrations. For this purpose, the unblended data, blended data in time-configuration 1 and de-blended data for source 1 were stacked and post-stack time migrated by 2D finite difference. Due to similar results to the migrations, the stacks are not shown. For completeness migrations of time-configuration 2 and de-blended data for source 2 are in appendix B. The migrations are shown in Figure 5.3, while difference and NRMS plots are shown in Figure 5.4. The migrated blended data (Figure 5.3b) shows interference noise most prominently around strong reflectors. The interference noise is also clearly seen in the difference plot (Figure 5.4a) and in the NRMS plot (Figure 5.4c) where the reflectors under the sea-bottom are masked by the interference noise. These reflectors are revealed in Figure 5.3c, which shows the de-blended data. This is also visible in the NRMS plot (Figure 5.4d) where the straight reflectors below the sea-bottom have a NRMS value around 0. Furthermore the difference plot (Figure 5.4b) reveals that also diffractions have been suppressed due to the de-blending. The NRMS values are placed in table 5.3. They are calculated for a specific window going from the sea-bottom to 0.5 seconds before the end of the data of 8 seconds. From these numbers we observe that migration reduces the blending noise.

We can summarize the observations as follows:

- We have successfully de-blended the blended data to into its respective sources.
- The de-blended shots show attenuation of some coherent energy marked with ellipses in the shot gathers. The method has also introduces unwanted energy pointed out with arrows.
- Migration of blended data shows interference pattern around strong reflectors, marked with ellipses. This blending noise has been successfully attenuated in the de-blending.
- Difference and NRMS plots of de-blended data show that straight reflectors have been de-blended well, while reflectors with high curvature such as diffractions have partly been attenuated.

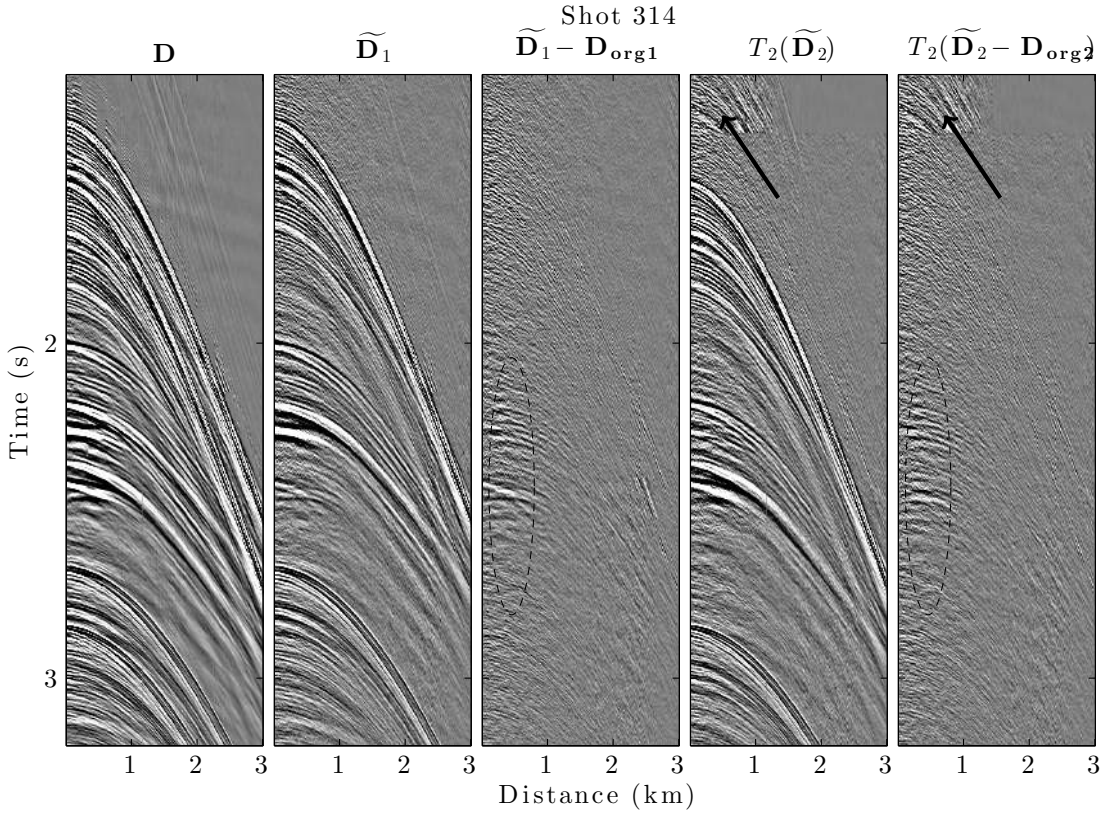

Figure 5.2: Scenario 1: De-blending of one shot from the Faroese dataset.

	Dataset	NRMS Stack	NRMS Migration
Faroese	Scenario 1: Blended T_1	0.59	0.57
	Scenario 1: Blended T_2	0.62	0.58
	Scenario 1: De-blended $\widetilde{\mathbf{D}}_1$	0.41	0.40
	Scenario 1: De-blended $\widetilde{\mathbf{D}}_2$	0.45	0.44

Table 5.3: NRMS results for scenario 1 of the Faroese data.

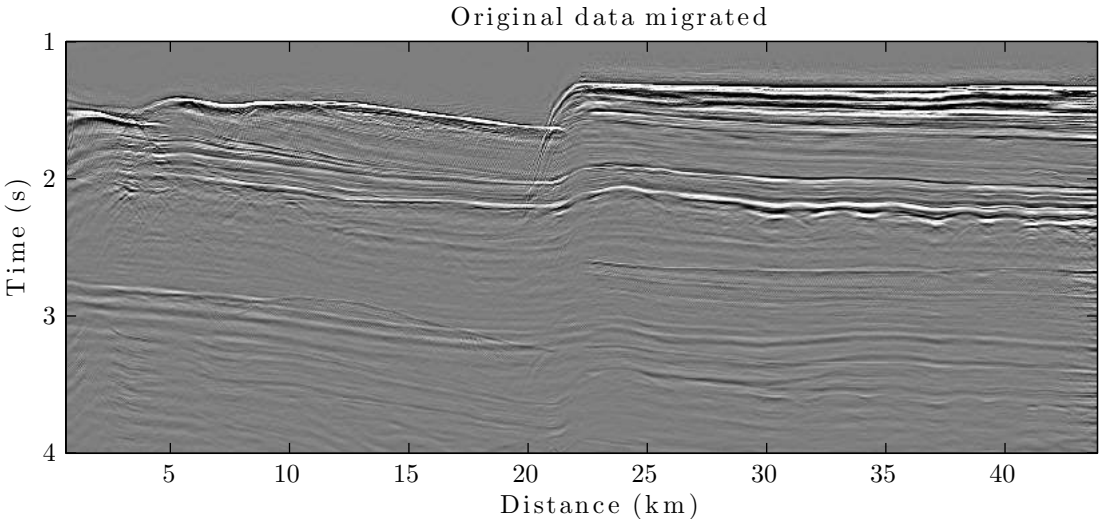

(a)

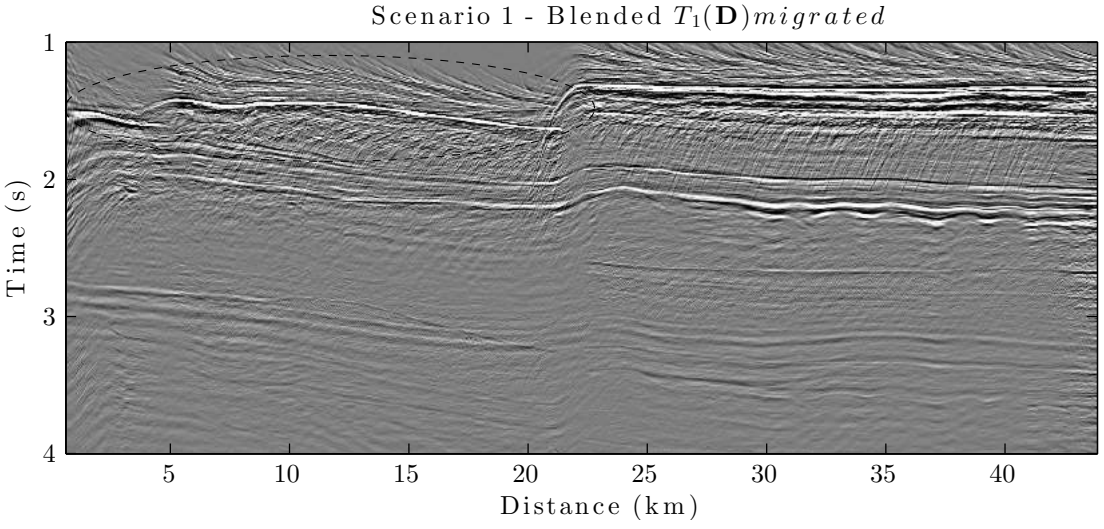

(b)

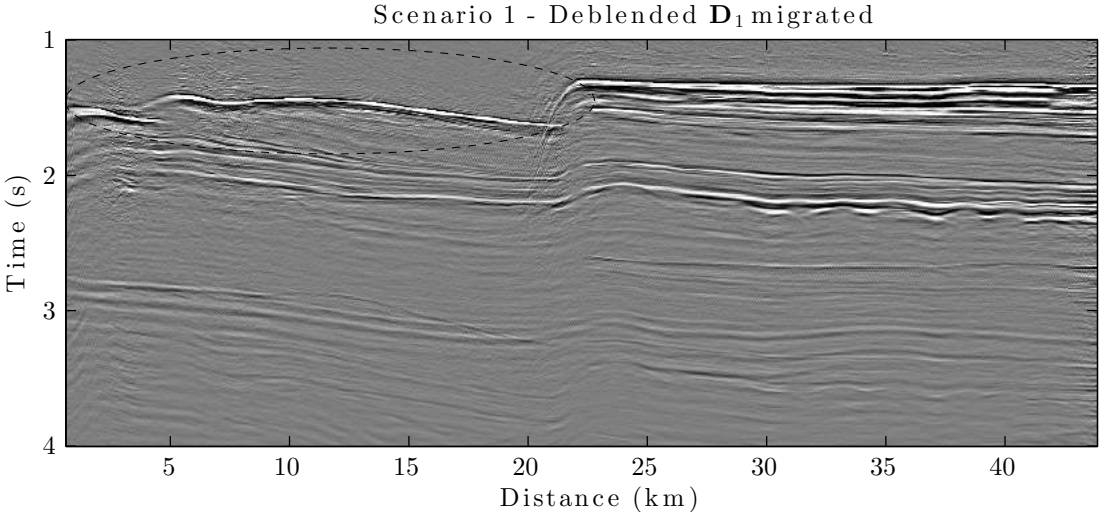

(c)

Figure 5.3: (a) Original data migrated. (b) Blended data migrated: $T_1(\mathbf{D})$. (c) Deblended data migrated: $\widetilde{\mathbf{D}}_1$.

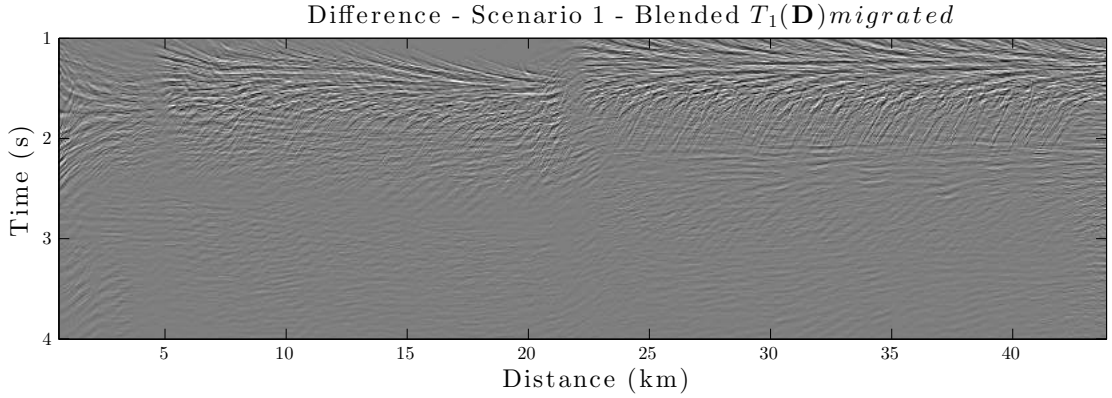

(a)

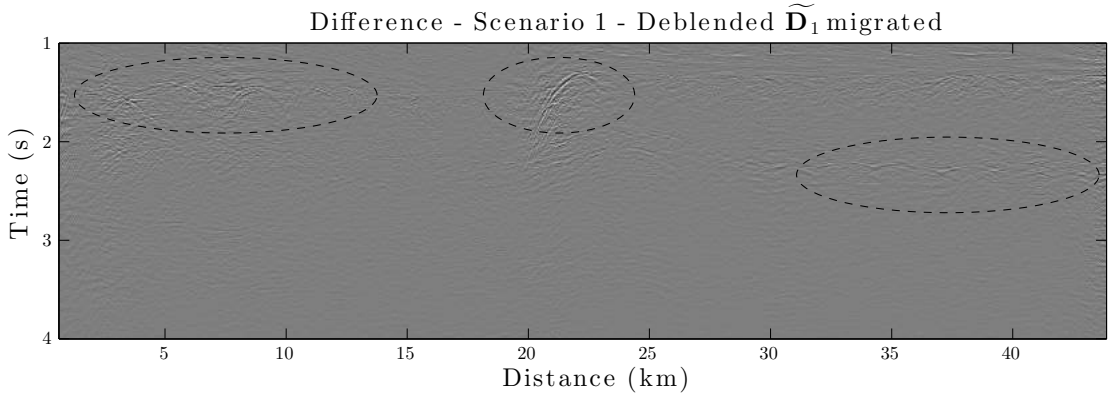

(b)

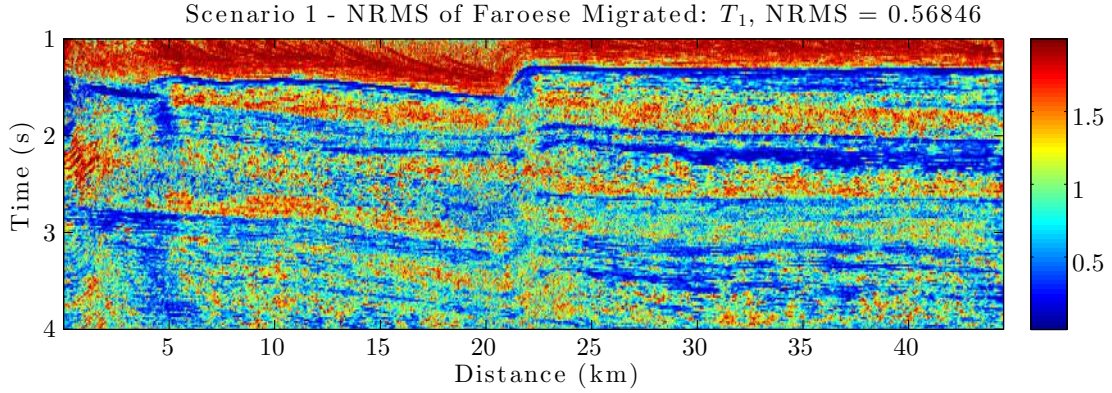

(c)

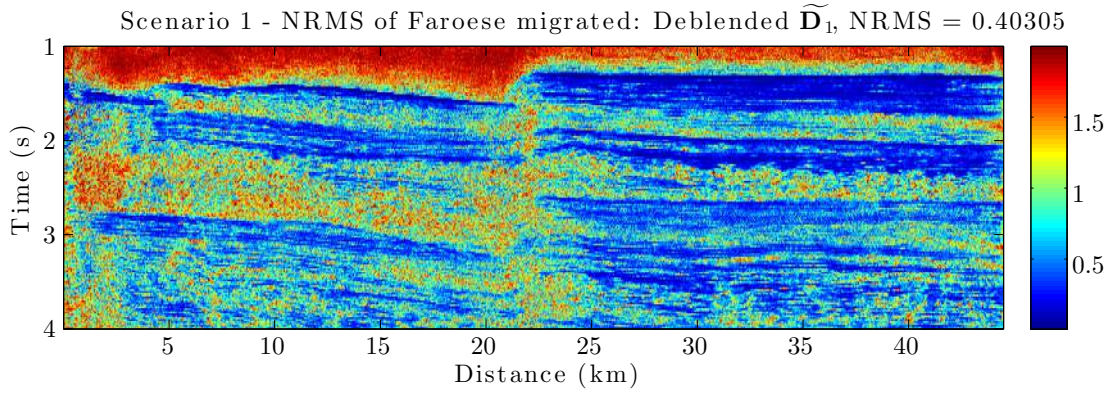

(d)

Figure 5.4: Scenario 1, migrated data. (a) Blending noise. (b) Estimation error. NRMS plots of: (c) Blending noise. (d) Estimation error.

Scenario 2

For scenario 2, the de-blended results are similar to scenario 1, but the interference noise present in the blended data has a different character. Figure 5.5 shows one blended shot de-blended into its respective sources, as well as the difference plots between the de-blended data and the original unblended data. The difference plots for sources 1 and 2 show attenuation of coherent energy. The data was further processed to compare the data as stacks and post-stack migrations. For this purpose, the unblended data, blended data in time-configuration 1 and de-blended data for source 1 were stacked and post-stack time migrated by 2D finite difference. The stacks are not shown due to similar results obtained for the migrations. For completeness migrations of time-configuration 2 and de-blended data for source 2 are in appendix B. Migrations are shown in Figure 5.6, while difference and NRMS plots are shown in Figure 5.7. The migrated blended data (Figure 5.6b) shows interference noise seen as almost vertical lines with an inclination to the right. The interference noise is also clearly seen in the difference plot (Figure 5.7a) and in the NRMS plot (Figure 5.7c). The interference noise, as well as diffractions have been attenuated by the de-blending seen in Figure 5.6c, which shows the output of the migrated de-blended data. This is also shown by the difference and NRMS plots between the original data in Figures 5.7d and 5.7b. The NRMS value was calculated for a specific window going from the sea-bottom to 0.5 seconds before the end of the data of 8 seconds are placed in table 5.4. As for scenario 1, migration of the data reduce the blending noise.

We can summarize the observations as follows:

- We have de-blended the two sources well with negligible amount of crosstalk. However, de-blended shots show some attenuation of coherent energy. The method also introduces some unwanted random energy in areas where hardly any data are present.
- Migrations of blended data shows interference pattern as vertical lines inclined to the right.
- Difference and NRMS plots of de-blended data show that straight reflectors have been de-blended well, while reflectors with high curvature such as diffractions have been attenuated.

		NRMS	
	Dataset	Stack	Migration
Faroese	Scenario 2: Blended T_1	0.59	0.53
	Scenario 2: Blended T_2	0.65	0.58
	Scenario 2: De-blended $\widetilde{\mathbf{D}_1}$	0.40	0.39
	Scenario 2: De-blended $\widetilde{\mathbf{D}_2}$	0.44	0.42

Table 5.4: NRMS results for scenario 2.

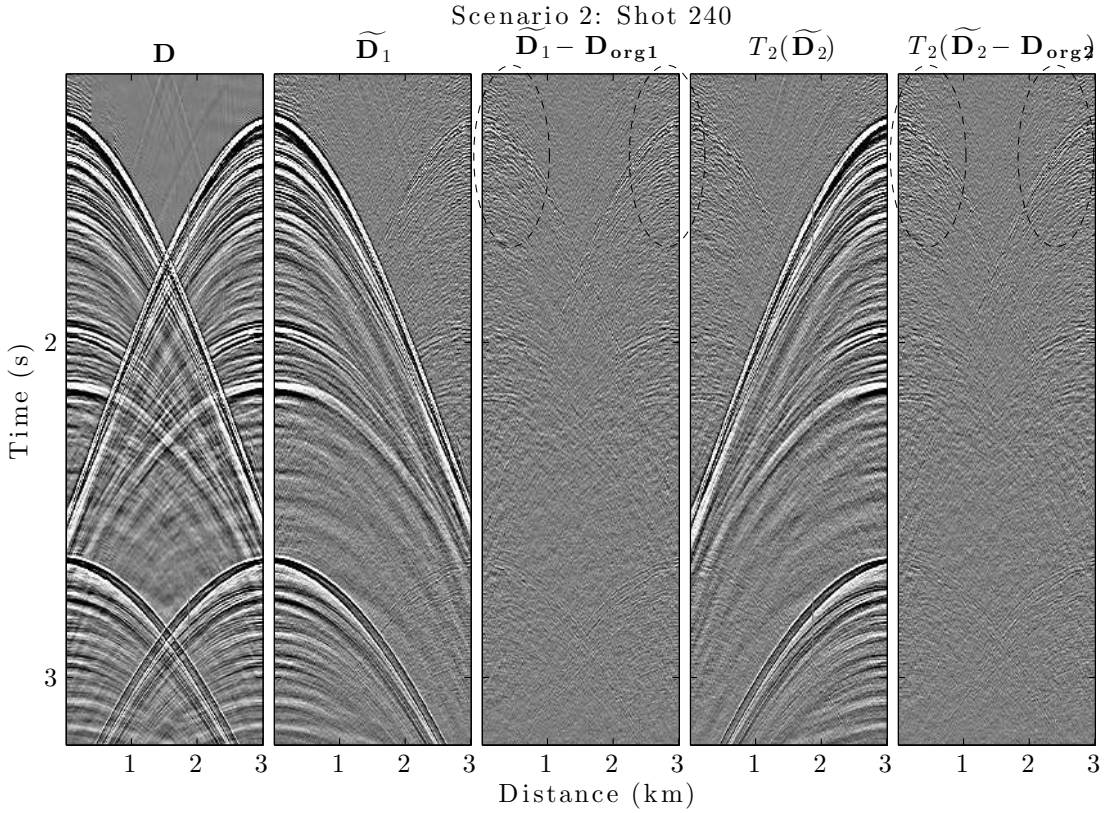

Figure 5.5: Scenario 2: De-blending of one shot into its respective sources.

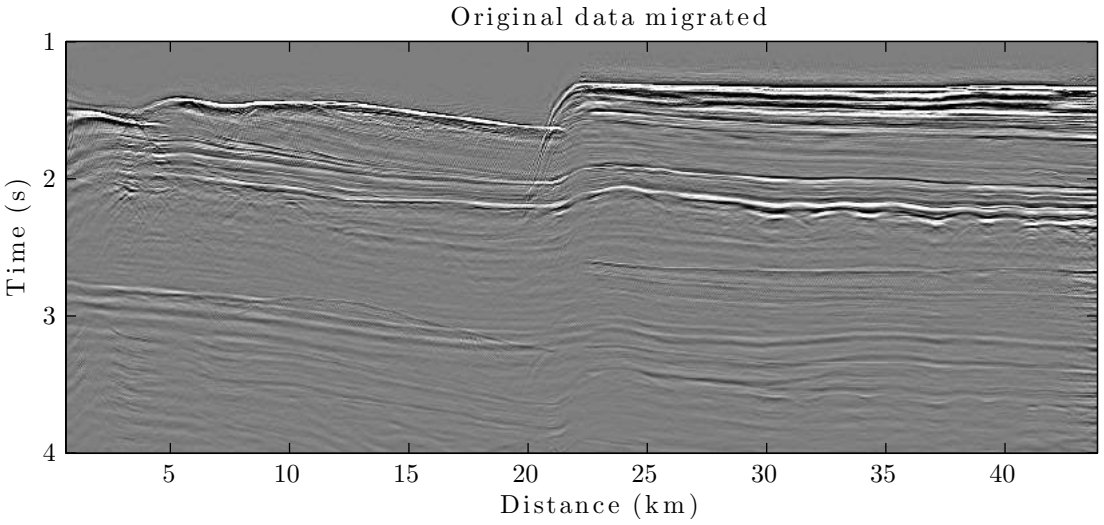

(a)

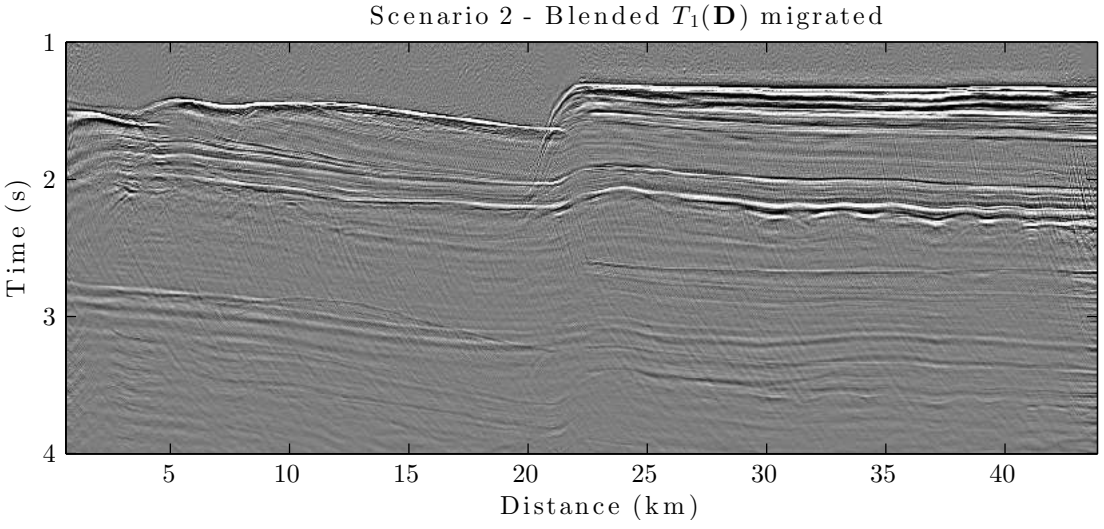

(b)

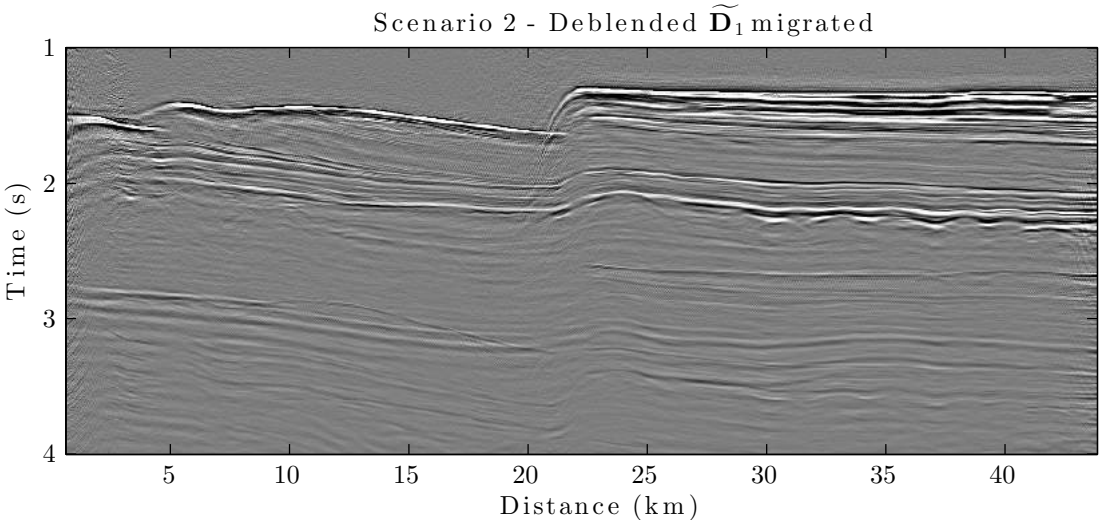

(c)

Figure 5.6: Scenario 2 - Migrated: (a) Original data. (b) Blended data: $T_1(\mathbf{D})$. (c) De-blended data: $\widetilde{\mathbf{D}}_1$.

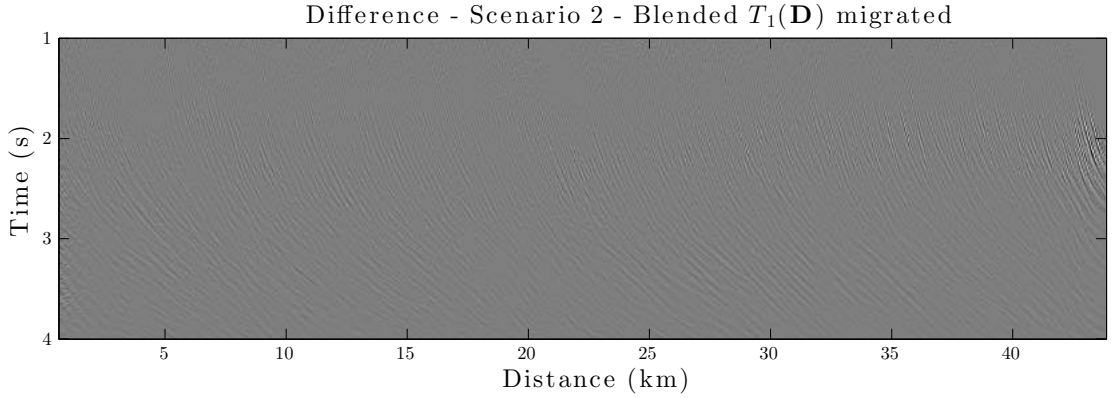

(a)

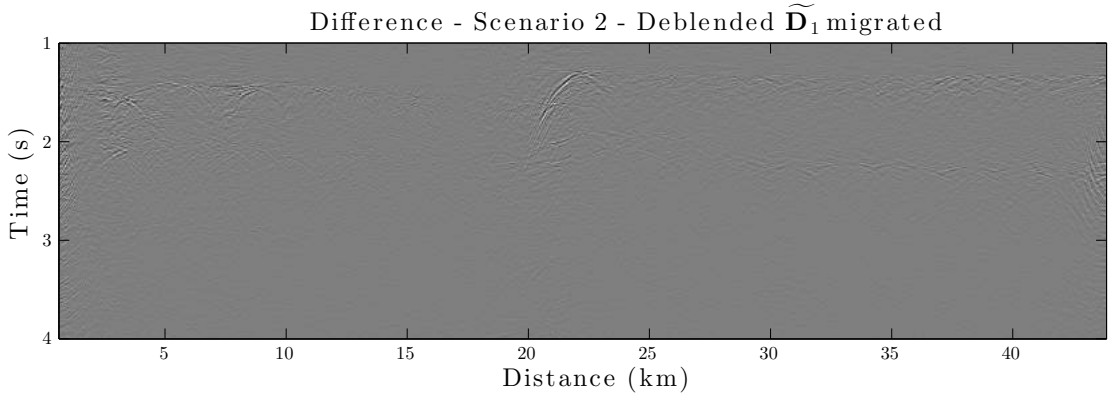

(b)

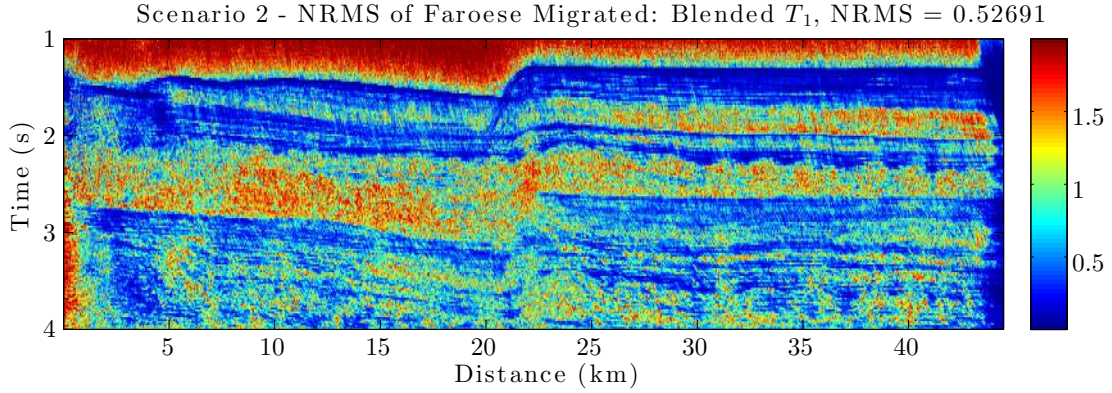

(c)

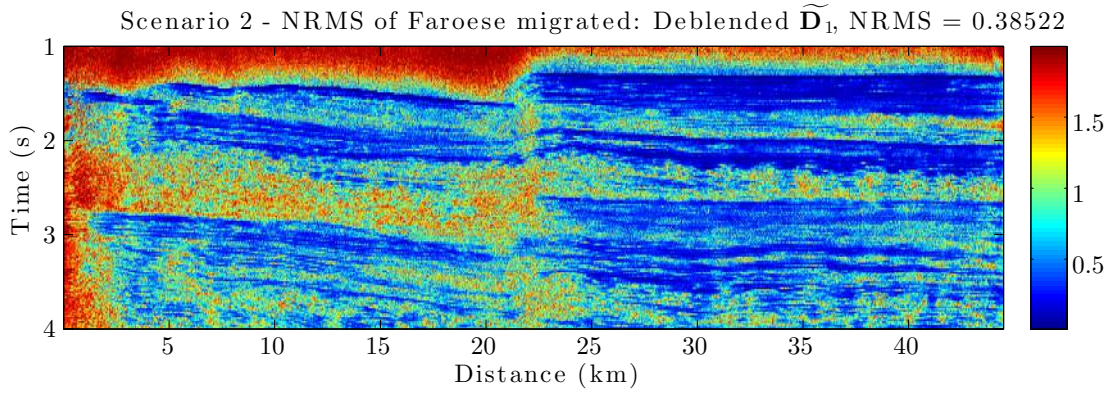

(d)

Figure 5.7: Scenario 2 - Migrated: (a) Blending noise. (b) Estimation error. NRMS plots: (c) Between unblended and blended data. (d) Between unblended and deblended.

5.3 Wide azimuth 2D field data: Joint de-blending of P and MC data

This section covers the results from joint de-blending using P and MC data, and consists of three parts. The first part, section 5.3.1, covers the blending strategy that has been applied for the numerical blended data. The second part, section 5.3.2, covers the de-blending strategy and parameters used in the de-blending. The third part, section 5.3.3, presents the results.

5.3.1 General information and blending strategy

This section discusses the numerical blending of the MC datasets. The datasets blended together are from the same wide azimuth (WAZ) survey in the Faroese Sea. For this test survey, one vessel is towing streamers, while a source vessel is steered with an angle in respect to the source vessel while shooting. The 61 last shots from the survey, noted *WAZ1*, have been blended together with the 61 middle shots, noted *WAZ2*. Data from dataset *WAZ1* have gone through de-noising. Joint directional de-noising (cf. section 3.3.3) has been applied to the Y and Z data from *WAZ1* dataset before blending so that we do not cumulate the MC noise. The P data from dataset *WAZ1* has also gone through a $\tau - p$ filter, where only a forward and a backward $\tau - p$ transformation has been applied to remove swell noise.

As testing is only done on 61 shots from the wide-azimuth survey, this analysis will only manage to conclude if the shot data could be improved; a final migrated image of the surface will not be provided due to lack of data. Furthermore the data contains only 120 channels as the streamers were only equipped with 120 channels of MC sensors. The blended *WAZ2* is treated as the coherent source, while data from *WAZ1* is time-shifted for every shot the same way as for the Faroese datasets.

Figure 5.8, 5.9 and 5.10 show shot gathers for blended and unblended data *WAZ1* and *WAZ2* as well as their average amplitude spectrum for P, Z and Y data respectively. For the P data, the amplitude spectrum and the shots have similar character. The Z- and Y data for *WAZ1* and *WAZ2* are very different in terms of noise contamination, where the signal in the WAZ2 is difficult to identify due to huge contamination of noise, whereas *WAZ1* is rather clean. The de-noised Y data have a similar character as the noisy Y, while the de-noised Z data seems averaged out. The character of the amplitude spectrum is therefore also hard to compare as the vibration noise is many magnitudes larger than the recorded signal.

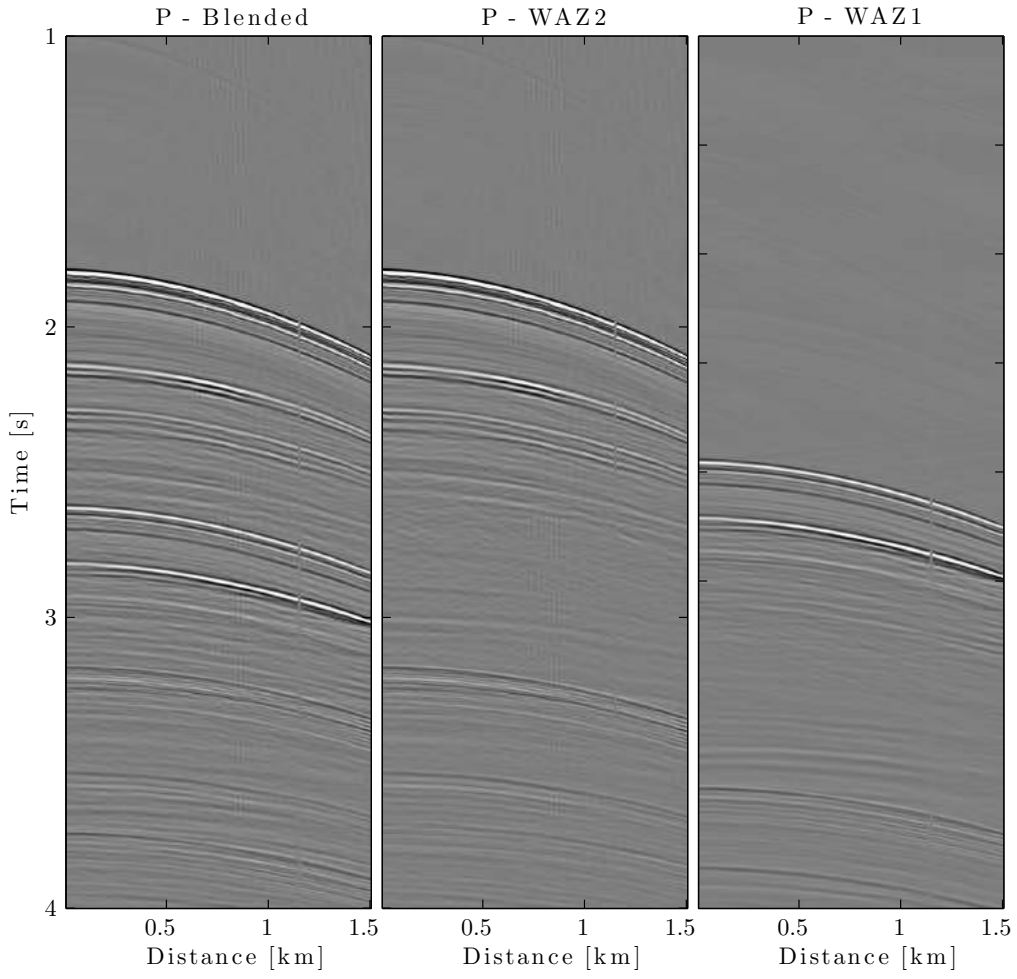

(a)

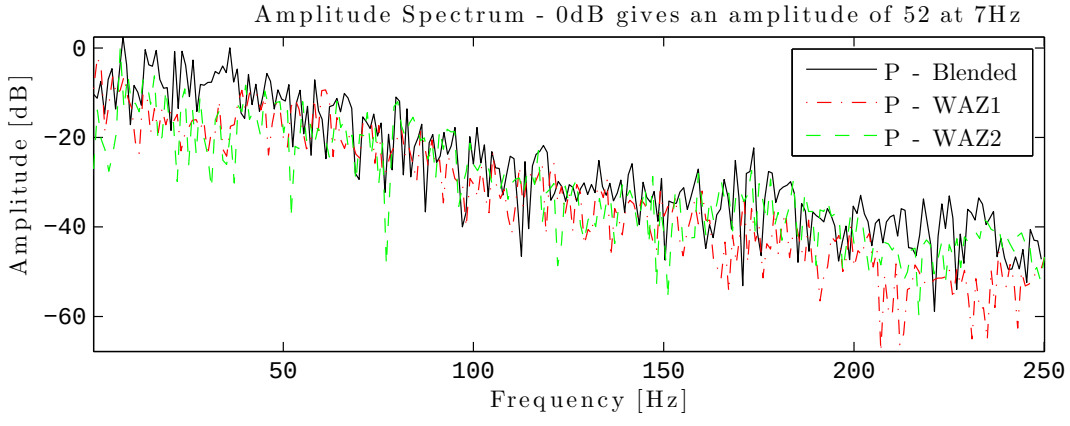

(b)

Figure 5.8: Analysis of P data blended together.

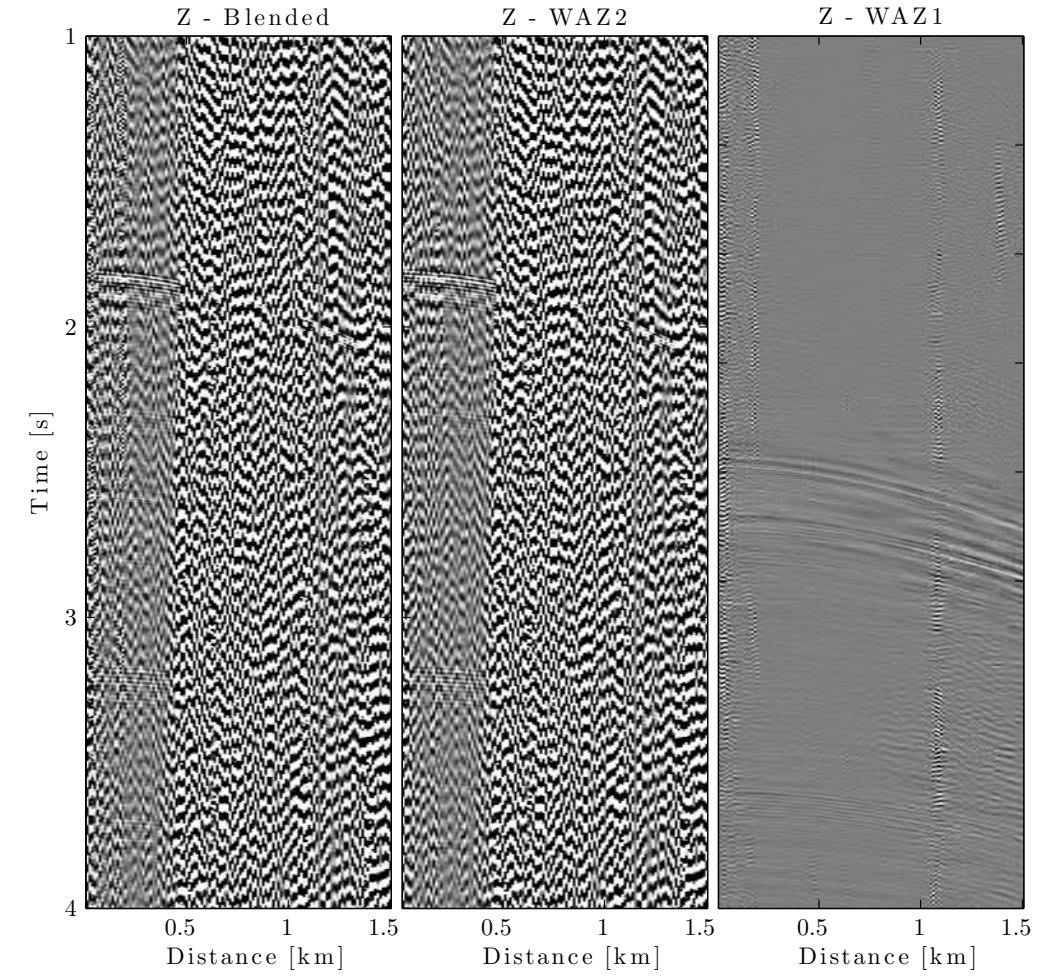

(a)

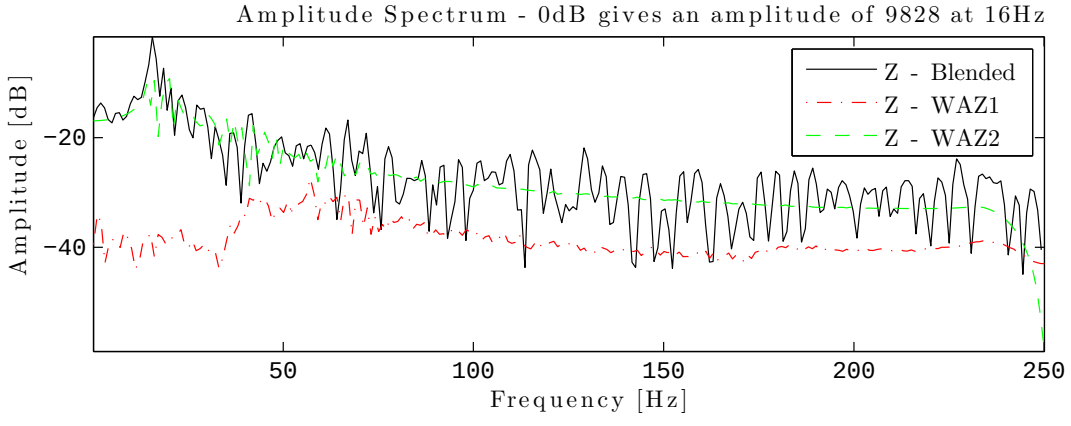

(b)

Figure 5.9: Analysis of Z data blended together.

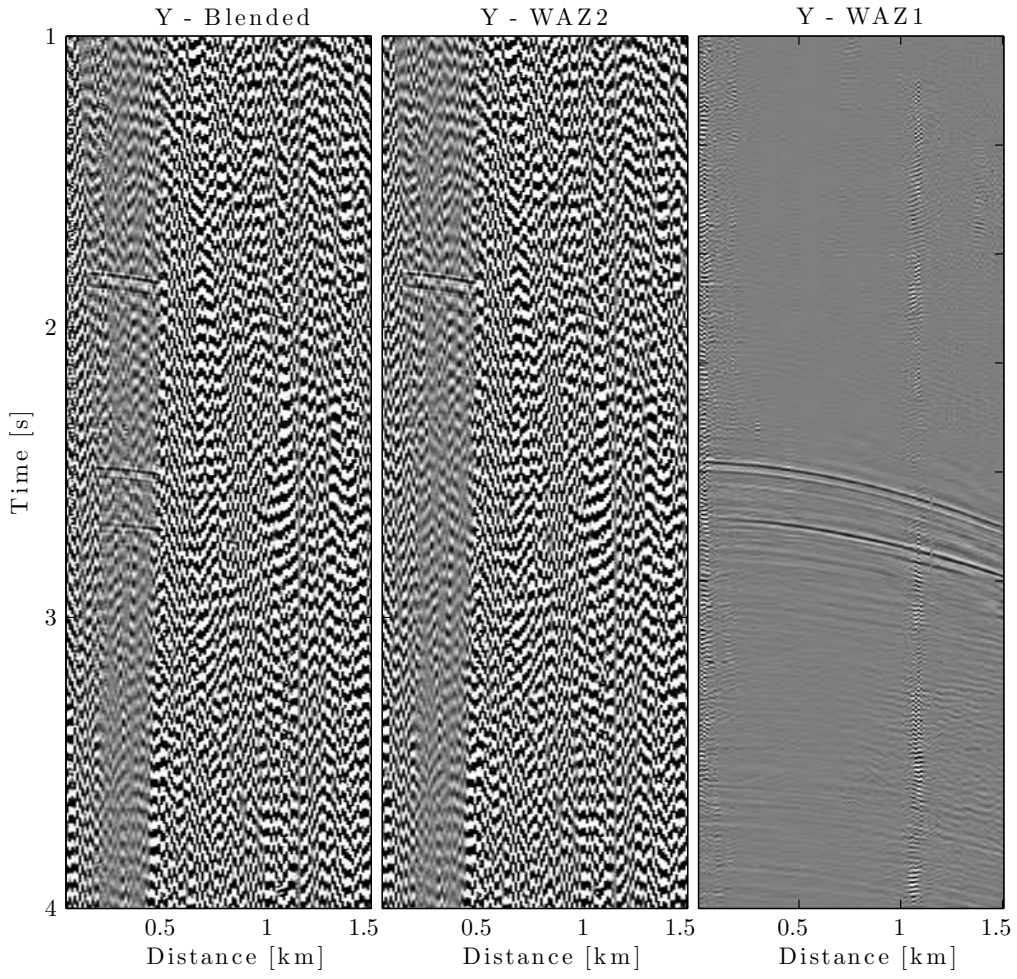

(a)

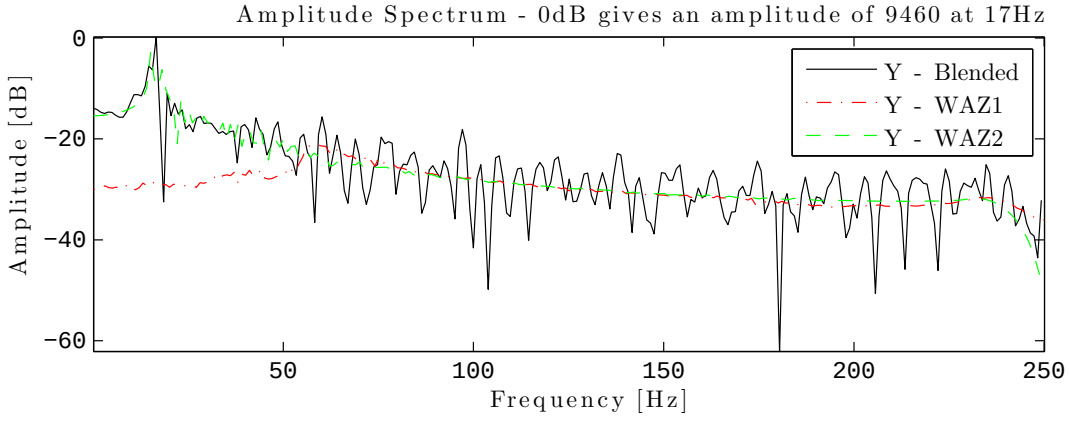

(b)

Figure 5.10: Analysis of Y data blended together.

	Window size			Eigenimages					
Dataset	nX	nY	per	r_{min}	r_{max}	r_{inc}	C	K	N_{den}
f-x Cadzow	21	256	0.25	1	8	1	0.01	-	-
Joint de-blend with Y data	21	256	0.25	1	8	1	0.01	1	5
Joint de-blend with Z data	21	256	0.25	1	8	1	0.01	1	5

Table 5.5: Parameters used in de-blending P data with f-x Cadzow and joint de-blending.

5.3.2 De-blending strategy

The de-blending of the P data is achieved with both the f-x Cadzow and joint de-blending and de-noising P and MC data. The results from de-blending using f-x Cadzow is set as a benchmark and is compared against the joint de-blending method.

For the f-x Cadzow method a window size of 256 samples and 21 traces was chosen with an window overlap of 25 %. Number of eigenimages to keep was incrementing by 1 from 1 to 8. The iterative process ended when the residual energy change was less than 1 %. The de-blending of the 61 shots took 1.1 hours with the f-x Cadzow running on the computer cluster abel using 12 processors.

As the joint de-blending method only uses one MC dataset at the time, we run the joint deblending for Y and Z data separately. As this survey is a wide-azimuth survey, both the Y and Z data have reasonable signal-to-noise ratio. In addition, we only test the middle frequencies $31 - 55$ Hz as the MC data are considered to be too noisy for the low frequencies. For both de-blending with the help of the Y data and Z data, a window size of 256 samples and 21 traces with an window overlap of 25 % is used. The threshold ratio, K is set to 1, and the number of eigenimages taken into the estimation increments by 1 at each iteration from 1 to 8. The iterative process ended when the residual energy changes was less than 1 %. The number of eigenimages used in the de-noising of MC data, N_{den}, is set to 5.

The parameters used for both methods are summarized in table 5.5.

5.3.3 Results

The following results display de-blended shots and common offset (CO) sections. For an estimation of the accuracy, the NRMS between estimated and original will be calculated for all the shots and averaged.

De-blending of P data

For comparison, the results for joint de-blending and the P-only de-blending are presented presented in table 5.6. The NRMS value is calculated for the full shot gather window and for all the shot-gathers and then averaged. The iteration number is the average iteration for all the windows and common offset (CO) sections. The time value is the average computation time to process one CO section, where all the tests have been run on the same hardware. As each processor is assigned one common offset section, this value can be compared. A bandpass filter has been applied to all the datasets prior to de-blending.

P-only de-blending

Figure 5.11 shows the results of de-blending the WAZ dataset with P-only. Figure 5.11a shows one blended shot de-blended into its respective sources: The first column is the blended shot gather, while the second and fourth column show de-blended data from each source. The difference between the estimated and unblended data is shown in the third and fifth column. The difference plots show that random energy has been introduced above the first arrival and some coherent energy has not been estimated (dashed boxes). Figure 5.12a shows one common offset section in both time-configurations, $\mathbf{D}$ and $T_2^{-1}(\mathbf{D})$, de-blended into its respective source contributions.

Joint de-blending

Joint de-blending is run with the use of Z and Y data separately. For the WAZ dataset, the SNR is higher for the Y data than the Z data, due to this being a very wide-azimuth survey. For this reason, only the results from joint de-blending using Y data are presented here. Figure 5.11b shows one blended shot of P data de-blended into its respective sources: The first column is the blended shot gather, while the second and fourth column show de-blended data from each source. The difference between the estimated and unblended data is shown in the third and fifth column. The difference plots show that some random energy has been introduced above the first arrival and some coherent energy has not been estimated (dashed line). Figure 5.12b shows one common offset section in both time-configurations, $\mathbf{D}$ and $T_2^{-1}(\mathbf{D})$, de-blended into its respective source contributions.

Visually, the joint de-blending with Y data is marginally better than P-only de-blending. Areas in Figures 5.11b and 5.12b that show improvement are marked with dashed ellipses.

Method	NRMS	iter.	Time (h)
P data only	0.518	21.0	0.10
Jointly with Z data	0.491	18.4	0.53
Jointly with Y data	0.494	20.3	0.47

Table 5.6: Comparison of the NRMS error, number of iterations and run-time for different de-blending techniques. The NRMS (calculated for all shots), the number of iterations and the run-time have been averaged.

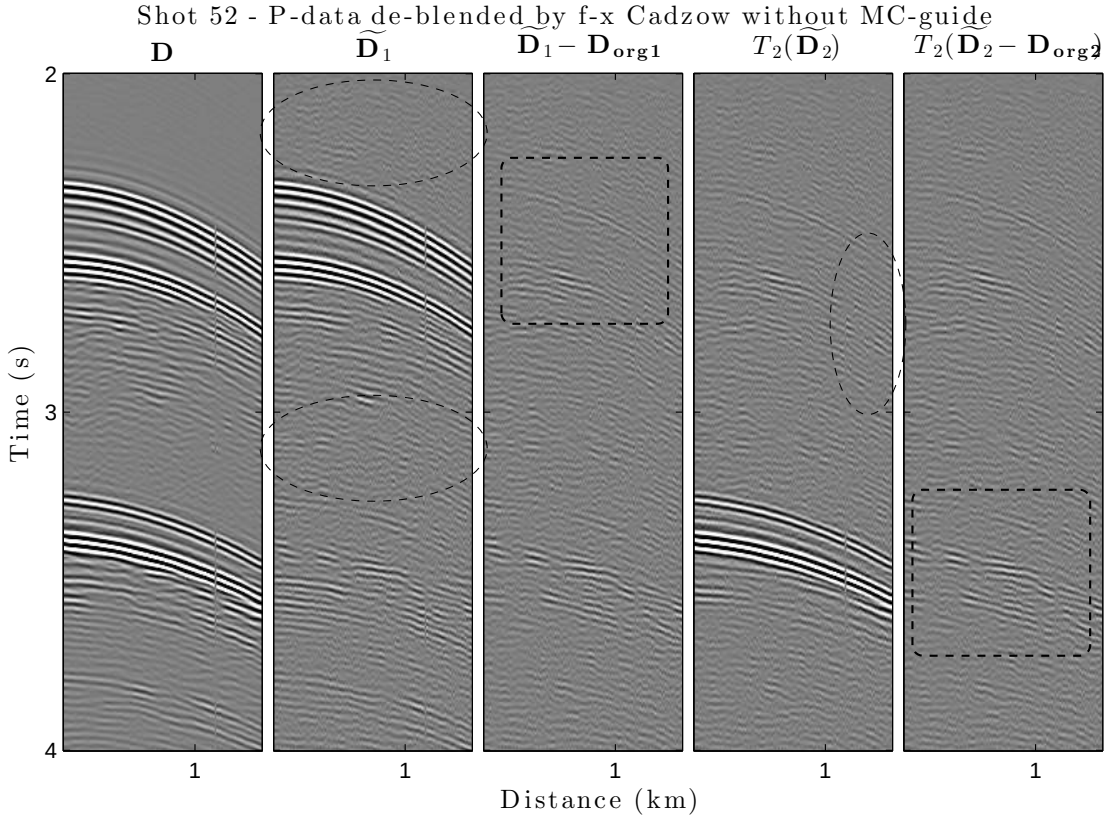

(a)

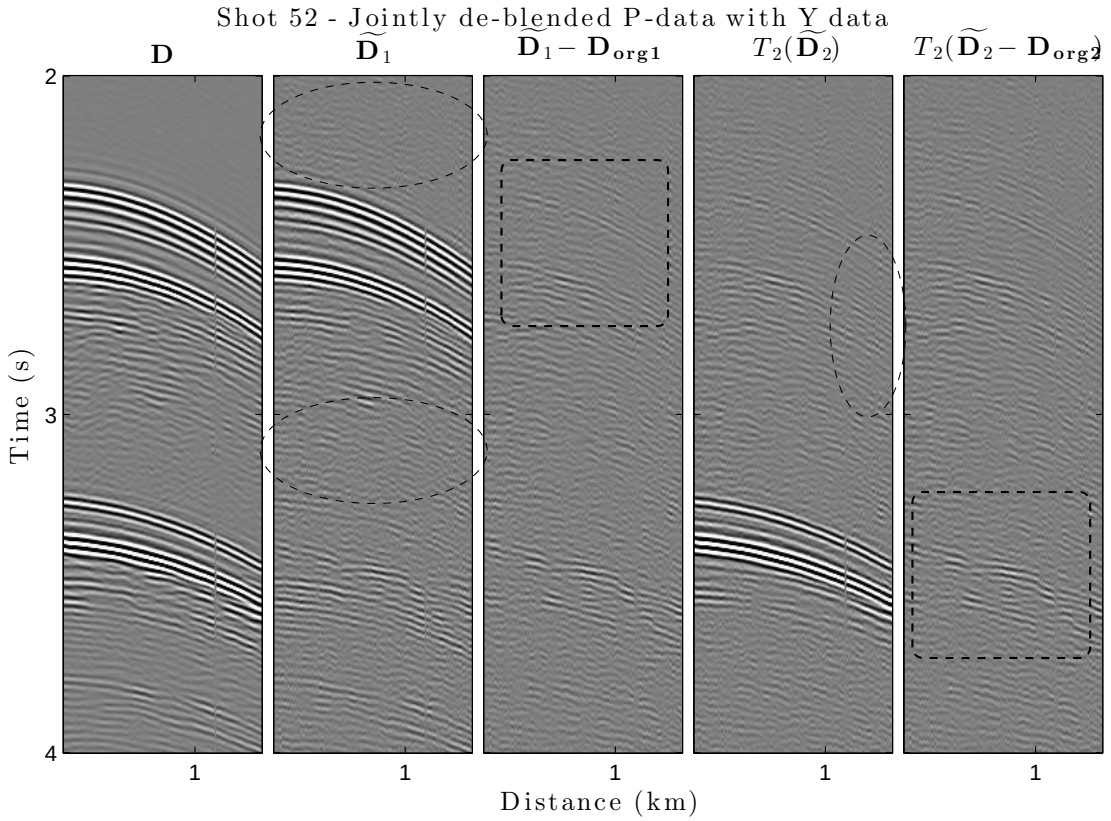

(b)

Figure 5.11: P data de-blended in shot domain. (a) With P data only. (b) Jointly with Y data.

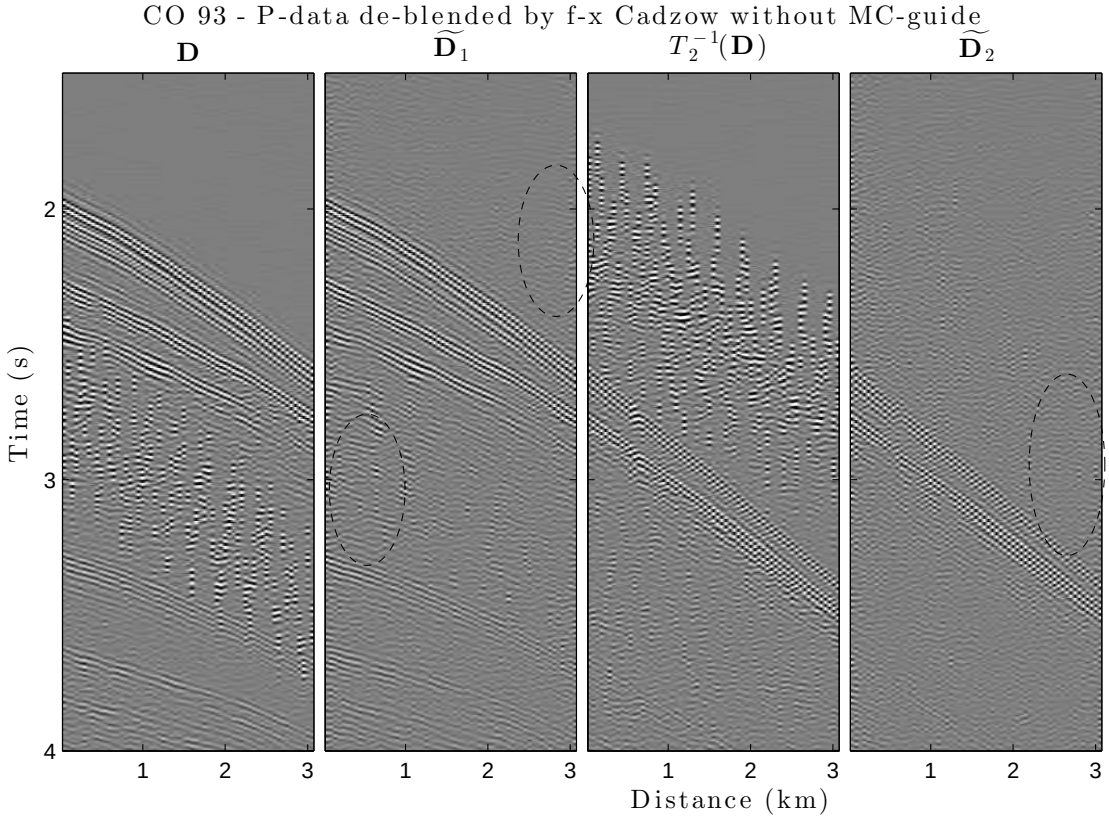

(a)

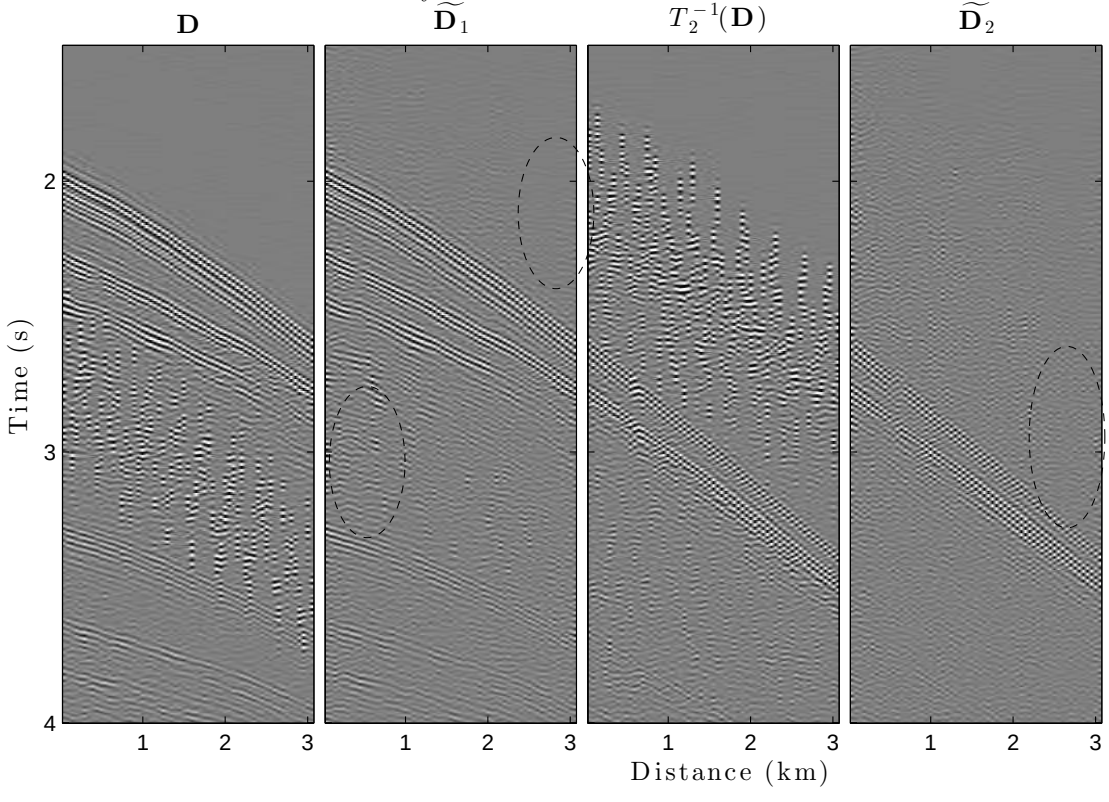

(b)

Figure 5.12: P data de-blended in CO domain. (a) Using P-data only. (b) Jointly with Y data.

De-blending and de-noising of Y data

The de-blending and de-noising results for Y data are shown in Figure 5.13. Figure 5.13a shows one blended shot de-noised and de-blended into its respective sources. The de-noising has not managed to attenuate all the blending noise. Some coherent energy from the other shot is also retained, marked with solid circles. The multi-sensor noise has been attenuated, but not completely removed, and the most prominent noise is marked with ellipses. Figure 5.13b shows one common offset section in both time-configurations, $\mathbf{Y}$ and $T_2^{-1}(\mathbf{Y})$, de-blended and de-noised. Going through all the 120 CO sections, 65 out of 120 CO sections have been de-blended and de-noised well. For these results also the amplitude is preserved well.

De-blending and de-noising of Z data

The results from the de-noising and de-blending of the Z data are shown in Figure 5.14. The same comments as for Figure 5.13 follow, but this time, 38 out of 120 CO sections are de-noised and de-blended well. For the Z data, the amplitude is not preserved after de-noising and de-blending.

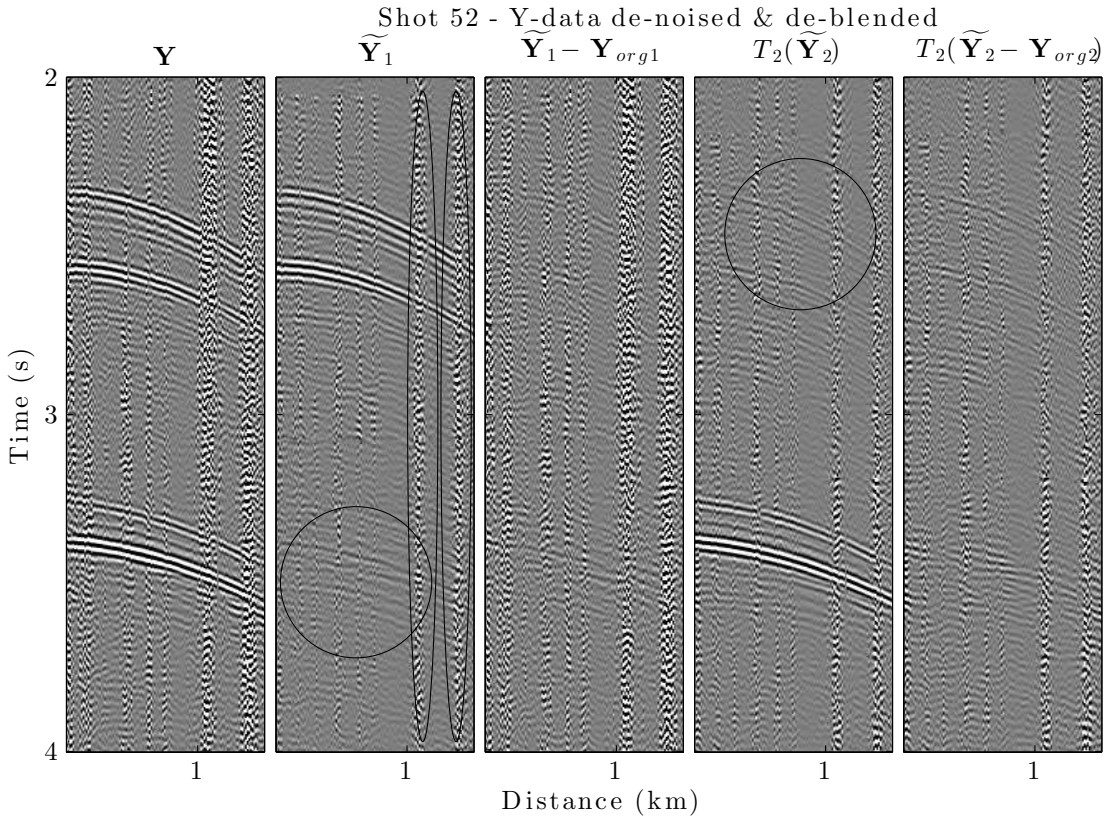

(a) Common shot domain

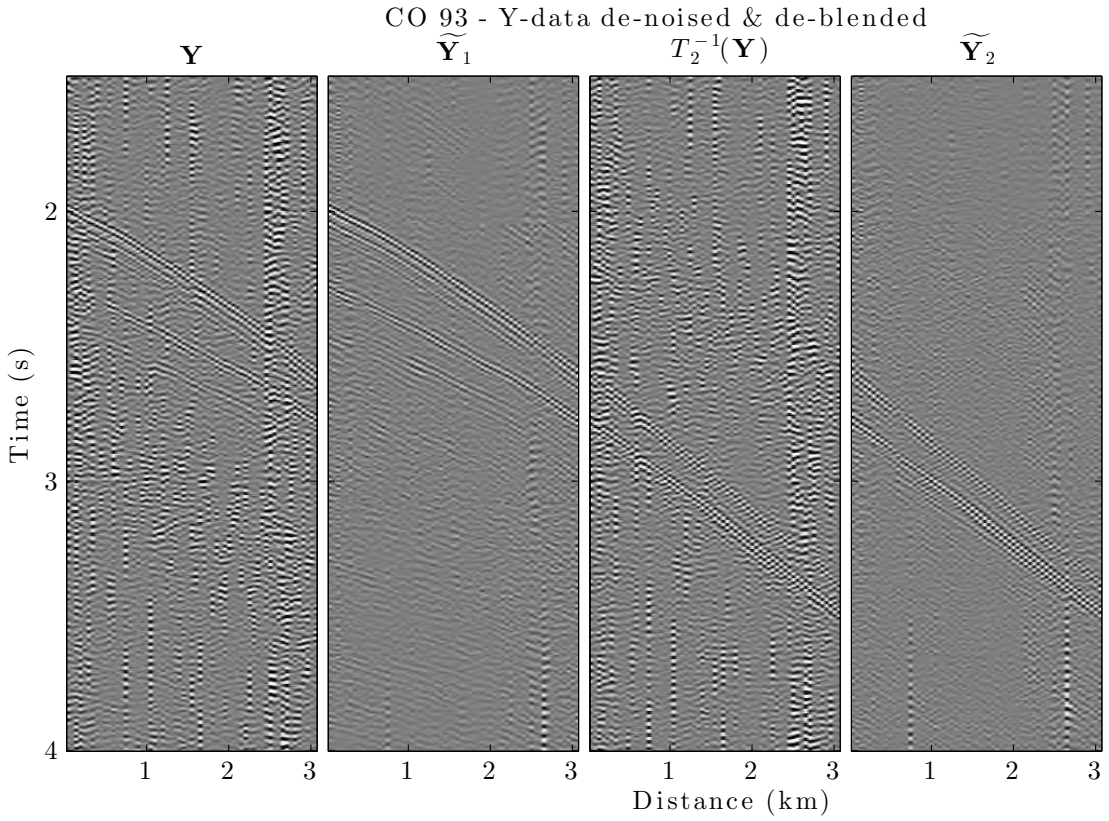

(b) Common offset domain

Figure 5.13: Y data de-noised and de-blended.

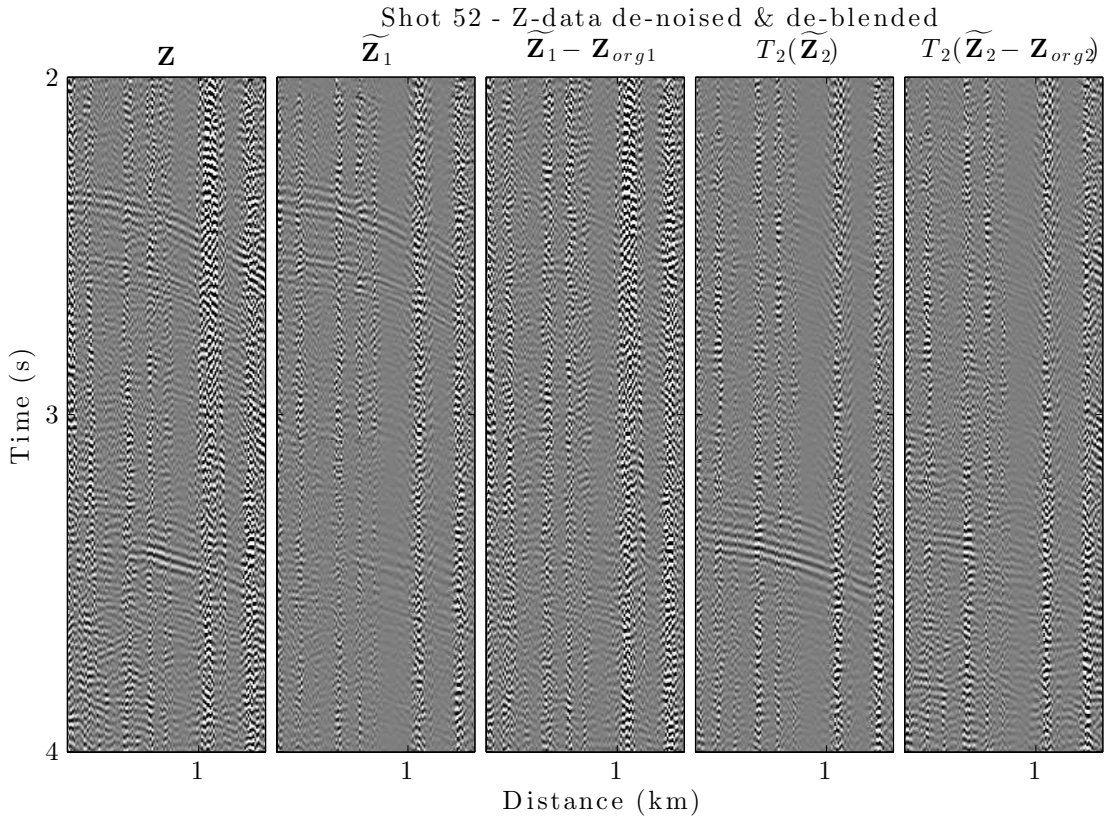

(a) Common shot domain.

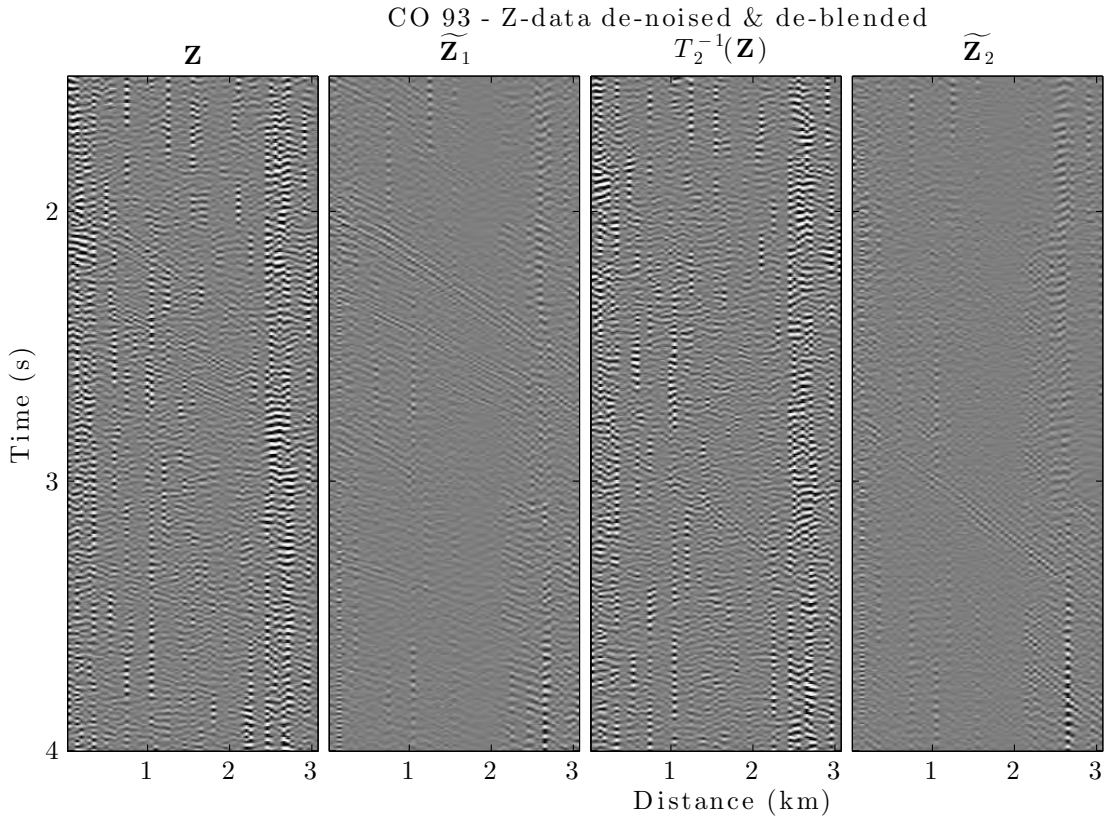

(b) Common offset domain.

Figure 5.14: Z data de-noised and de-blended.

6 Discussion

As for now, the f-x Cadzow has been tested on a numerically blended real dataset using P data only. However, a discussion of how necessary the deblending step is for the final image should be engaged. Furthermore, we have investigated one way of using multicomponent data to improve de-blending.

6.1 Active vs. passive de-blending

The comparison done in this thesis between passive, i.e. by stacking and migration, and active de-blending is limited. To truly compare active and passive de-blending, pre-stack time or depth migration should have been applied to the data. Furthermore, if we had 3D data, more points would have been used in the migration, improving both passive and active de-blending.

The main advantage regarding active de-blending is that we can process the de-blended data using conventional workflows. As algorithms for processing blended data directly get more and more mature, the de-blending step, would not be necessary. However, the de-blending step may be included in these algorithms to bring extra information in the direct processing of the blended data.

After processing blended data by stacking and post-stack migration, two interesting features have been observed for the two different blending scenarios. For scenario 1, where both sources are on the same side of the receivers, the blending noise looks like a feather masking the reflectors. For scenario 2, where the two sources are at opposite sides of the receivers, the blending noise has a different character. It is characterized as vertical lines inclined to the right. For both scenarios the blending noise is due to stacking of the data. If a mute was to be applied on the common-midpoint (CMP) gathers before normal move out (NMO) correction, the blending noise would have disappeared above the sea-floor. For scenario 2, the blending noise comes from a different CMP and has high amplitude from the receivers furthest away from source 1. Therefore, when NMO correction is applied to the data a NMO stretch occurs due to that the NMO correction is not a linear correction. The stacking of these NMO corrected CMP gathers results in the vertical lines inclined to the right observed. For scenario 1, the blending noise is not NMO-stretched more than the original data. This is due to the sources being on the same side of the receiver, and therefore amplitudes are similar for both sources in the traces in

the CMP-gather. By stacking, the signal-to-noise amplitude ratio is approximately improved by $\sqrt{N}$ (Robinson, 1970), where N is the number of traces. The same principle applies for the post-stack migration, where either energy along scattering isochrones or travel times are stacked. In this way, the blending noise is seen as random and further reduced, as observed.

6.2 De-blending using f-x Cadzow

When de-blending data using the f-x Cadzow we have observed the following: Random noise contaminates data gathers, some coherent energy and events with high curvature, such as diffractions, have been attenuated.

One of the drawbacks of the f-x Cadzow filter is the averaging of the Hankel matrices. This averaging step explains the random noise contamination, especially above the seafloor. Some solutions could be tried to solve this problem:

- By muting the data above primary reflector the random noise above the sea-floor is attenuated.
- By thresholding, one can reconstruct the data more gradually, and the random noise created by the averaging of the Hankel matrices is attenuated by the thresholding and will not be taken further.

Attenuation of coherent energy could be solved by looking at the residuals. A problem with the residuals is that some coherent energy relating to one source is in the estimation of the other source. This happens when the method does not manage to remove the blending noise completely, and therefore when time-shifted and subtracted from the other source, coherent energy is withdrawn. A few possible solutions that should be tested:

- Thresholding the data.
- Try to find coherent energy in the other source and re-estimate it back to the other source.

High curvature needs to be reconstructed with many dips, and therefore many eigenimages. Using many eigenimages in the reconstruction will also keep blending noise created by the diffraction. A solution to this problem could be to convert the data to another domain where the diffractions do not have such a high curvature.

6.3 Joint deblending of P and MC data

In this thesis, we have proposed an implementation of joint de-blending of P and MC data where the objective was double: Improve the deblending of P data and simultaneously de-blend MC data. Compared with only using P data in the de-blending, the proposed method gave both a marginal improvement in number of iterations used before convergence, and in the quality of the de-blending. Furthermore, the Y and Z data were de-blended and de-noised satisfactorily.

An interesting observation was that the de-noised and de-blended Z data did not retain its amplitudes. This could be related to two factors: a low SNR but also in this case, P and Z having a different receiver ghosts. When P and Z data have different ghosts, the mismatch in the reflection wavelets yields a non-optimal denoising of MC data. For future analysis, the P and Z data should be conditioned by applying a de-ghosting re-ghosting processing algorithm (Poole, 2013), so that they have the same receiver ghost.

As for now, due to some overlapping windows having a low SNR, the method goes back to only using P data if the evaluation of the first eigenvalue does not pass the ratio threshold. This is a critical area of the method and a more robust evaluation should be investigated further to increase the robustness of the method.

Furthermore, the data have been numerically blended where one source has been de-noised beforehand, so it actually differs from real recorded blended MC data. The data was from a WAZ survey where the sources were from the same sailing line. It would be interesting to use the MC data where two sources have a different sail-line, and therefore different MC signature.

A note should be given on the de-noising of MC data in common offset sections. A CO gather comes from the same receiver. If this receiver is not optimally configured or if it is very prone to noise, the whole CO section is contaminated by noise. For these CO-sections the SNR is extremely low, and therefore the de-noising fails. For this reason, it may be worth trying to de-noise shot gathers one more time after de-blending.

Finally, this is to our knowledge one of the first attempt to use MC data for deblending. For this reason, more tests should be conducted before we can draw a final conclusion about this method.

7 Conclusion and future work

From the results and discussion in this thesis the following conclusions can be drawn:

- Results from the synthetic dataset *Pluto* suggest that using a f-x Cadzow filter is better than a hybrid TFDN/f-x Cadzow in terms of faster convergence and better results.
- Using the f-x Cadzow filter iteratively de-blends the data successfully, but introduces some random noise where hardly any data are present. Furthermore, some coherent energy, as well as events with high curvature such as diffractions have been attenuated.
- Jointly de-blending of P and MC data, using middle frequencies (31-55 Hz) converged marginally faster when using either Z or Y data. The end result was also marginally better visually and in terms of having a lower NRMS value than using P-only in the de-blending.
- The Y and Z data were de-noised and de-blended satisfactorily for middle frequencies. But, the Z data did not retain its amplitudes, due to low SNR and due to having a different receiver ghost than P data.

Based on the results and discussion of this thesis following recommendations are given for future work:

f-x Cadzow:

- Investigating if thresholding at each iteration could improve: Contamination by random noise where hardly any data are present, and improving the estimation of coherent energy.
- Investigate different blending strategies impact on the de-blending. Understand how the blending of the data impacts the de-blending.
- Investigate if wrongly estimated data could be added back to its original source.

Using multicomponent data:

- Apply a de-ghosting and re-ghosting processing algorithm so P and Z data have the same receiver ghost.
- Investigate the use of MC data when the sources have different sail-lines.

- Only the conservative estimate of the P data are evaluated for both sources. And investigation considering if also evaluating the estimate after filtering could improve the method should be taken.
- For now the method falls back to only using P-data if the first eigenvalue do not pass the ratio threshold. A more robust method should be investigated to decide if we should drop the evaluation step or not.
- Add another step of de-noising of MC data in shot domain after de-blending.
- Investigate the use of high frequencies, and find the lower border for the use of low frequencies.

List of Figures

1.1 A marine seismic survey . . . 2
1.2 Streamer Technology . . . 3
1.3 Collocated pressure and motion sensor . . . 4

2.1 Example of Multiples . . . 10
2.2 Example of Ghost reflections . . . 11
2.3 Example of Ghost free data (amplitude spectrum) . . . 11
2.4 Example of Diffraction . . . 12
2.5 Example of Seismic interference . . . 12
2.6 f-k spectrum of transversal and longitudinal vibrations and angular vibrations plots . . . 15

3.1 Frequency filter . . . 18
3.2 F-K dip filtering . . . 19
3.3 $\tau - p$ transformation . . . 20
3.4 F-X Prediction: Synthetic example 1 . . . 22
3.5 SVD Example 1 . . . 24
3.6 SVD examples . . . 25
3.7 f-x Cadzow Flow Chart . . . 27
3.8 Cadzow examples . . . 29
3.9 f-x Cadzow: Eigenimages . . . 30
3.10 Energy in eigenimages . . . 31
3.11 Cadzow on blending noise . . . 31
3.12 TFDN on blending noise . . . 33
3.13 Joint de-noise of MC data - Workflow . . . 34

4.1 Blended data in different domains . . . 37
4.2 Shot domain and common offset domain . . . 38
4.3 Flowchart de-blending 1 . . . 39
4.4 Flowchart de-blending 2 . . . 41
4.5 Hybrid filter - Workflow . . . 43
4.6 Comparison Hybrid and Cadzow - Window . . . 44
4.7 Comparison Hybrid and Cadzow - RMS . . . 45
4.8 Time-shifting inside window . . . 46
4.9 Example of different window sizes . . . 46
4.10 Workflow for the joint de-blending and de-noising of P data . . . 50
4.11 Flowchart de-blending using MC data . . . 51

5.1 Blended Faroese acquisition design 57
5.2 Scenario 1 - Faroese: One shot de-blended 59
5.3 Faroese: Migration of $\mathbf{D}_1$ & T_1 60
5.4 Faroese: Difference and NRMS of migration $\mathbf{D}_1$ & T_1 61
5.5 Scenario 2 - Faroese: One shot de-blended 63
5.6 Scenario 2 Faroese: Migration of $\mathbf{D}_1$ & T_1 64
5.7 Scenario 2 Faroese: Difference and NRMS of migration $\mathbf{D}_1$ & T_1 65
5.8 WAZ - Analysis P data 67
5.9 WAZ - Analysis Z data 68
5.10 WAZ - Analysis Y data 69
5.11 WAZ dataset de-blended with and without MC-data in shot domain 72
5.12 WAZ dataset de-blended with and without MC-data in CO domain 73
5.13 Y data de-noised and de-blended 75
5.14 Z data de-noised and de-blended 76

B.1 Scenario 1: Faroese $\mathbf{D}_2$- Migrations 88
B.2 Scenario 1 - Difference and NRMS of T_2 and $\mathbf{D}_2$ of migration 89
B.3 Scenario 2 - Faroese $\mathbf{D}_2$ Migrations 90
B.4 Scenario 2 - Faroese Migration - Difference and NRMS of T_2 and $\mathbf{D}_2$ 91

List of Tables

1.1 Different configurations for hydrophone only streamers 2

2.1 List of different coherent and random noise types. 9

4.1 Brief comparison - Parameters and Results 44
4.2 Parameters that can be set in the de-blending of P data 49
4.3 MC - other attempts 53

5.1 Acquisition geometry for the Faroese dataset. 56
5.2 Faroese data: parameters used 57
5.3 Faroese - Results scenario 1 59
5.4 Faroese - Results scenario 2 62
5.5 Multicomponent dataset: parameters used 70
5.6 Results for WAZ data with and without MC guide 71

A Characterization of noise modes in multicomponent streamers

This appendix goes through the equations in the article 'Characterization of noise modes in multicomponent(4C) towed streamers' presented by Teigen et al. (2012).

A.1 Transverse vibrations

The equation of motion describing the transverse displacement $\psi(t,x)$ of a stiff streamer can be approximated by the transverse vibration of a slender uniform beam subjected to axial tension:

$$EI\frac{\partial^4\psi(x,t)}{\partial x^4} - T\frac{\partial^2\psi(x,t)}{\partial x^2} + m\frac{\partial^2\psi(x,t)}{\partial t^2} = h(x,t), \tag{A.1}$$

where E is the Young's modulus, I is the moment of inertia, T is the axial tension, m is the mass per unit length, t is time, x is the coordinate of the inline axis, and $h(x,t)$ is the external force per unit length. For a buoyant and stationary streamer $m = \pi d^2\rho/4$, where d is the outer diameter of the streamer, ρ is the density of sea water. When the streamer is towed ρ is replaced by ρ_a due to extra weight from the displaced water that moves with the streamer.

The eigenfunctions of equation A.1 give the resonance frequencies and wavenumbers, i.e., frequencies and wavenumbers at which the vibration noise has its peak amplitudes and is on the following form: $g(x,t) = e^{j2\pi(ft+kx)}$. Leading to the following characteristic equation:

$$4\pi^2\frac{k^4}{f^2}EI + \frac{k^2}{f^2}T - \frac{\pi d^2\rho_a}{4} = 0. \tag{A.2}$$

The corresponding phase velocity can then be given as

$$v_p(k) \equiv \frac{f(k)}{k} = \frac{2}{d}\sqrt{\frac{4\pi^2k^2EI + T}{\pi\rho_a}}. \tag{A.3}$$

If the streamer is fluid- or gel-filled, the Young modulus, E, in A.2 can be set to zero and therefore the dispersion relation in A.1 becomes

$$\frac{k^2}{f^2}T - \frac{\pi d^2 \rho_a}{4} = 0 \tag{A.4}$$

corresponding to a phase velocity of

$$v_p(k) \equiv \frac{f(k)}{k} = \frac{2}{d}\sqrt{\frac{T}{\pi \rho_a}}. \tag{A.5}$$

This phase velocity does not change with the frequency ,i.e., it is not dispersive.

A.2 Longitudinal vibrations

The equation of motion describing the longitudinal displacement $\varphi(t,x)$ of a stiff streamer can be given as:

$$EA\frac{\partial^2 \varphi(x,t)}{\partial x^2} - m\ddot{\varphi}(x,t) = q(x,t), \tag{A.6}$$

where E is the Young's modulus, A is the cross sectional area, m is the mass per unit length and $q(x,t)$ is the forcing term.

The phase velocity can be given as:

$$v_p(k) \equiv \frac{f(k)}{k} = \sqrt{\frac{EA}{m}}. \tag{A.7}$$

A.3 Angular vibrations

The equation of motion describing angular displacement $\Theta(t,x)$ can be given as:

$$G\frac{\partial^2 \Theta(x,t)}{\partial x^2} - \rho\ddot{\Theta}(x,t) = 0, \tag{A.8}$$

where G is the shear modulus of elasticity and ρ the density.

B Faroese test - Additional results

Additional results for the Faroese 2D field data for completion.

B.1 Scenario 1

Figure B.1 shows migrated data for time-configuration 2, and de-blended data from source 2. Figure B.2 shows difference and NRMS plots, showing the blending noise and estimation error.

B.2 Scenario 2

As for scenario 1, the migrated data for the second time-configuration and de-blended source are shown in Figure B.3 for scenario 2. The difference and NRMS plots are shown in Figure B.4.

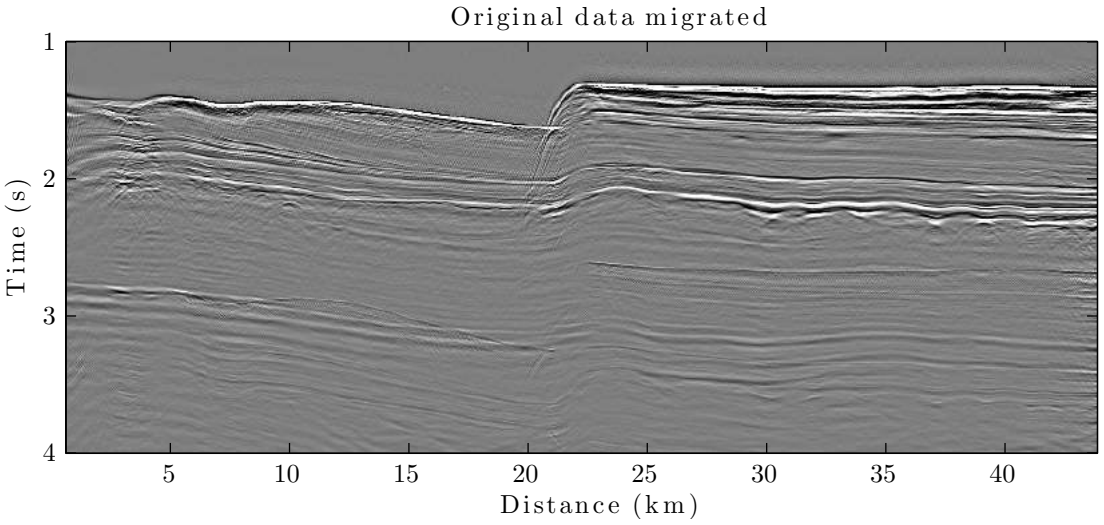

(a) Original data migrated

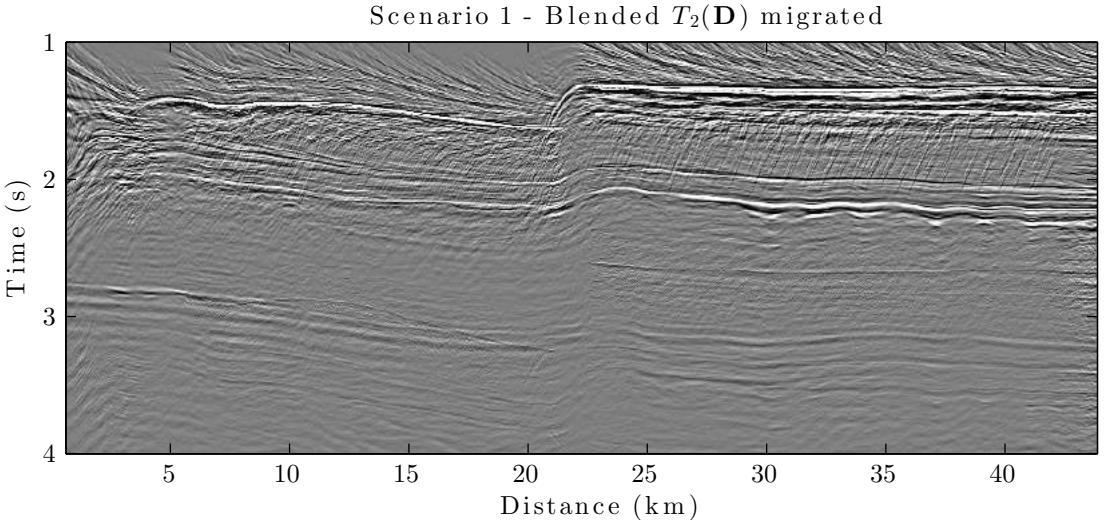

(b) Blended migration of $T_2(\mathbf{D})$

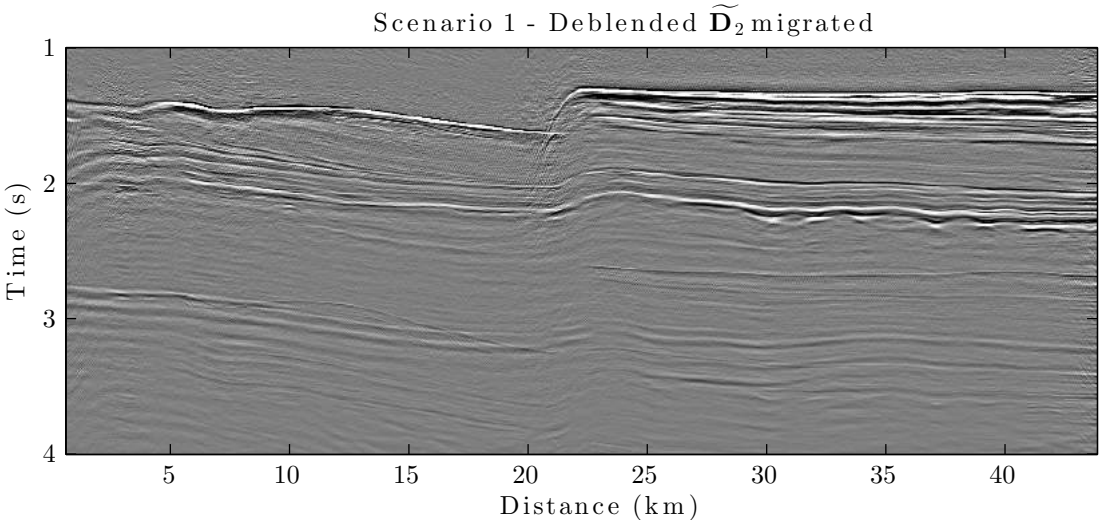

(c) De-blended migration of $\widetilde{\mathbf{D}}_2$

Figure B.1: Scenario 1. Migrated data: (a) Original data. (b) Blended data: $T_2(\mathbf{D})$. (c) De-blended: $\widetilde{\mathbf{D}}_2$.

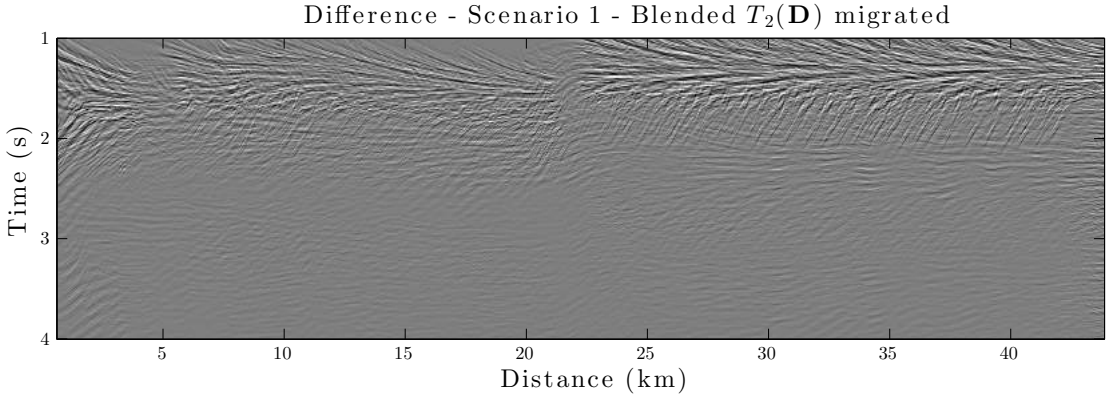

(a) Blending noise after migration.

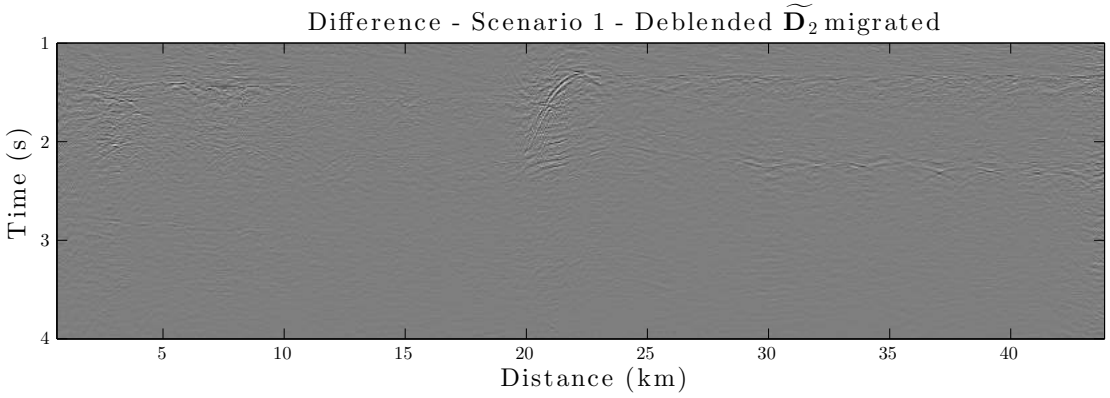

(b) Estimation error after migration.

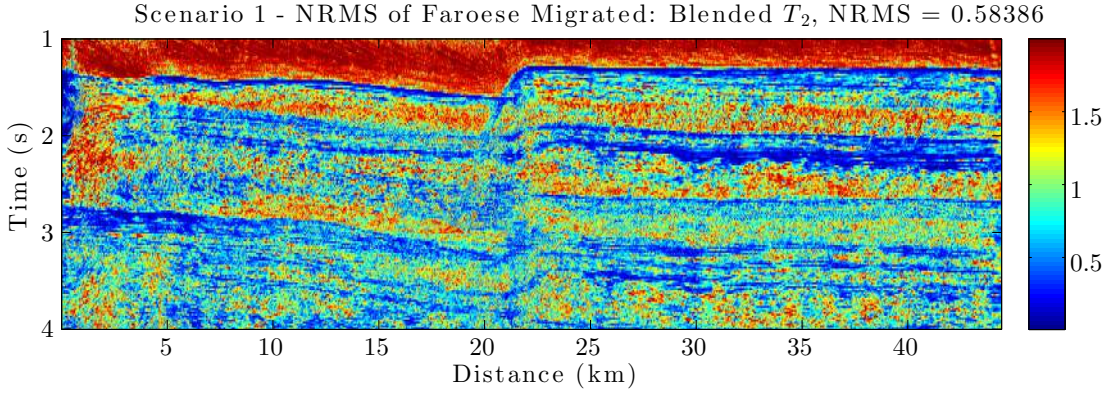

(c) NRMS of the blending noise after migration.

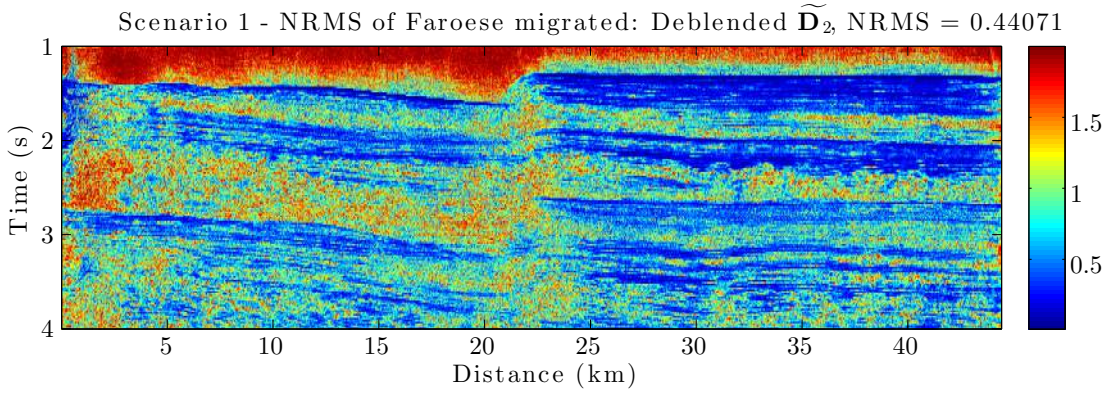

(d) NRMS of the estimation error after migration.

Figure B.2: Migration: (a) Blending noise. (b) Estimation error. NRMS plots: (c) Blending noise after migration. (d) Estimation error after migration.

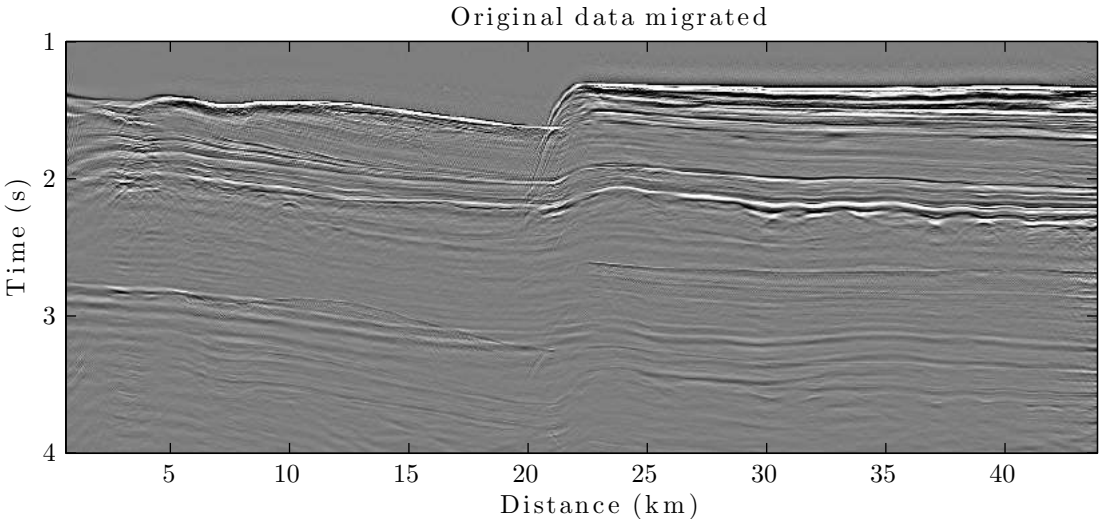

(a) Original data migrated

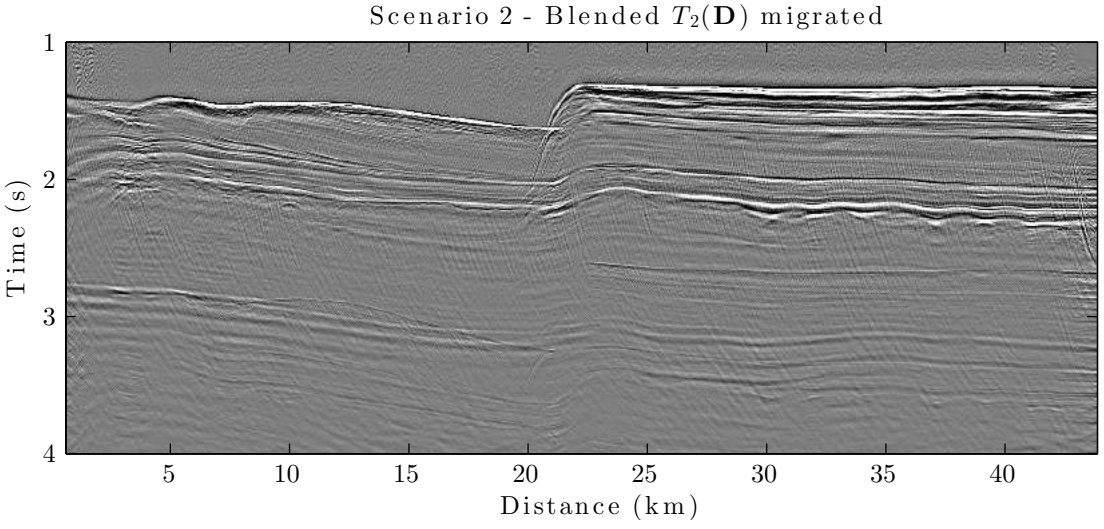

(b) Blended migration of $T_2(\mathbf{D})$

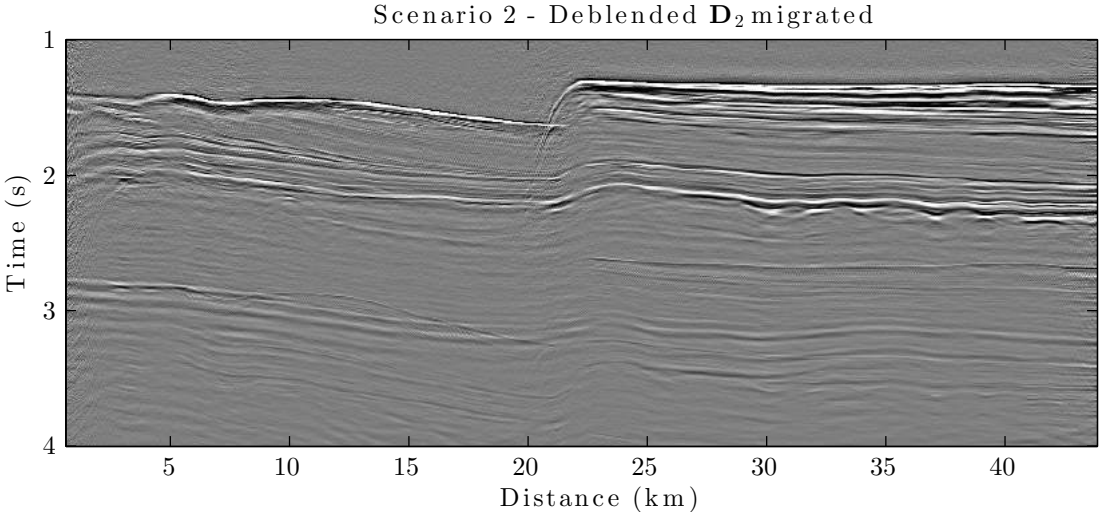

(c) De-blended migration of $\mathbf{D}_2$

Figure B.3: Scenario 2. Migrated data: (a) Original data. (b) Blended data: $T_2(\mathbf{D})$. (c) De-blended: $\widetilde{\mathbf{D}_2}$.

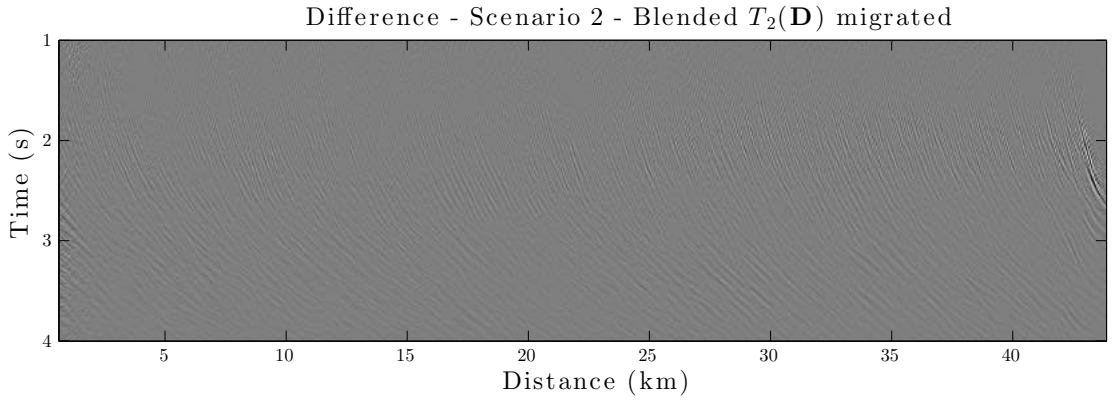

(a) Blending noise after migration.

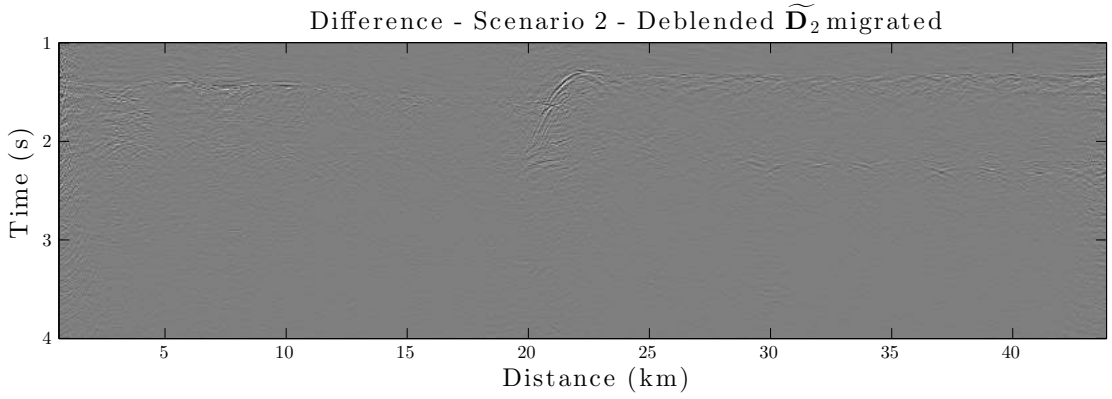

(b) Estimation error after migration.

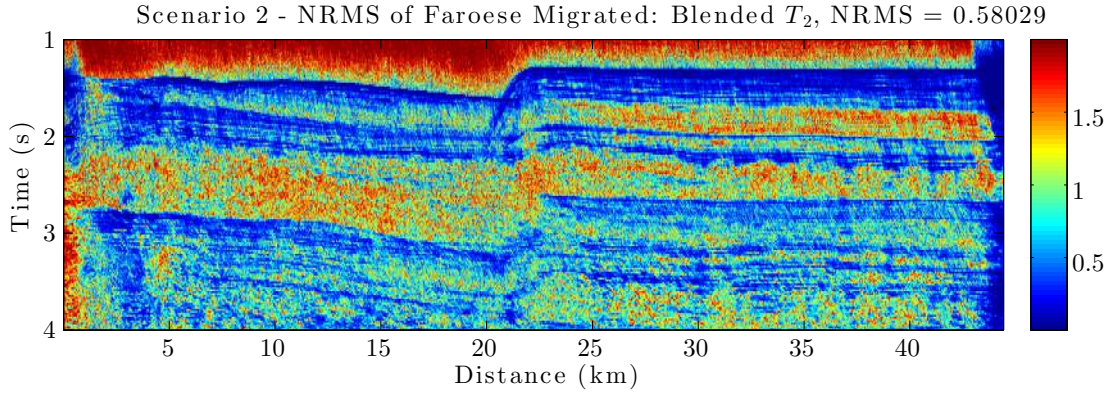

(c) NRMS of the migrated datasets original and blended

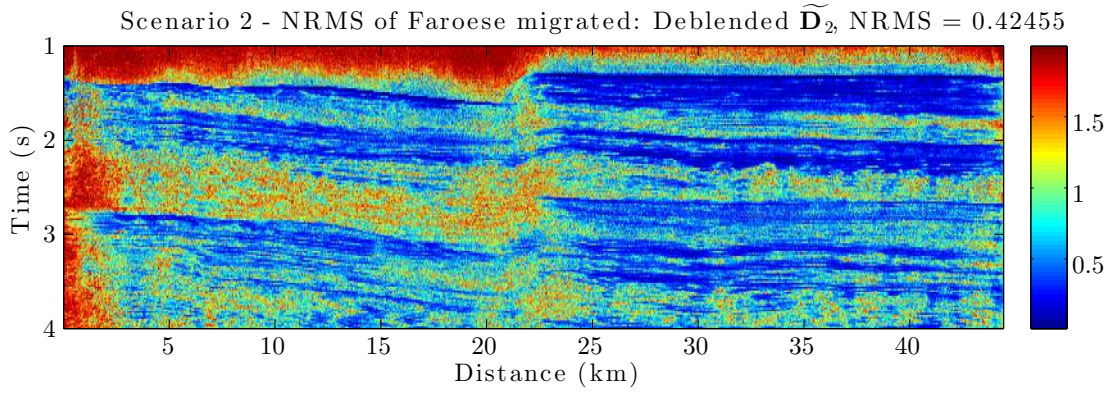

(d) NRMS of the migrated datasets original and deblended.

Figure B.4: Scenario 2. Migrated data: (a) Blending noise. (b) Estimation error. NRMS plots: (c) Blending noise after migration. (d) Estimation error after migration.

Bibliography

Abma, R. L., Manning, T., Tanis, M., Yu, J., and Foster, M. 2010. High quality separation of simultaneous sources by sparse inversion. *72nd Annual International Conference and Exhibition, EAGE, Extended Abstracts*. doi:10.3997/2214-4609.201400611.

Akerberg, P., Hampson, G., Rickett, J., Martin, H., and Cole, J. 2008. Simultaneous source separation by sparse radon transform. *78th Annual International Meeting, SEG, Expanded Abstracts*, 2801–2805. doi:10.1190/1.3063927.

Bagaini, C. 2006. Overview of simultaneous vibroseis acquisition methods. *76th Annual International Meeting, SEG, Expanded Abstracts*, 70–74. doi:10.1190/1.2370358.

Barbier, M. and Staron, P. 1972. Method of exploring a medium by transmitting energy emitted in the form of separate impulses and its application to seismic prospecting. US Patent 3,811,111.

Barbier, M. G. and Viallix, J. R. 1974. Pulse coding in seismic prospecting sosie and seiscode. *Geophysical Prospecting* 22 (1), 153–175. doi:10.1111/j.1365-2478.1974.tb00071.x.

Beasley, C. J., Chambers, R. E., and Jiang, Z. 1998. A new look at simultaneous sources. *68th Annual International Meeting, SEG, Expanded Abstracts*, 133–135. doi:10.1190/1.1820149.

Bekara, M. and van der Baan, M. 2007. Local singular value decomposition for signal enhancement of seismic data. *Geophysics* 72 (2), 59–65. doi:10.1190/1.2435967.

Berkhout, A. J. 2008. Changing the mindset in seismic data acquisition. *The Leading Edge* 27 (7), 924–938. doi:10.1190/1.2954035.

Berkhout, A. J. 2013. Decentralized blended acquisition-are networks the next big step in seismic data collection? *75th Annual International Conference and Exhibition, EAGE, Extended Abstracts*. doi:10.3997/2214-4609.20130085.

Berkhout, A. J., Blacquière, G., and Verschuur, D. J. 2009. The concept of double blending: Combining incoherent shooting with incoherent sensing. *Geophysics* 74 (4), A59–A62. doi:10.1190/1.3141895.

Berkhout, A. J., Verschuur, D. J., and Blacquière, G. 2012. Illumination properties and imaging promises of blended, multiple-scattering seismic data: a tutorial. *Geophysical Prospecting* 60 (4), 713–732. doi:10.1111/j.1365-2478.2012.01081.x.

Berni, A. J. May 28 1985. Marine seismic system. US Patent 4,520,467.

Blacquière, G. and Ongkiehong, L. 2000. Single sensor recording: Anti-alias filtering, perturbations and dynamic range. *70th Annual International Meeting, SEG, Expanded Abstracts* 33–36. doi:10.1190/1.1816060.

Broomhead, D. S. and King, G. P. 1986. Extracting qualitative dynamics from experimental data. *Physica D: Nonlinear Phenomena* 20 (2), 217–236. doi:10.1016/0167-2789(86)90031-X.

Cadzow, J. 1988. Signal enhancement a composite property mapping algorithm. *IEEE Transactions on Acoustics, Speech, and Signal Processing* 36, 49–62. doi:10.1109/29.1488.

Canales, L. L. 1984. Random noise reduction. *54th Annual International Meeting, SEG, Expanded Abstracts*, 525–527. doi:10.1190/1.1894168.

Cao, Z., Bancroft, J., Brown, R., and Xaio, C. 2003. Radon transform and multiple attenuation. Technical report, CREWES Research Report.

Caprioli, P., Özdemir, K., van Manen, D.-J., Mahat, S., Özbek, A., Kragh, E., and Christie, P. 2012. Combination of multi-component streamer pressure and vertical particle velocity: Theory and application to data. *82nd Annual International Meeting, SEG, Expanded Abstracts*, 1–5. doi:10.1190/segam2012-1144.1.

Carlson, D., Long, A., Söllner, W., Tabti, H., Tenghamn, R., and Lunde, N. 2007. Increased resolution and penetration from a towed dual-sensor streamer. *First Break* 25 (12).

Chen, Y. 2014. Deblending using a space-varying median filter. *84th Annual International Meeting, SEG, Expanded Abstracts*, 82–87. doi:10.1190/segam2014-0325.1.

Cheng, J. and Sacchi, M. D. 2013. Separation of simultaneous source data via iterative rank reduction. *83rd Annual International Meeting, SEG, Expanded Abstracts*, 88–93. doi:10.1190/segam2013-1313.1.

Choi, Y. and Alkhalifah, T. 2012. Application of multi-source waveform inversion to marine streamer data using the global correlation norm. *Geophysical Prospecting* 60 (4), 748–758. doi:10.1111/j.1365-2478.2012.01079.x.

Doulgeris, P., Bube, K., Hampson, G., and Blacquière, G. 2012. Convergence analysis of a coherency-constrained inversion for the separation of blended data. *Geophysical Prospecting* 60 (4), 769–781. doi:10.1111/j.1365-2478.2012.01088.

Dowle, R. 2006. Solid streamer noise reduction principles. *76th Annual International Meeting, SEG, Expanded Abstracts*, 85–89. doi:10.1190/1.2370392.

Dragoset, B. 2005. A historical reflection on reflections. *The Leading Edge* 24 (1), 46–70. doi:10.1190/1.2112392.

Elboth, T. and Hermansen, D. 2009. Attenuation of noise in marine seismic data. *79th Annual International Meeting, SEG, Expanded Abstracts*, 3312–3316. doi:10.1190/1.3255547.

Elboth, T., Qaisrani, H. H., and Hertweck, T. 2008. De-noising seismic data in the time-frequency domain. *78th Annual International Meeting, SEG, Expanded Abstracts*, 2622–2626. doi:10.1190/1.3063887.

Frijlink, M., van Borselen, R., and Söllner, W. 2011. The free surface assumption for marine data-driven demultiple methods*. *Geophysical Prospecting* 59 (2), 269–278. doi:10.1111/j.1365-2478.2010.00914.x.

Galbraith, M. 1991. Random noise attenuation by f-x prediction: A tutorial. *61th Annual International Meeting, SEG, Expanded Abstracts*, 1428–1431. doi:10.1190/1.1889082.

Gelius, L.-J. and Johansen, T. A. 2010. *Petroleum geophysics*. Bergen: Unigeo. 660 pp.

Gu, Y. J. and Sacchi, M. 2009. Radon transform methods and their applications in mapping mantle reflectivity structure. *Surveys in geophysics* 30 (4-5), 327–354. doi:10.1007/s10712-009-9076-0.

Guitton, A. and Díaz, E. 2012. Attenuating crosstalk noise with simultaneous source full waveform inversion. *Geophysical Prospecting* 60 (4), 759–768. doi:10.1111/j.1365-2478.2011.01023.x.

Hampson, G., Stefani, J., and Herkenhoff, F. 2008. Acquisition using simultaneous sources. *The Leading Edge* 27 (7), 918–923. doi:10.1190/1.2954034.

Hayes, H. C. 1920. Detection of submarines. *Proceedings of the American Philosophical Society* 59 (1), 1–47.

Huo, S., Luo, Y., and Kelamis, P. G. 2012. Simultaneous sources separation via multidirectional vector-median filtering. *Geophysics* 77 (4), V123–V131. doi:10.1190/geo2011-0254.1.

Ibrahim, A. and Sacchi, M. D. 2013. Simultaneous source separation using a robust radon transform. *Geophysics* 79 (1), V1–V11. doi:10.1190/geo2013-0168.1.

Ikelle, L. 2007. Coding and decoding: Seismic data modeling acquisition and processing. *77th Annual International Meeting, SEG, Expanded Abstracts*, 66–70. doi:10.1190/1.2792383.

Ikelle, L. T. and Amundsen, L. 2005. *Introduction to Petroleum Seismology*. Tulsa: Society of Exploration Geophysicists. 315–359. doi:10.1190/1.9781560801702.ch8.

Kim, Y., Gruzinov, I., Guo, M., and Sen, S. 2009. Source separation of simultaneous source obc data. *79th Annual International Meeting, SEG, Expanded Abstracts*, 51–55. doi:10.1190/1.3255810.

Kozola, S. 2001. Large data in matlab: A seismic data processing case study. http://www.mathworks.com/matlabcentral/fileexchange/30585. (Accessed: 20.06.14).

Kragh, E. and Christie, P. 2002. Seismic repeatability, normalized rms, and predictability. *The Leading Edge* 21 (7), 640–647. doi:10.1190/1.1497316.

Lawyer, L. L., Bates, C. C., and Rice, R. B. 2001. *Geophysics in the Affairs of Mankind*. Society of Exploration Geophysicists. 507 pp. doi:10.1190/1.9781560801788.

Lin, T. T. Y. and Herrmann, F. J. 2009. Designing simultaneous acquisitions with compressive sensing. *71st Annual International Conference and Exhibition, EAGE, Extended Abstracts*. doi:10.3997/2214-4609.201400276.

Magnussen, F. 2015. Iterative source separation using a hybrid cadzow and median filter. *77th Annual International Conference and Exhibition, EAGE, Extended Abstracts*.

Mahdad, A. 2012. *Deblending of seismic data*. PhD thesis, TU Delft, Delft University of Technology. doi:10.4233/uuid:68883d84-3cf3-4b5c-a8ee-9c0a92604fce.

Mahdad, A., Doulgeris, P., and Blacquière, G. 2012. Iterative method for the separation of blended seismic data: discussion on the algorithmic aspects. *Geophysical Prospecting* 60 (4), 782–801. doi:10.1111/j.1365-2478.2012.01084.x.

Manolakis, D. G., Ingle, V. K., and Kogon, S. M. 2005. *Statistical and adaptive signal processing: spectral estimation, signal modeling, adaptive filtering, and array processing*. Artech House Norwood. 816 pp.

Mansour, H., Wason, H., Lin, T. T., and Herrmann, F. J. 2012. Randomized marine acquisition with compressive sampling matrices. *Geophysical Prospecting* 60 (4), 648–662. doi:10.1111/j.1365-2478.2012.01075.x.

Maraschini, M., Dyer, R., Stevens, K., Bird, D., and King, S. 2012. An iterative svd method for deblending: theory and examples. *82nd Annual International Meeting, SEG, Expanded Abstracts*, 1–5. doi:10.1190/segam2012-0675.1.

Meunier, J. 2011. *Seismic acquisition from yesterday to tomorrow*. Society of Exploration Geophysicists. 249 pp. doi:10.1190/1.9781560802853.

Moldoveanu, N., Combee, L., Egan, M., Hampson, G., Sydora, L., and Abriel, W. 2007. Over/under towed-streamer acquisition: A method to extend seismic bandwidth to both higher and lower frequencies. *The Leading Edge* 26 (1), 41–58. doi:10.1190/1.2431831.

Moore, I., Dragoset, B., Ommundsen, T., Wilson, D., Eke, D., and Ward, C. 2008. Simultaneous source separation using dithered sources. *78th Annual International Meeting, SEG, Expanded Abstracts*, 2806–2810. doi:10.1190/1.3063928.

Namorato, M. V. 2000. A concise history of acoustics in warfare. *Applied Acoustics* 59 (2), 101–135. doi:10.1016/S0003-682X(99)00021-3.

Parkes, G. E. and Hegna, S. 2012. A robust system and methodology for removing the acquisition related effects from seismic data. *74th Annual International Conference and Exhibition, EAGE, Extended Abstracts*. doi:10.3997/2214-4609.20148844.

Parrack, A. L. April 20 1976. Method of marine reflection-type seismic exploration. US Patent 3,952,281.

Pavey, J. 1966. Marine seismic cable system. US Patent 3,275,097.

Pavey, J. G. M. and Pearson, R. H. December 6 1966. Method and underwater streamer apparatus for improving the fidelity of recorded seismic signals. US Patent 3,290,645.

PGS. 2015. Ramform atlas. http://www.pgs.com/pageFolders/307413/Atlas_flier.pdf. (Accessed: 18.05.15).

Plessix, R.-É., Baeten, G., de Maag, J. W., ten Kroode, F., and Rujie, Z. 2012. Full waveform inversion and distance separated simultaneous sweeping: a study with a land seismic data set. *Geophysical Prospecting* 60 (4), 733–747. doi:10.1111/j.1365-2478.2011.01036.x.

Poole, G. 2013. Pre-migration receiver de-ghosting and re-datuming for variable depth streamer data. *83rd Annual International Meeting, SEG, Expanded Abstracts*, 4216–4220. doi:10.1190/segam2013-0541.1.

Ray, C. H. and Moore, N. A. October 5 1982. High resolution, marine seismic stratigraphic system. US Patent 4,353,121.

Reynolds, G. 2007. Complex exponential analysis. http://www.mathworks.com/matlabcentral/fileexchange/12439. (Accessed: 24.04.14).

Robertsson, J. O., Moore, I., Vassallo, M., Özdemir, K., van Manen, D.-J., and Özbek, A. 2008. On the use of multicomponent streamer recordings for reconstruction of pressure wavefields in the crossline direction. *Geophysics* 73 (5), A45–A49. doi:10.1190/1.2953338.

Robinson, J. C. 1970. Statistically optimal stacking of seismic data. *Geophysics* 35 (3), 436–446. doi:10.1190/1.1440105.

Sacchi, M. D. 2002. Statistical and transform methods for geophysical signal processing (notes). http://www.ualberta.ca/~msacchi/GEOPH426/. (Accessed: 18.05.15).

Sacchi, M. D. and Kuehl, H. 2001. Arma formulation of fx prediction error filters and projection filters. *Journal of Seismic Exploration* 9 (3), 185–198.

Sanchis, C. and Elboth, T. 2014. Multicomponent streamer noise characteristics and denoising. *84th Annual International Meeting, SEG, Expanded Abstracts*, 4183–4187. doi:10.1190/segam2014-1182.1.

Soubaras, R. 1994. Signal-preserving random noise attenuation by the f-x projection. *64th Annual International Meeting, SEG, Expanded Abstracts*, 1576–1579. doi:10.1190/1.1822843.

Soubaras, R. and Dowle, R. 2010. Variable-depth streamer–a broadband marine solution. *first break* 28 (12).

Stoughton, D., Stefani, J., and Michell, S. 2001. 2d elastic model for wavefield investigations of subsalt objectives, deep water gulf of mexico. *71st Annual International Meeting, SEG, Expanded Abstracts*, 1269–1272. doi:10.1190/1.1816325.

Teigen, O., Ozdemir, A. K., Kjellsvig, B., and Goujon, N. 2012. Characterization of noise modes in multicomponent (4c) streamers. *82nd Annual International Meeting, SEG, Expanded Abstracts* 1–5. doi:10.1190/segam2012-0792.1.

Tenghamn, R., Vaage, S., and Borresen, C. 2007. A dual-sensor, towed marine streamer; its viable implementation and initial results. *77th Annual International Meeting, SEG, Expanded Abstracts*, 989–993. doi:10.1190/1.2792571.

Timoshin, Y. V. and Chizhik, A. I. 1990. Sposob prostranstvennoy seysmorazvedki po metodu mnogokratnykh perekrytiy. SU Patent 1,543,357.

Treitel, S. 1970. Principles of digital multichannel filtering. *Geophysics* 35 (5), 785–811. doi:10.1190/1.1440130.

Trickett, S. R. 2003. F-xy eigenimage noise suppression. *Geophysics* 68 (2), 751–759. doi:10.1190/1.1567245.

Trickett, S. R. 2008. F-xy cadzow noise suppression. *78th Annual International Meeting, SEG, Expanded Abstracts*, 2586–2590. doi:10.1190/1.3063880.

Vaage, S. T. 2002. Method and system for acquiring marine seismic data using multiple seismic sources. US Patent 6,906,981.

Vassiliou, A. and Garossino, P. 1998. Computer based method of filtering geophysical time series. US Patent 5,850,622.

Vautard, R. and Ghil, M. 1989. Singular spectrum analysis in nonlinear dynamics, with applications to paleoclimatic time series. *Physica D: Nonlinear Phenomena* 35 (3), 395–424. doi:10.1016/0167-2789(89)90077-8.

Wason, H., Herrmann, F. J., and Lin, T. T. Y. 2011. Sparsity-promoting recovery from simultaneous data: a compressive sensing approach. *81st Annual International Meeting, SEG, Expanded Abstracts*, 6–10. doi:10.1190/1.3628174.

Wason, H., Oghenekohwo, F., and Herrmann, F. J. 2014. Randomization and repeatability in time-lapse marine acquisition. *84th Annual International Meeting, SEG, Expanded Abstracts*, 46–51. doi:10.1190/segam2014-1677.1.

Xue, Z., Chen, Y., Fomel, S., and Sun, J. 2014. Imaging incomplete data and simultaneous-source data using least-squares reverse-time migration with shaping regularization. *84th Annual International Meeting, SEG, Expanded Abstracts*, 3991–3996. doi:10.1190/segam2014-1552.1.